Technical Report

Aquafin CRC

Numerical Hydrodynamic Modelling of the Tuna Farming Zone, Spencer Gulf

Mike Herzfeld, John F. Middleton, John R. Andrewartha, John Luick, Leeying Wu

March 2009

Aquafin CRC Project 4.6

(FRDC Project No.2005/059)

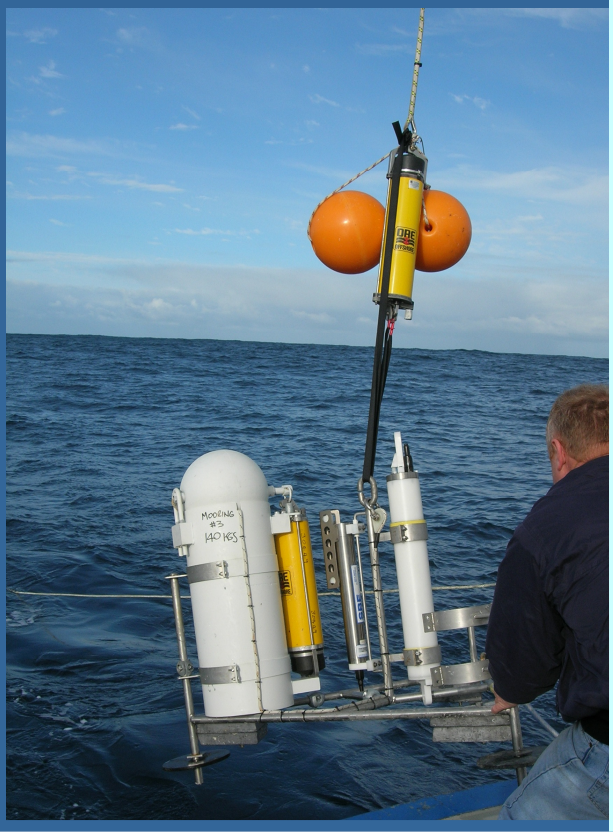

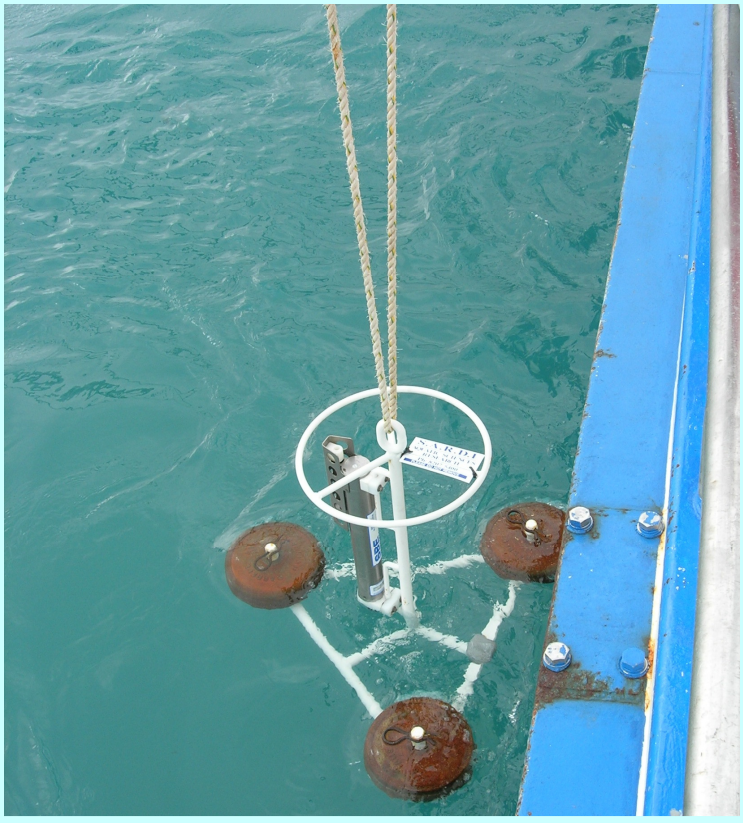

This publication may be cited as:
Herzfeld, M., Middleton, J.F., Andrewartha, J.R., Luick, J. and Wu, L. (2008) Numerical Hydrodynamic Modelling of the Tuna Farming Zone, Spencer Gulf. Technical report, Aquafin CRC Project 4.6, FRDC Project 2005/059. Aquafin CRC, Fisheries Research & Development Corporation and South Australian Research & Development Institute (Aquatic Sciences), Adelaide. SARDI Publication No F2008/000745-1, SARDI Research Report Series No 342, 100 pp.

Printed in Adelaide, March 2009
SARDI Aquatic Sciences
PO Box 120
Henley Beach SA 5022

SARDI Aquatic Sciences Publication Number F2008/000745-1
SARDI Research Report Series Number 342
ISBN Number 978-1-921563-11-9

Authors: Herzfeld, M., Middleton, J.F., Andrewartha, J.R., Luick, J. and Wu, L.
Reviewers: Paul van Ruth, Charles James
Approved by: Jason Tanner

Signed:
Date: 24 March 2009
Distribution: FRDC, ASBTIA, SARDI Aquatic Sciences Library
Circulation: Public domain

Numerical Hydrodynamic Modelling of the Tuna Farming Zone, Spencer Gulf

Mike Herzfeld[1], John F. Middleton[2], John R. Andrewartha[1], John Luick[2], Leeying Wu[2]

[1] CSIRO Marine and Atmospheric Research
Castray Esplanade
Hobart Tas 7000

[2] SARDI Aquatic Sciences
2 Hamra Ave
West Beach SA 5024

March 2009

Aquafin CRC Project 4.6

(FRDC Project No. 2005/059)

Table of Contents

List of tables

List of figures

Non-technical summary

A numerical hydrodynamic model was developed for the Spencer Gulf / Boston Bay region in order to investigate the circulation, flushing and connectivity of the region. The model also served as the driver for biogeochemical and sediment transport models, which were coupled to the hydrodynamic model. The model was forced with measured meteorological fields at the sea surface (wind, pressure, temperature) and sea surface elevation, temperature and salinity at the offshore boundary. The offshore boundary forcing was obtained using a nesting strategy involving a larger scale regional model.

The model output was compared to measured temperature and salinity data that was collected during a field program during 2005 / 2006. Sea level comparisons were also made with data measured at Port Lincoln, Wallaroo and Whyalla, and temperature, salinity and current comparisons were made with mooring derived data from the tuna farming zone (TFZ). Various model parameters and processes were optimized to achieve the best comparison between measured and modelled data. This optimization process provided insight into which parameters and processes the model was sensitive to. Simulations using the model were performed for the period August 2005 – August 2006, providing output of currents, sea level and temperature and salinity distributions.

The results from the data show there to be a strong (~20 cm s^{-1}) tidal currents that are very well reproduced by the model and that may be implicated in bottom stirring but not transport: particle displacements due to the tides were small and less than 1.4 km over a 3 hr period. Results for the weather-band currents (periods 3-20 days) are reasonably well produced by the model and show smaller currents (< 5 cm s^{-1}). However, due to the longer periods these can be important to the transport and flushing of the region: a 5 cm s^{-1} current with period 10 days will transport a fluid parcel 7 km over a 2.5 day period. Both data and model indicate the mean currents to be weak (~ 1 cm s^{-1}) and to the north/north east during both summer and winter: transport here over a 3-month period is around 80 km.

The gulf-scale model reproduces the clockwise circulation expected for winter. During summer, a similar pattern is found and opposite that expected from other studies. Nonetheless, the model does show predictive skill in the TFZ.

The currents were also found to be strongly sheared in the vertical and so may be important to shear enhanced diffusion and dispersal. However, estimates of the flushing times based on tracers and Lagrangian tracking show range from 10 days (Boston Bay) to 2 days (TFZ).

During summer, the model and data show a degree of connectivity between the coastal zone and the outer bay region that can be caused by local upwelling during summer, whereby offshore (eastward) winds force surface waters offshore, with onshore bottom flow. On the shelf, these winds would be downwelling favourable. In addition, the larger evaporation that occurs near the coast leads to dense water formation and bottom plumes that flow to the outer bay region. During winter, similar plumes result from coastal cooling rather than evaporation.

The strong seasonal cycle for temperature (salinity) is reproduced by the model to within1 ^{o}C (0.1 psu), and is shown to be largely driven by local heating (evaporation). Evidence does exist that local transport processes, including wind-driven upwelling and dense water formation, also effect temperature and salinity.

1. Background

Boston Bay is situated in the lower western side of Spencer Gulf (Figure 1.1) on the southern coast of Australia, and is the base for a large tuna aquaculture industry. This industry occupies the waters offshore of Boston Island, in an area hereafter called the tuna farming zone (TFZ). This area has been subject to detailed studies of the interactions between aquaculture and the environment. The present document is part of a larger study that seeks to develop an integrated hydrodynamic, sediment & biogeochemical model of the TFZ, to address environmental risks to the tuna industry, and to assess where nutrients released by the industry are dispersed to and what their potential environmental effects are. The larger study is detailed in Tanner and Volkman (2008).

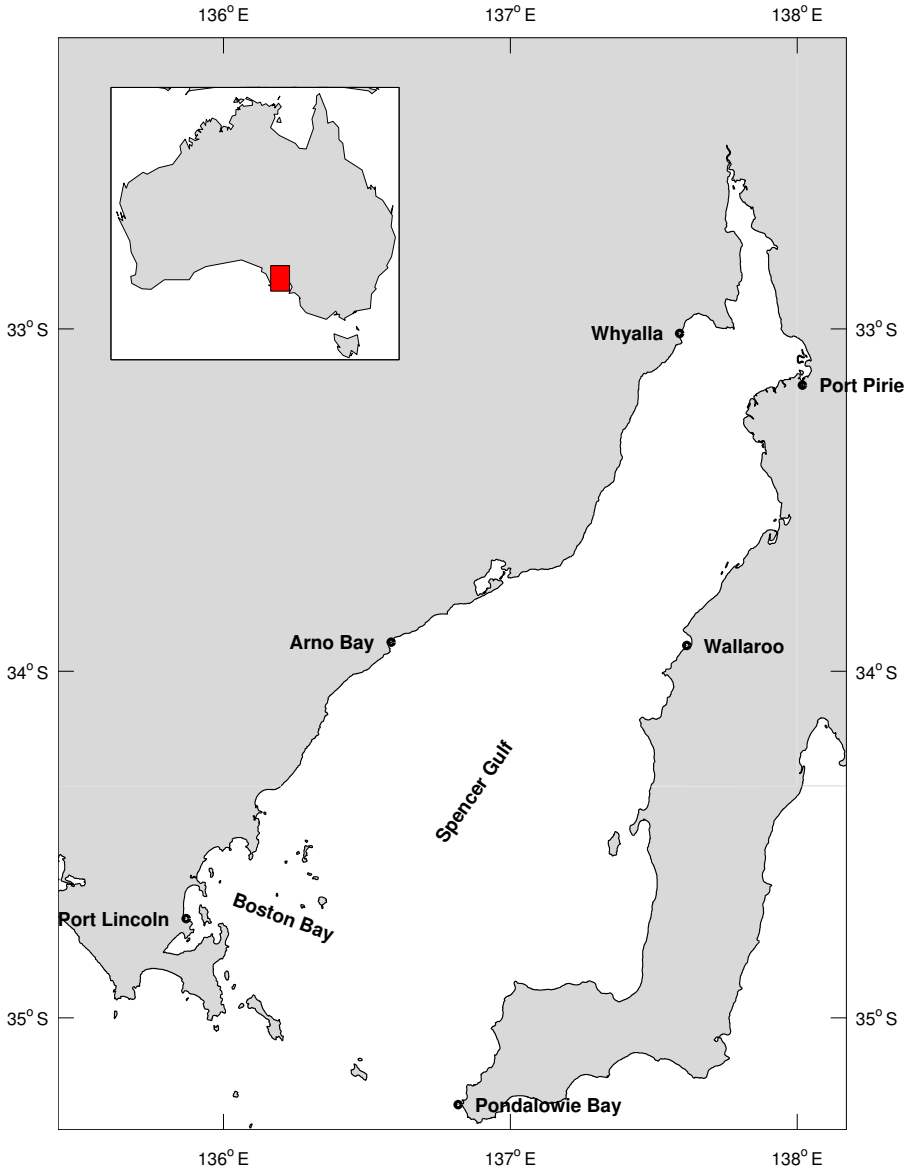

Figure 1.1. Spencer Gulf / Boston Bay region.

Studies of the tidal circulation of the gulf have been made (eg., Easton 1978; Nixon and Noye 1999) that show it to be a ¾ wave resonator, whereby the semi-diurnal constituents are amplified with current speeds of up to 50 cm s^{-1} mid-gulf. Additionally, because both the M2 and S2 tides have almost equal amplitude (but different frequency), these constituents interfere destructively leading to 4-5 day period every 14.8 days when the tidal velocities are small – the "dodge tide".

The gulf circulation driven by local meteorology and remote forcing is strongly seasonal. During winter, the westerly winds and atmospheric cooling combine to drive a westerly shelf circulation with water downwelled to depths of 300 m. Shelf current speeds of up to 1 m s^{-1} have been recorded on the shelf (Middleton and Bye 2007). Within the gulf, the atmospheric cooling is known to drive a clockwise circulation that appears to be modulated by the fortnightly dodge tide when the otherwise large (~50 cm s^{-1}) currents relax to near zero. Water is drawn in along the western side of the gulf and expelled past Kangaroo Island on the eastern side of the gulf.

During summer, evaporation is sufficient to make the gulf water denser than that found during winter, although significant gulf-shelf exchange is not observed. The reason for this appears related to the reversal of winds and resultant upwelling to the south-east of Kangaroo Island. Indeed, the analyses of Nunes Vaz et al (1990), Petrusivics (1993) and McClatchie et al (2006) suggest that the upwelled water forms a pool of sub-surface, nutrient rich water across the mouth of the gulf. This water is denser than that found in the gulf and may block its passage onto the shelf (Petrusivics 1993). Some penetration of upwelled water into the eastern side of the gulf is indicated from sea surface temperature data (see Middleton and Bye 2007). However, it may be possible that sub-surface intrusions do occur: little data has been collected to answer these questions.

The circulation driven by local winds and by the wind-driven circulation on the adjacent shelf has received little attention. Most recently, Middleton and Teixeira (2008) have shown that the gulf circulation driven by strong winds (10 m s^{-1}) is quite weak (< 5 cm s^{-1}) where the water depth is 10-20m or more. The reason for this is that the conditions of zero normal flow at coastal boundaries penetrate over a distance of the external deformation radius, that is, of order the width/length of the gulf. A similar result is found for the gulf circulation that is driven by (wind-driven) shelf circulation. As we will see from the study below, weak currents (< 5 cm s^{-1}) are found for the weather-band (3-20 days), both in the data and model. In shallow water (< 5m), the study of Middleton and Teixeira (2008) indicates that currents can be significantly larger (~15 cm s^{-1}) since the deformation radius is smaller.

During winter, the south-eastward winds expected to drive a clockwise circulation near the mouth of the gulf with water drawn in along the western side of the gulf and expelled along the Yorke Peninsula (Middleton and Teixeira 2008). This circulation should enhance that driven by dense water formation.

During summer, the winds and gulf circulation are expected to reverse, albeit with a weaker anticlockwise circulation near the gulf mouth (Middleton and Platov 2003; Middleton and Teixeira 2008). A schematic of the expected flow is shown in Figure 1.2. Consistent with this pattern, recent studies suggest that nutrient rich water should be drawn in along the eastern gulf mouth that arises from the summertime upwelling onto the shelf (Middleton and Teixeira 2008). As noted above, this water appears to prevent a strong gulf-shelf exchange that is found for winter (Lennon et al 1987).

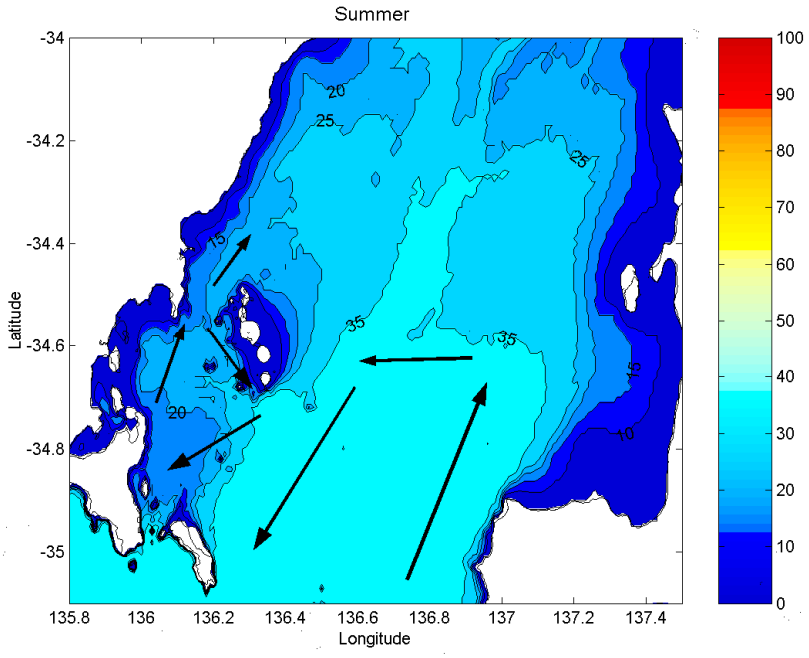

Figure1.2. The topography of the southern gulf region with the 0, 10, 15, 20, 25 35 m isobaths plotted. The arrows indicate expected flow due to mean summer winds. The arrow in the TFZ region corresponds to that estimated from the local model and data.

The numerical results will support the above conceptual model but with two additional complexities. The first is that when the waters are stratified, localized upwelling (downwelling) can occur for the Boston Bay region in the presence of eastward (westward) winds. Eastward winds drive surface gulf waters offshore that can drive a compensatory deeper onshore flow. On the adjacent shelf, eastward (westward) winds lead to downwelling (upwelling).

The second complexity arises from the topographic shielding of the TFZ from the larger gulf-scale summertime anticlockwise circulation. The local TFZ model and data below show that the flow past the region (along the 20 m depth contour) is to the north-north-east for all of the year. The larger gulf-scale regional model shows that the flow farther offshore (along the 30 m isobath) is to the south and south-west: this flow is essentially blocked by the Sir Joseph Banks group of islands that lie to the immediate north of the Boston Bay region.

While the wind-forced circulation (~ 5 cm s^{-1}) is smaller in magnitude than that of the 12 hourly tides (30-50 cm s^{-1}), we note here that the former persist for longer times (3 –20 days) and can be more important in terms of flushing of the region and in nutrient transport. Thus, both tidal and wind-driven motions are modelled in the study below, as are density currents that arise from atmospheric cooling and evaporation.

2. Objectives

In order to assess the physical characteristics of the TFZ, this study aims to implement a numerical hydrodynamic model that will provide predictive capacity for currents and mixing. The model is calibrated against data collected during field excursions. Insight into current regimes, flushing times, tracer dispersal distributions and residual flows can be gained from application of the model. The model is designed to aid in decisions regarding risks posed to the tuna industry, and assist in identifying mitigation strategies to those risks. The hydrodynamic model forms the basis for sediment transport and biogeochemical numerical investigations. The model was forced with atmospheric fluxes including wind stress, heat and freshwater exchanges, and with surface elevation, temperature and salinity on the offshore limits of the domain. A regional scale hydrodynamic model, which covers the whole of Spencer Gulf, is developed to establish boundary conditions for the local TFZ model. This model is represented with much larger resolution (~2-5 km) and covers a larger area, having the sole purpose of providing boundary conditions for the local model. The hydrodynamic model, its inputs, and model output, are discussed in more detail below. Analyses are presented addressing the flushing characteristics of the TFZ, passive tracer distributions in response to the circulation, residual flow dynamics and connectivity.

3. The Hydrodynamic Model

The hydrodynamic model used to simulate the flow and mixing of the TFZ is SHOC (Sparse Hydrodynamic Ocean Code; Herzfeld, 2006). This model has been developed by the Environmental Modelling group at CSIRO (Commonwealth Scientific and Industrial Research Organization) Division of Marine and Atmospheric Research over the last decade. SHOC is intended to be a general purpose model applicable to scales ranging from estuaries to regional ocean domains, and has been successfully applied to a variety of applications encompassing these scales to date. SHOC is a three-dimensional finite difference hydrodynamic model based on the primitive equations. Outputs from the model include three-dimensional distributions of velocity, temperature, salinity, density, passive tracers, mixing coefficients and sea level. The equations forming the basis of the model are similar to those described by Blumberg and Herring (1987). SHOC is based on the MECO model (Model for Estuaries and Coastal Oceans; Walker and Waring, 1998) with added functionality to allow distributed processing over multiple computing processors. SHOC also employs a sparse coordinate system internally that allows the representation of unused land in the model to be excluded. Inputs required by the model include forcing due to wind, atmospheric pressure gradients, surface heat and water fluxes, and open boundary conditions (e.g. tides). A schematic of the major forcing mechanisms captured by SHOC is included as Figure 3.1. SHOC is based on the three-dimensional equations of momentum, continuity and conservation of heat and salt, employing the hydrostatic and Boussinesq assumptions. The equations of motion are discretized on a finite-difference stencil corresponding to the Arakawa C grid.

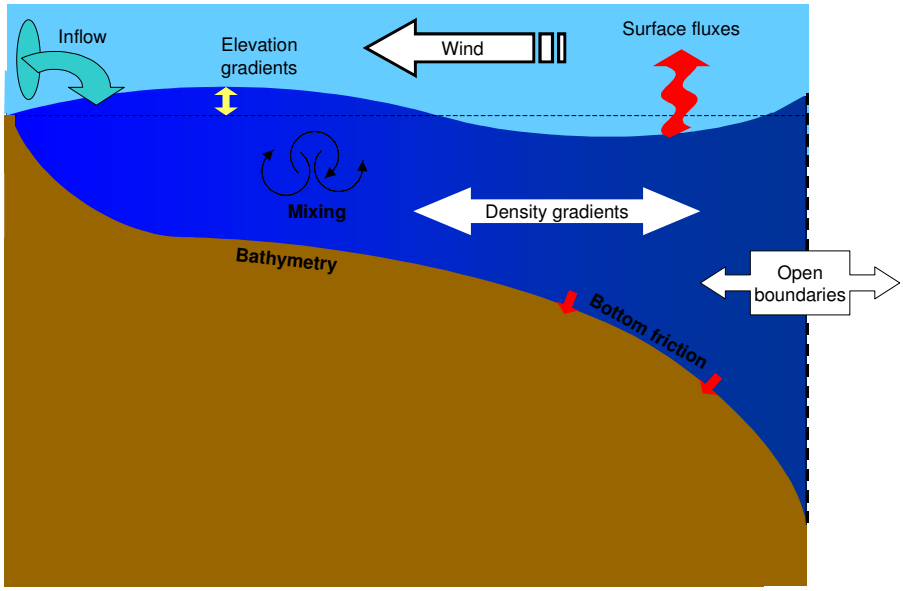

Figure 3.1. Schematic of forcing mechanisms in SHOC.

The model uses a curvilinear orthogonal grid in the horizontal and a choice of fixed 'z' coordinates or terrain following σ coordinates in the vertical. The curvilinear horizontal grid was particularly useful in this application since it enabled high resolution to be specified in areas of the study region where small-scale motions were present and larger resolution where

they were not. The ‘z’ vertical system allows for wetting and drying of surface cells, useful for modelling regions such as tidal flats where large areas are periodically dry. SHOC has a free surface and uses mode splitting (Simons, 1974) to separate the two-dimensional (2D) mode from the three-dimensional (3D) mode. This allows fast moving gravity waves to be solved independently from the slower moving internal waves, allowing the 2D and 3D modes to operate on different time-steps, resulting in a considerable improvement in computational efficiency. The model uses explicit time-stepping throughout except for the vertical diffusion scheme which is implicit. The implicit scheme guarantees unconditional stability in regions of high vertical resolution. A Laplacian diffusion scheme is employed in the horizontal on geopotential surfaces. Smagorinsky mixing coefficients may be utilized in the horizontal (Griffies and Hallberg, 2000).

SHOC can invoke several turbulence closure schemes, including k-ε, Mellor-Yamada 2.0 and Csanady type parameterisations. A variety of advection schemes may be used on tracers and 1st or 2nd order can be used for momentum. This study used the QUICKEST advection scheme for tracers (Leonard, 1979) in conjunction with the ULTIMATE limiter (Leonard, 1991). This scheme is characterized by very low numerical diffusion and dispersion, and yielded excellent performance when resolving frontal features, which often occurred during tracer analyses. SHOC also contains a suite of radiation, extrapolation, sponge and direct data forcing open boundary conditions. Input and output is handled through netCDF data formatted files, with the option of submitting ascii text files for simple time-series forcing. The netCDF format allows input of spatially and temporally varying forcing and initialization data in a grid and time-step independent manner. SHOC is capable of performing particle tracking and may be directly coupled to ecological and sediment transport models.

4. Model Domain

The simulation of the physics of the Boston Bay region required the construction of two model grids. The regional grid supplied the initial and open boundary conditions for a smaller local grid of the local study region, nested within the regional grid. In the absence of field-derived temperature, salinity and surface elevation measurements to apply to the open boundaries, this strategy is the only way of adequately driving the model through the open boundaries of the local model. The regional domain is illustrated in Figure 4.1 and the TFZ (local) domain in Figure 4.2.

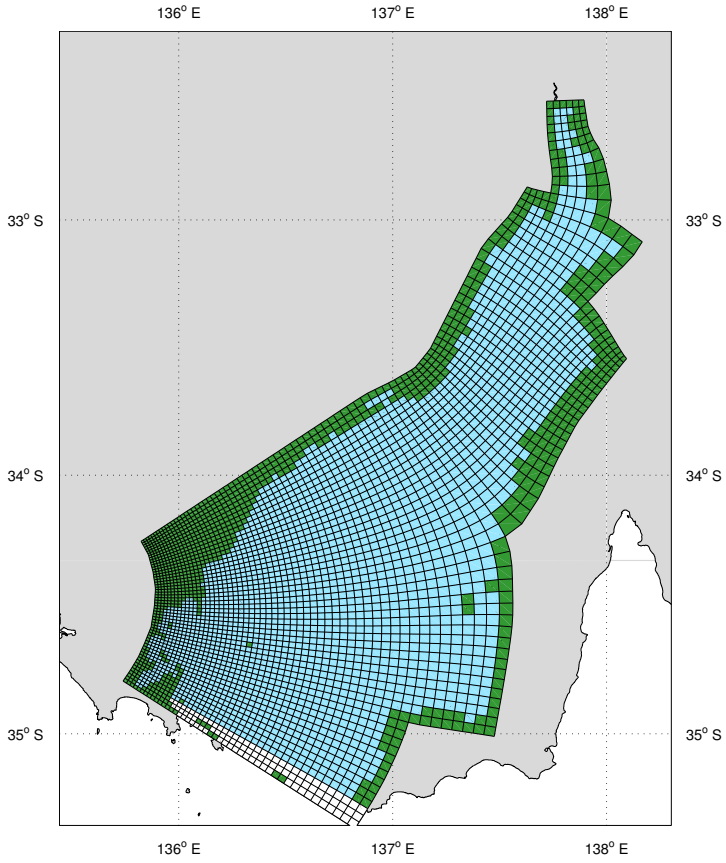

Figure 4.1. Regional Spencer Gulf domain.

The regional grid is curvilinear with variable resolution over the domain. Seaward of Boston Island the resolution is ~1500 m with resolution increasing to > 6 km on the eastern side of the gulf. The model uses 23 layers in the vertical with 0.5 m resolution at the surface and ~8 m resolution near the maximum depth of 60 m. The grid size is 55 x 95 x 23; 45% of surface cells are wet cells and 30% of all cells in the grid are wet. Run time ratios achieved were ~192:1 (i.e. the model simulates 192 days of results in 1 day of real time), allowing an annual simulation to be completed in ~2 days. The run-time ratio is determined by the stability constraints on the model, which limit the maximum time-step to be used for 2D and 3D modes, and are dependent on the grid resolution, the water depth, stratification and the size of the grid.

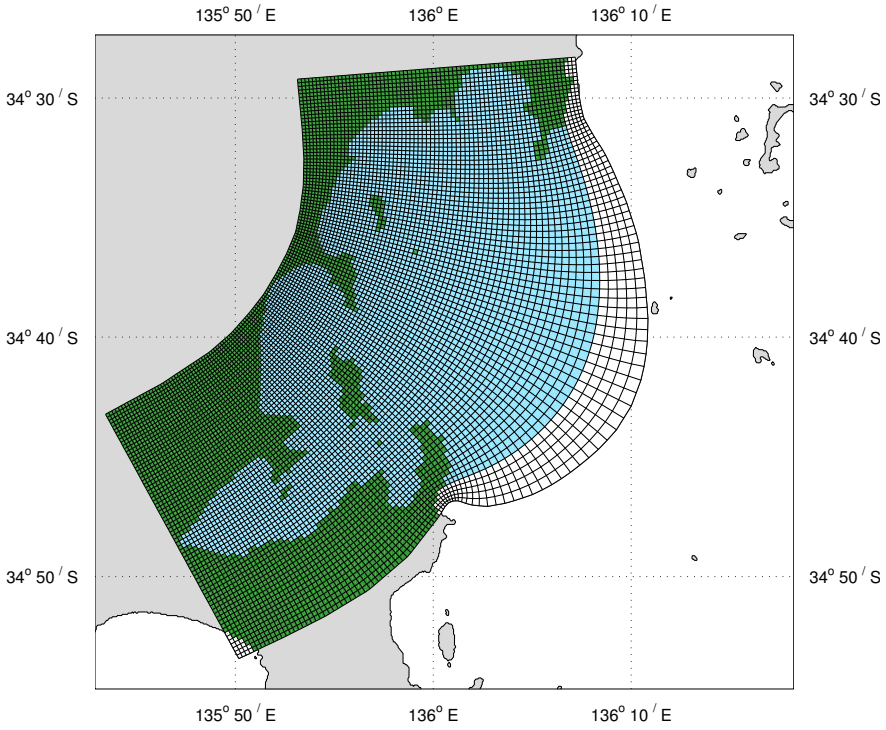

Figure 4.2. The tuna farming zone (TFZ) domain.

A curvilinear grid was also used to model the TFZ region. The grid spacing seaward from Boston Island is ~330 m and a maximum resolution of ~1 km exists on the offshore open boundary. The grid dimensions are 135 x 70 x18, with 0.5 m resolution in the vertical at the surface and ~4 m resolution at the bottom with a maximum depth of 30 m. This domain also consists of a high percentage of land cells, with 53% of the surface layer comprising wet cells and only 28% of the 3D domain being wet. Run time ratios achieved were ~90:1, allowing an annual simulation to be completed in ~4 days.

The seaward limit of the open boundary for the local model was based on the distribution of the tuna farming lease sites in 2005. It is acknowledged that these sites are subject to change, and there is a tendency for leases to be granted further into Spencer Gulf. Obviously the modelling cannot anticipate future lease configurations, hence it was considered appropriate to define the offshore limit of the local model based on the lease configuration of mid-2005 (Figure 4.3). As information became available, it was evident that leases were in fact edging into deeper water, and some of the proposed leases for 2006 were impinging on the local grid open boundary (Figure 4.4). The model domain was defined on the basis of information available at the commencement of the project, which encompassed all lease sites positioned during 2005.

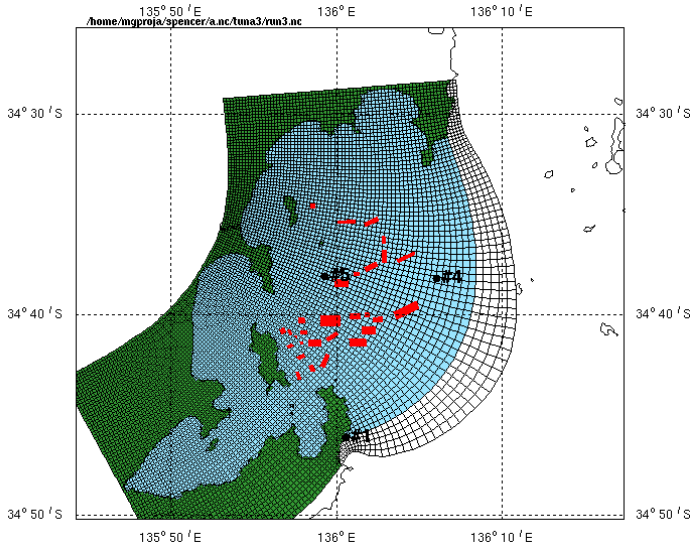

Figure 4.3. Lease sites at commencement of the study; 2005.

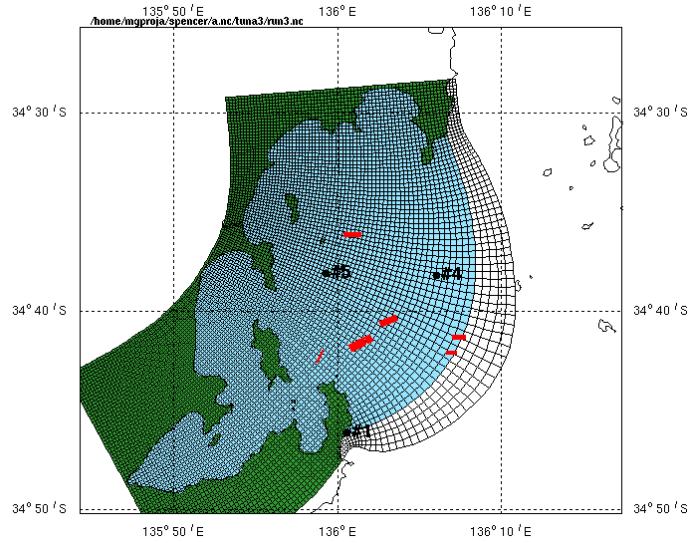

Figure 4.4. Differences in proposed 2006 lease sites.

5. Input Data

The model was forced with surface atmospheric fluxes (wind, heat and freshwater), and elevation, temperature and salinity on the open boundaries. A field program was implemented to supply data to force the open boundary of the regional model, and to supply calibration data for both models. The simulation period, defined by availability of data from this field program, was chosen as 2 Sep 2005 to 11 Aug 2006 inclusive, providing ~12 months of simulation. The sources of the forcing data are detailed below.

5.1. Bathymetry

The bathymetry for the regional model was interpolated from Geoscience Australia's 1 km bathymetric product (Petkovic and Buchanan, 2002). The bathymetry for the TFZ region was initially interpolated from Geoscience Australia's 2005 product at 250 m resolution, but as this inadequately represented the bathymetry of the region, it was supplemented with digitized bathymetry from the AUS134 navigational chart. The final bathymetry used for the TFZ is displayed in Figure 5.1.1. Overlaid on this figure are the 2005 lease site locations, and the locations of the moorings deployed in the TFZ (see Section 6).

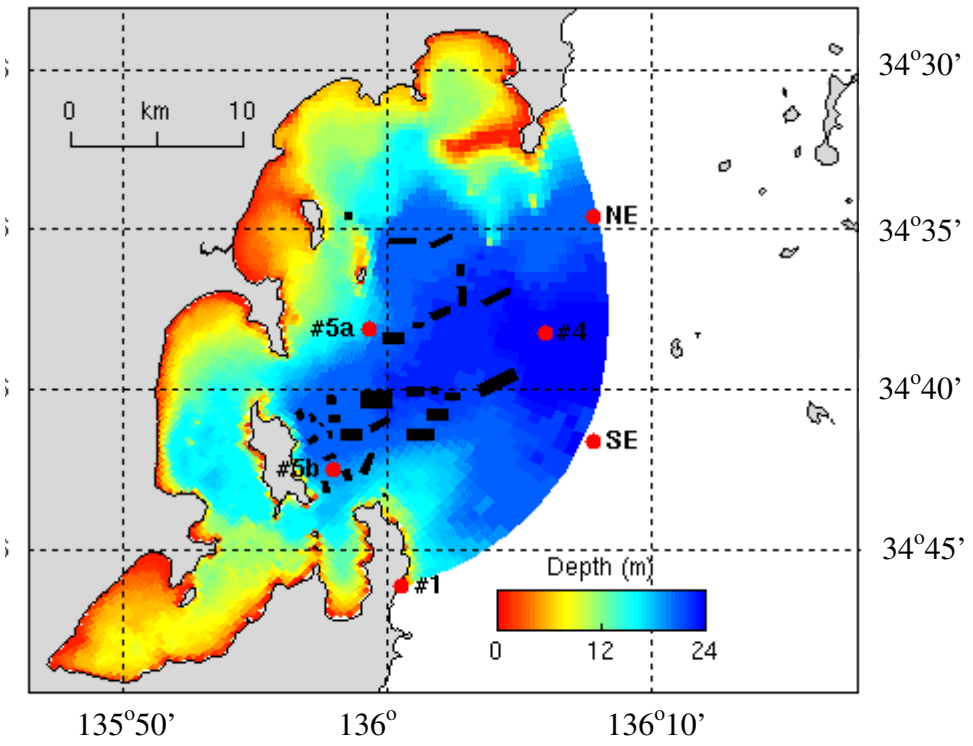

Figure 5.1.1. Bathymetry of the tuna farming zone region. NE and SE refer to the limits of the tuna farming zone designated during 2005. Numbers indicate mooring locations (see Section 6.1).

5.2. Wind Forcing

Wind speed and direction data were obtained from the Bureau of Meteorology at the locations depicted in Figure 5.2.1 and interpolated onto the regional domain to provide a temporally and spatially varying wind-field.

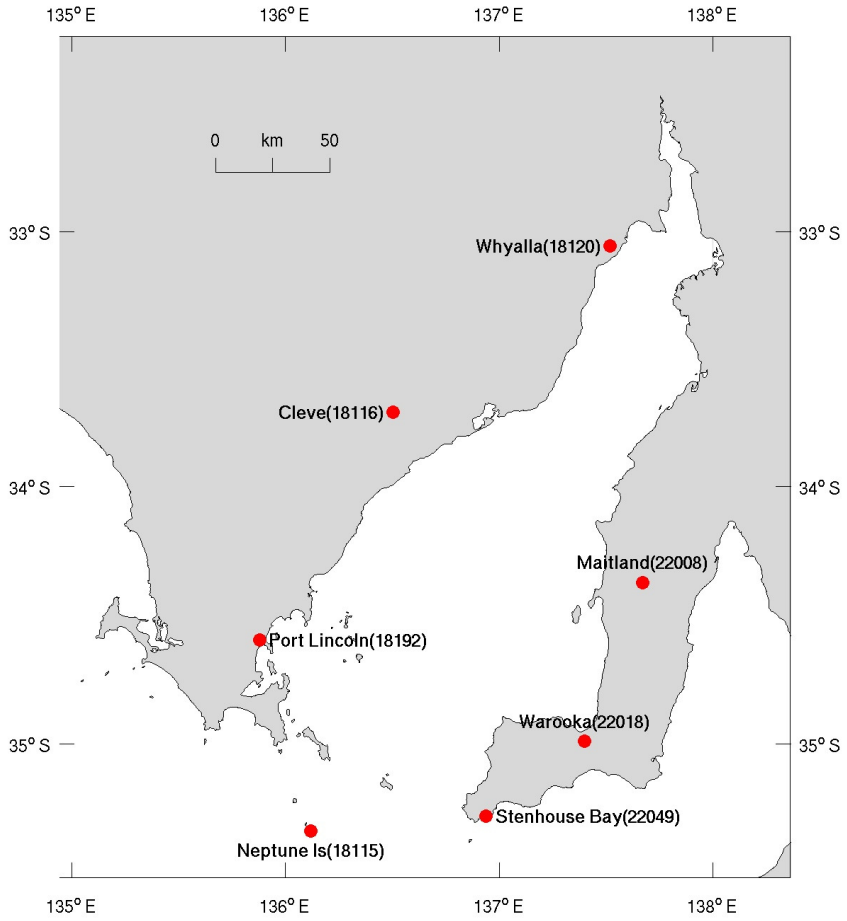

Figure 5.2.1. Wind Measurement sites. Numbers in brackets indicate the number of measurements taken during the simulation period.

A sample of the wind-field at selected sites is shown in Figure 5.2 for the simulation period. The mean wind speed and direction during the whole period is shown in Table 5.1.

Table 5.1. Mean wind speed and direction for wind measurement sites

Site	Annual Mean Wind Speed ($m\ s^{-1}$)	Annual Mean Wind Direction (^oT)
Cleve	5.3	192
Port Lincoln	5.1	208
Neptune Island	8.2	178
Stenhouse Bay	6.1	192
Warooka	3.2	202
Maitland	2.9	192
Whyalla	4.8	211

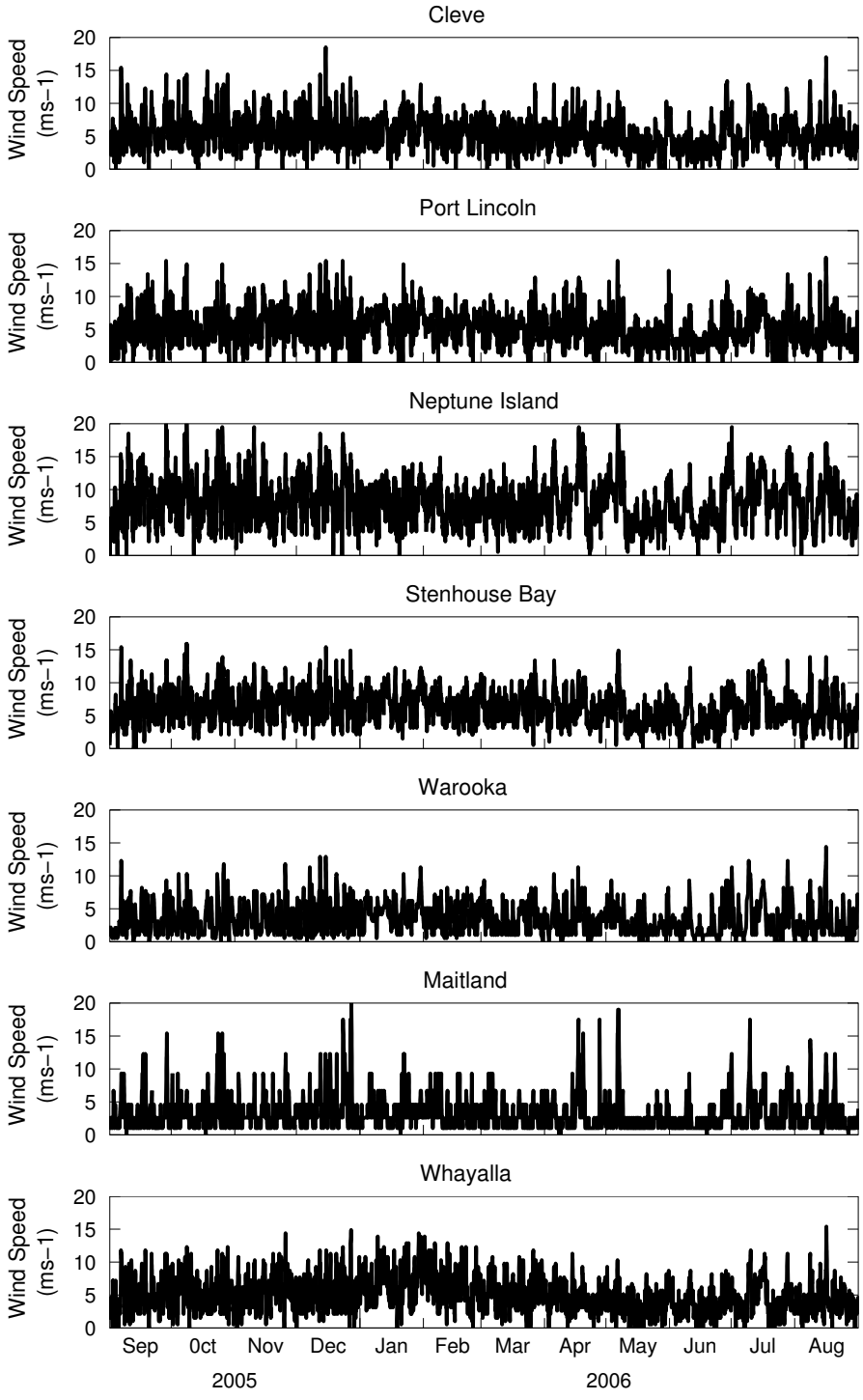

Figure 5.2.1. Wind speed at measurement sites.

Figure 5.2.1 and Table 5.1 indicate that for the simulation period, the mean wind in the TFZ region was a relatively light (~5 m s^{-1}) southerly. Wind speed is generally below 15 m s^{-1}, with the southern most sites and those on the western side of the gulf experiencing higher wind-speed.

5.3. Surface Elevation

The time series of surface elevation prescribed on the open boundaries of the local TFZ model were supplied from output of the regional model. The elevations used in the regional model consist of a high frequency component (tidal component with periods < 1 day) and a low frequency component with periods of days to weeks. Measurement sites for which sea level data were obtained are illustrated in Figure 5.3.1.

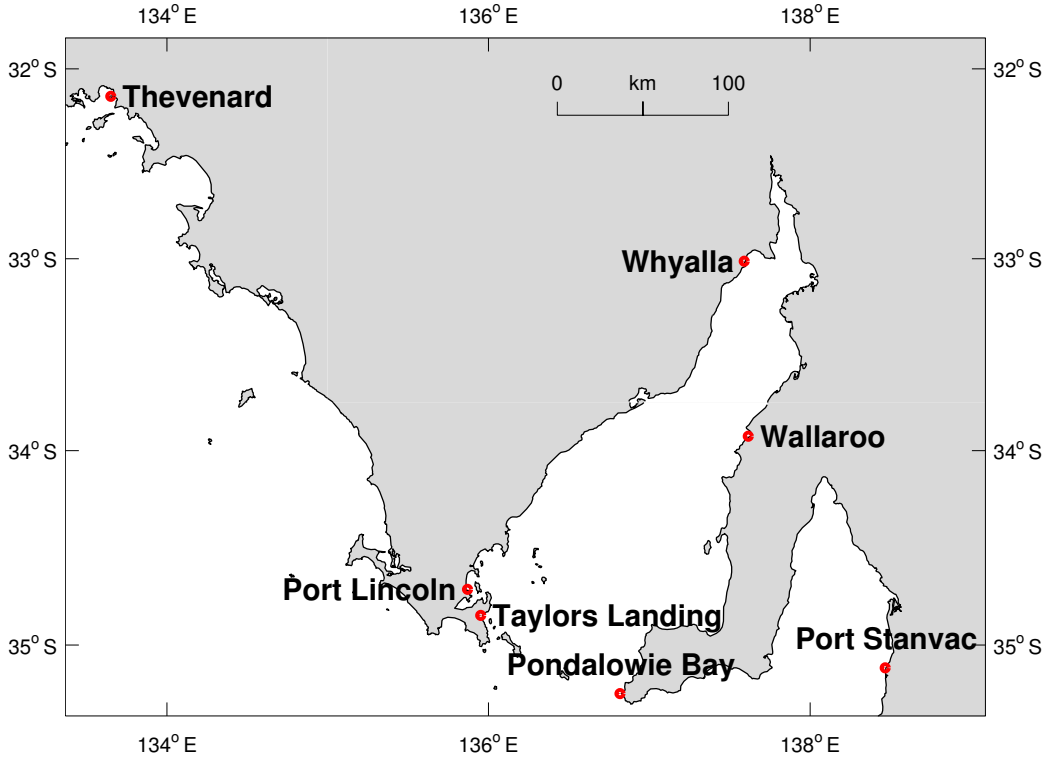

Figure 5.3.1. Tidal measurement locations.

There are two components of forcing needed at the mouth of the gulf for the (large scale) regional model. We first discuss forcing in the tidal band and then forcing in the weather band (typically 3 days or longer).

Tidal-band Forcing

The open boundary of the regional model fortuitously corresponded to a linear transect between Taylor's Landing and Pondalowie Bay, and to a lesser extent Thevenard and Port Stanvac. This allowed the tidal harmonics and low frequency signal corresponding to these measurement sites to be linearly interpolated along the open boundary of the regional model. The tidal harmonics for Taylor's Landing and Pondalowie Bay (obtained from http://www.flaterco.com/xtide/) allowed the phase and amplitude of the 14 largest constituents (see Table 5.3.1) to be linearly interpolated along the open boundary of the regional model. The tide was then reconstructed from this information at the open boundary nodes to create the tidal sea level response along the regional domain seaward boundary.

Table 5.3.1. Tidal harmonics for Taylor's Landing

Constituent	Amplitude (m)	Phase (Deg)
M2	0.2013	17.75
S2	0.2109	67.80
K1	0.2105	24.49
O1	0.1528	358.26
S1	0.0075	139.10
Q1	0.0329	336.19
P1	0.0679	18.01
N2	0.0159	97.48
NU2	0.0	0.0
K2	0.0615	69.18
L2	0.0146	57.62
2N2	0.0100	83.31
MU2	0.0120	98.60
T2	0.0167	73.41

It is observed from Table 5.3.1 that the dominant constituents in the region are those due to M2, S2 and K1, all of which have approximately the same amplitude. It is the similarity between the amplitude of the semi-diurnal components that allows the unique phenomena of the dodge tide to occur in Spencer Gulf; this occurs when M2 and S2 are exactly out of phase, therefore cancelling and resulting in no tidal movement (and hence no currents) for the tidal period.

Weather-band Forcing

Sea level signals across the gulf mouth need to be prescribed that correspond to forcing by local winds and the wind-forced shelf circulation. Unfortunately, the sea level records from M1 and M2 were found to have datum shifts of 10 – 20 cm brought about by re-deployment of the instruments at slightly different depths after servicing (Table 6.1 below). Such datum shifts must be eliminated if the data is to be used to drive the model open boundary for periods longer than the minimum period of co-incident data (42 days). In addition, due to lack of equipment, the pressure sensors adopted for moorings M1 and M2 only give approximate depths with an accuracy of a centimetre or so. Moreover, no averaging was made to eliminate aliasing due to waves: sea level heights were recorded instantaneously every 15 minutes. Mooring M3 did use a high quality tide gauge sensor and every 15 minutes samples were obtained as burst (4 minute) averages. Thus, the quality of the M1 and M2 sea level data remains to be determined.

To this end a re-analysis is made (Appendix A) of the low-passed filtered sea level data from the gulf sites M1 to M5. First, the low-pass filtered data at site M5 is found to be very similar to that at site M1 so that data from the former (M5) can be used to produce a long 10 month time series of continuous data at site M1.This also gives confidence in the M1 data collected. Similar continuous data sets are obtained for site M2 and M3. The mean seasonal sea level signal at M3 (~ 10 cm) is assumed for sites M1 and M2 and the underlying assumption is that no net geostrophic flow into the gulf occurs for periods of two months or greater.

The use of these (uncertain) time series is discussed in section 7.3. As an alternative, continuous time series of sea level were also obtained for Thevenard and Port Stanvac from the National Tidal Centre (NTC) and used to extract the low frequency signal. This signal propagates anti-clockwise around the Australian coast, and a lag of 7.68 hours was computed between Thevenard and Port Stanvac. The lag between any open boundary node and

Thevenard could then be computed as a fraction of this lag. The amplitude of the low frequency signal at each open boundary node was calculated using a weighted interpolation in time and space between the Thevenard and Port Stanvac data, and applied at the correctly lagged time relative to Thevenard. The sea level was then linearly interpolated across the gulf mouth. The seaward boundary in the model was forced with the tidal and weather-band sea levels using relaxation to a gravity wave radiation condition with a time-scale of 30 minutes following the methodology of Blumberg and Kantha (1985).

5.4. Temperature and Salinity

The initial conditions for temperature and salinity for both regional and local grids were derived from the product synTS (Ridgway et al., 2006). This product uses satellite altimetry to prescribe surface temperature and sea level distributions, then utilizes correlations based on climatology to project the surface distributions through depth. Resolution is 0.25 degrees. The initial temperature and salinity distributions over the regional domain are illustrated in Figure 5.4.1.

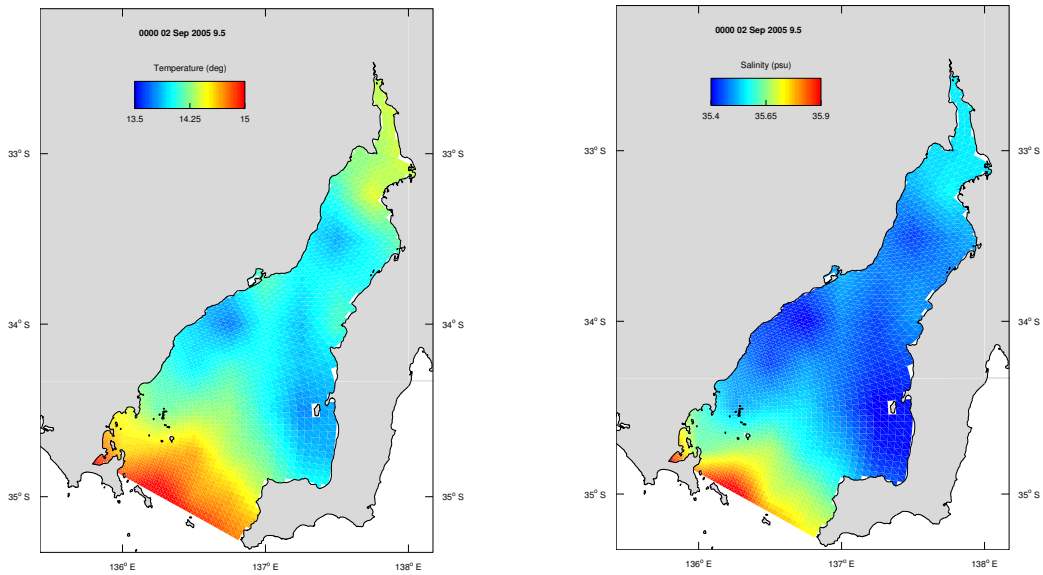

(a) Temperature (b) Salinity

Figure 5.4.1. Initial conditions for the regional grid derived from synTS.

The open boundary forcing for the regional model was derived from measurements obtained from the moored instruments across the mouth of Spencer Gulf (see Section 6). These instruments provided temperature and salinity at the surface on the eastern and western sides of the gulf, and at the deepest location mid-gulf. These surface and bottom data were used as endpoints of a profile of temperature and salinity (T/S); the depth distribution of T/S between these endpoints was scaled to a time dependent density profile obtained from the model during its simulation at a location 10 grid cells into the interior of the domain from the open boundary.

5.5. Heat and Salt Fluxes

Heat fluxes were computed from standard meteorological measurements by the methods outlined in Herzfeld (2005, Chapter 9). Short wave radiation was estimated from the sun's hour angle at the latitude corresponding to Spencer Gulf, and corrected for (measured) cloud cover. Long wave radiation was calculated using the model sea surface temperature and

measured air temperature, also correcting for cloud. Sensible and latent heat fluxes were calculated using the bulk method of Kitaigorodskii et al. (1973), which required wet and dry bulb air temperature, pressure and wind-speed measurements as input. The heat flux components for the simulation period were computed from atmospheric data collected at Warooka, and are illustrated in Figure 5.5.1.

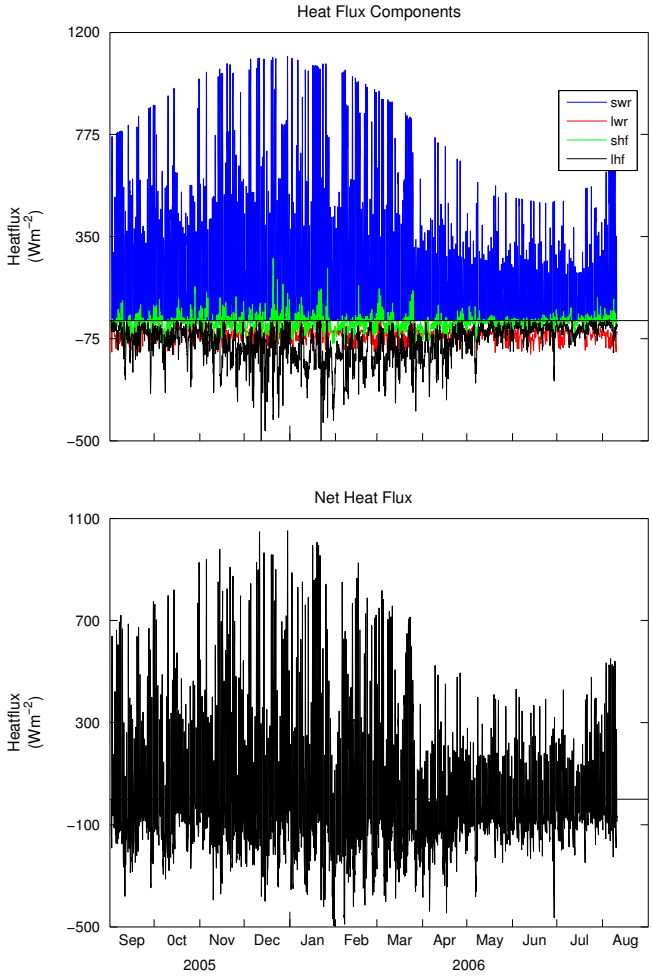

Figure 5.5.1. Heat fluxes calculated for Spencer Gulf based on atmospheric data obtained from Warooka. Swr – short wave radiation, lwr – long wave radiation, shf – sensible heat flux, lhf – latent heat flux.

The salt flux is defined as the difference between evaporation and precipitation. Rainfall was spatially and temporally interpolated from the meteorological sites illustrated in Figure 5.2.1. Evaporation over water is difficult to measure, and was estimated from monthly means provided by the bureau of meteorology (http://www.bom.gov.au/cgi-bin/climate/cgi_bin_scripts/evaporation.cgi) at locations corresponding to Port Augusta and Yorketown at the end of Yorke Peninsula. Differences in air – sea temperature can initiate a stable layer above the sea surface which suppresses evaporation, resulting in differing evaporation rates over the ocean compared to those over land. This typically requires the application of a pan factor to land based evaporation measurements to provide rates applicable over the ocean. These pan factors are the ratio of the evaporation rate over the ocean to that encountered over a standard meteorological evaporation pan under similar atmospheric conditions. Pan factors are usually < 1.0, and were treated as calibratable parameters in this study, varying linearly from the southern boundary

to the head of the gulf. Evaporation rates used in regional and local grids in the TFZ and the head of the gulf are displayed in Figure 5.5.2.

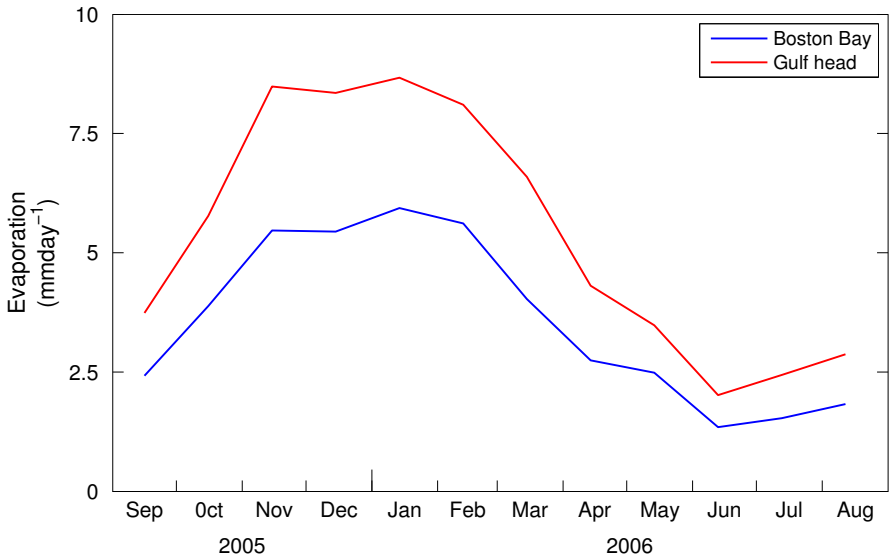

Figure 5.5.2. Estimated evaporation rates in Spencer Gulf.

6. Measured Data

6.1. Fixed Moorings – an overview

Between August 30 2005 and September 1 2006, a series of oceanographic moorings were placed across the mouth of Spencer Gulf and in and around the tuna-farming zone (Figures 6.1.1 and 6.1.2). Shallow moorings (3-5 m) were placed on either side of the mouth at Pondalowie Bay (mooring 2) and Carcasse Rock (mooring 1. e.g. Figure 6.1.3) to measure conductivity, temperature and depth, while a similar deep-water mooring (50 m), also incorporating a tide gauge, was placed in the middle of the mouth of the gulf, north of Wedge Island (mooring 3). The two moorings in the farming zone measured conductivity, temperature, depth, light and chlorophyll levels, and were also configured with ADCPs to measure current speeds throughout the water column (e.g. Figure 6.1.4, mooring 4). All shallow water moorings were successfully serviced on a three monthly basis, when data was downloaded, moorings cleaned and then redeployed. Fouling was an issue on many of the moorings (Figure 6.1.5), and may have compromised data quality on occasion. Mooring 5 was relocated to new positions in the TFZ on these servicing events. Due to its location, mooring 3 required a reasonable sized vessel to perform the deployment, hence was only serviced once (in February). During the May 2006 service, mooring 5 was re-located south of its previous position (from 5c to 5d), mooring 4 was re-located to lie further north-east on the model open boundary (from 4c to 4d) and an extra mooring was deployed (mooring 6) having the same configuration as mooring 4 minus an ADCP. These moorings collected data that is essential for developing the proposed hydrodynamic models, as well as data for calibrating the biogeochemical model. The locations and turn-around details are displayed in Table 6.1.

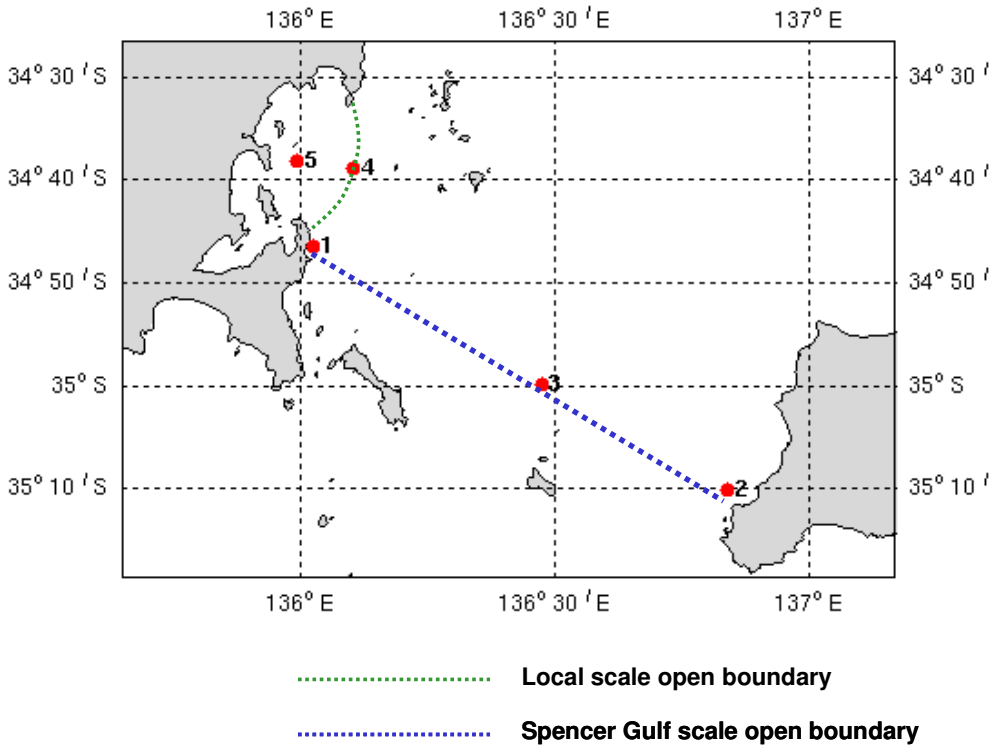

Figure 6.1.1. Location of moorings deployed in Spencer Gulf. The local scale open boundary indicates the extent of the detailed model, which is influenced by what happens in the less detailed model of Spencer Gulf.

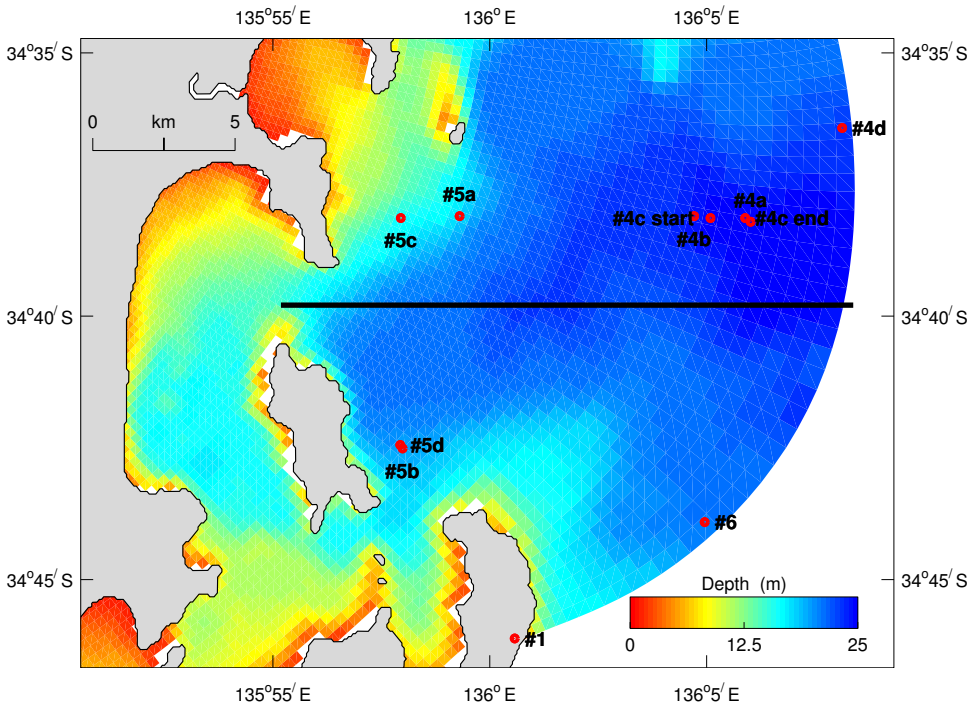

Figure 6.1.2. Details of moorings deployed in the TFZ. Mooring 4 was dragged during deployment #3; start and end locations are denoted 4c_start and 4c_end respectively. The thick black line corresponds to a CTD transect that was sampled monthly (see below).

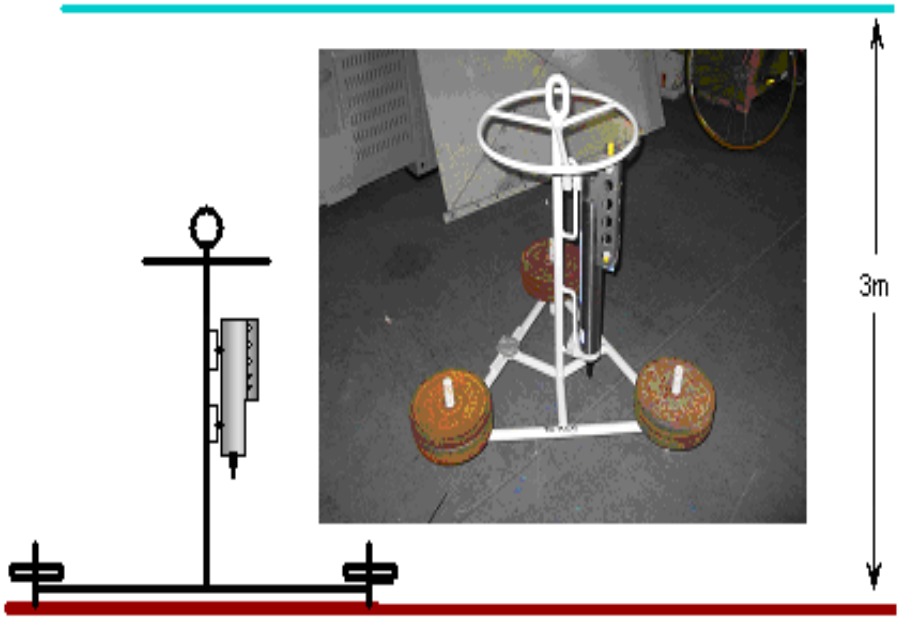

Figure 6.1.3. Mooring 1 & 2 configuration.

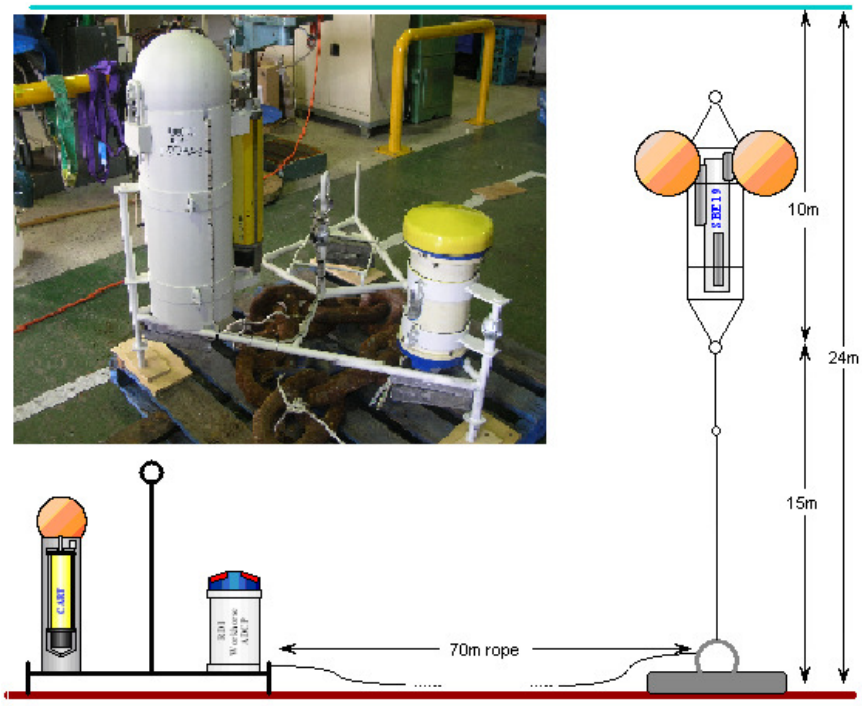

Figure 6.1.4. Mooring 4 configuration.

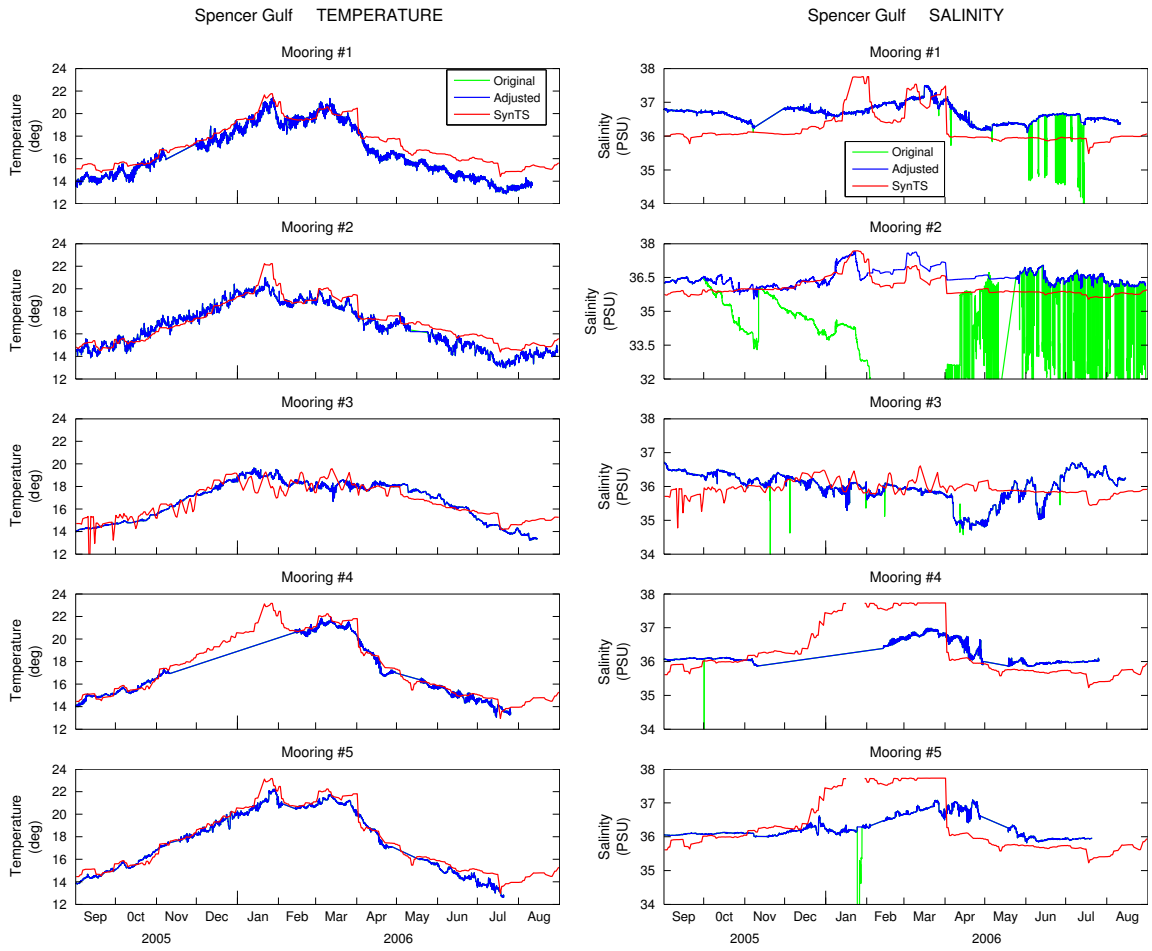

Figure 6.1.5. Raw and processed temperature and salinity time series.

Table 6.1. Mooring location and deployment details.

Mooring 1

Deployment	Date (local)	Sensor Depth (m)	Latitude	Longitude
Seabird Microcat with depth sensor				
1	31/0805 08:55	4.4	34 46.118S	136 00.576E
2	30/11/05 8:50	4.8	34 46.118S	136 00.576E
3	16/03/06	4.3	34 46.118S	136 00.576E
4	18/5/2006 17:40	4.8	34 46.108S	136 00.600E

Mooring 2

Deployment	Date (local)	Sensor Depth (m)	Latitude	Longitude
Seabird Microcat with depth sensor				
1	1/9/05 12:41	~5	35 13.873S	136 50.371E
2	11/11/05 10:10	~5	35 13.873S	136 50.371E
3	01/02/06	5.38	35 13.873S	136 50.371E
4	24/05/06 13:10	5.40	35 13.873S	136 50.371E

Mooring 3

Deployment	Date (local)	Sensor Depth (m)	Latitude	Longitude
Seabird Microcat with depth sensor + Seabird SBE 26 Integrating tide gauge				
1	1/9/05 09:15	48.33	35 00.089S	136 27.968E
2				
3	14-Feb-06 17:15	48.47	35 00.086S	36 27 .989E
4				

Mooring 4

Deployment	Date (local)	Sensor/Water Depth (m)	Latitude	Longitude
Seabird * SBE19 + RDI Workhorse 600Khz (High resolution model)				
1	31/08/05 11:23	13.80/24	34 38.206S	136 06.011E
2	17/11/05 11:40	?/22	34 38.101 S	136 04.711 E
3	13/Feb/06 10:20	9.66/22	34 38.137 S	136 05.090 E
4	18/5/2006 13:20	9.04/22	34 36.425S	136 08.126E

Mooring 5

Deployment	Date (local)	Water Depth (m)	Latitude	Longitude
Seabird * SBE19 + Nortek Aquapro 1Mhz Adcp (with external battery pack)				
1	31/0805 10:20	18.53/20	34 38.099S	135 59.306E
2	17/11/05 10:25	19.89/18	34 42.508 S	135 57.993 E
3	13/Feb/06 11:31	20.05/18	34 42.465 S	135 57.946 E
4	18/5/2006 11:30	20.13/18	34 42.446S	135 57.938E

Mooring 6

Deployment	Date (local)	Water Depth (m)	Latitude	Longitude
Seabird * SBE19				
1	18/5/2006 15:05	~20	34 43.908S	136 04.953E

6.2. Temperature/Salinity Mooring Data

Overall, the quality of data retrieved from the moorings is fair. Temperature and salinity are displayed in Figure 6.1.5. Mooring #4 lost all data for the second deployment; temperature appears reasonable for all other deployments. Salinity suffers from several obvious problems. Mooring 1 is ~0.7 psu saltier than mooring 4 and 5, although the lateral distance between all three moorings is not great. It is considered unlikely that such a large salinity gradient could exist in the absence of reasonable freshwater or salt input fluxes. Mooring 2 becomes fresher throughout the course of the first and second deployments. After the first turnaround salinity jumps markedly, indicative of a systematic drift of the salinity sensor. The third deployment produced no reasonable salinity data for mooring 2, and data from synTS was substituted for this period with a 0.6 psu offset applied. The fourth deployment contained an excessive number of spikes. Mooring 3 looks reasonable except for the odd low salinity spike. As mentioned above, mooring 4 lost all data for the second deployment, otherwise data looks reasonable. Mooring 5 has an anomalous spike in the data toward the end of January, otherwise also looks reasonable.

These errors in the salinity measurements can be managed to a certain extent by interpolating over gaps and de-trending salinity drifts. The adjusted salinity to be used as model input is also displayed in Figure 6.1.5. The synTS T/S is included in Figure 6.1.5 for reference. Note that synTS is the most accurate derived product suitable for analysis of temperature or salinity available.

6.3. Transect and SST Data

To put the above time series in context, we next discuss the SST and transect data obtained for the region. The transect data was obtained monthly (from September 2005 to August 2006) and along a zonal path, just south of M4 and M5- see Figure 6.1.2. Only valid data that largely covered the section is discussed. We begin with the SST image (MODIS) shown in Figure 6.3.1 for November 2nd 2005.

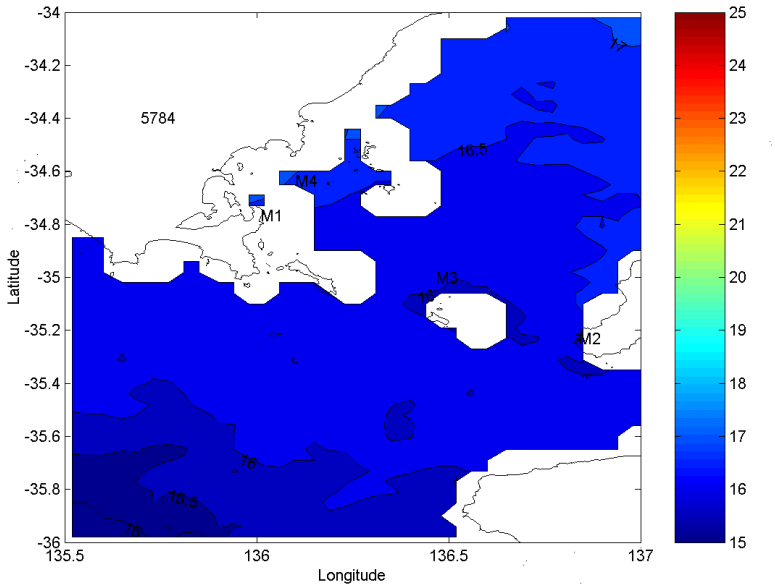

Figure 6.3.1. MODIS SST for November 2nd 2005 (JD 5785). Contour interval is 0.5 ˚C.

As is evident, there is little spatial variation and the cool 16 °C water is indicative of winter conditions. Indeed, the wind stress to this time (JD 5785), and up until the end of 2005 (JD 5842), is characterized by a mean direction to the east and by the passage of strong storms (0.1-0.2 Pa) every 3-20 days (Figure 6.3.2).

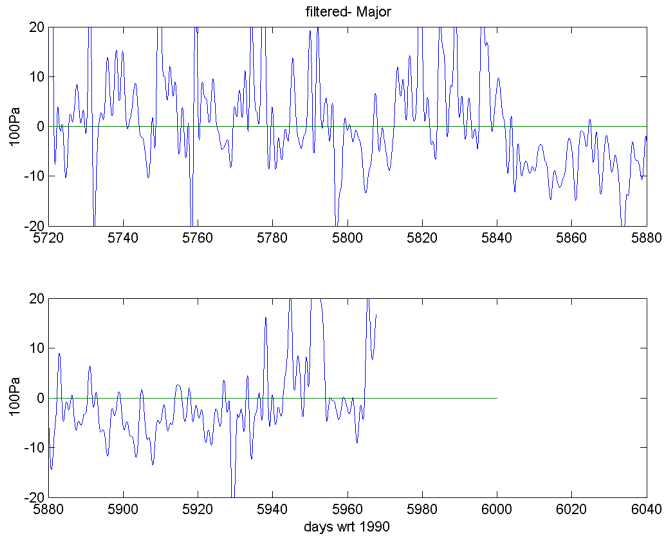

Figure 6.3.2. Major component of wind stress (Thompson Filtered; Units 100Pa). The major component was resolved to be that along the shelf and is positive to the S.E.

After November, the gulf waters warm (Figure 6.1.5) due to solar heating. In Figure 6.3.3, we present the temperature from M5 along with a synthetic time series based on the net daily heat flux for the region and an assumed depth of 20 m (see Appendix B). The synthetic time series is based on the daily temperature changes so determined and an assumed initial temperature from the M5 mooring: taken on December 6th 2005 (JD 5818).

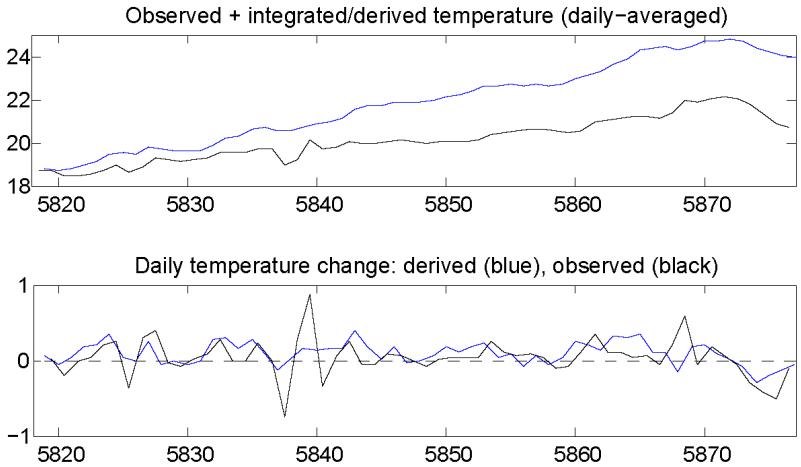

Figure 6.3.3. Upper panel: observed temperature at Mooring 5 in the TFZ (black line) and predicted temperature based on modelled heat flux assuming the same starting temperature (blue line). Bottom panel: Daily changes in temperature for the observed and predicted time series. The start and end dates (days 5818 and 5877) are 6 December 2005 and 3 February 2006.

As is evident, part of the daily temperature changes can be explained by local solar heating. The general increase in temperature is also captured, although the simple model leads to higher temperature than observed.

By December 28th, 2005 (JD 5840), the winds reverse to become upwelling favourable for the shelf (Figure 6.3.2) and remain so until the end of February (JD 5935). There is no dramatic drop in mooring temperatures following the onset of shelf upwelling, although the cooler temperatures observed (Figure 6.3.3) may result from a combination of solar heating and inflow of cool upwelled water. The strong upwelling winds on JD 5875 (Figure 6.3.2) coincide with a marked drop in temperature at all moorings and the simple solar cooling model is only able to account for half of the 1.5 ˚C drop in temperature at this time (Figure 6.3.3).

There is evidence that some of the shelf upwelled water is reaching the eastern side of the TFZ. In Figure 6.3.4, we present SST for February 3rd (JD 5877). As can be seen, the gulf waters (warmed by solar heating) are preferentially cooled on the eastern side of the gulf. The path of the upwelled plume follows that from previous studies (eg., Middleton and Bye 2007) and it is possible some upwelled water moves into the TFZ as a sub-surface plume.

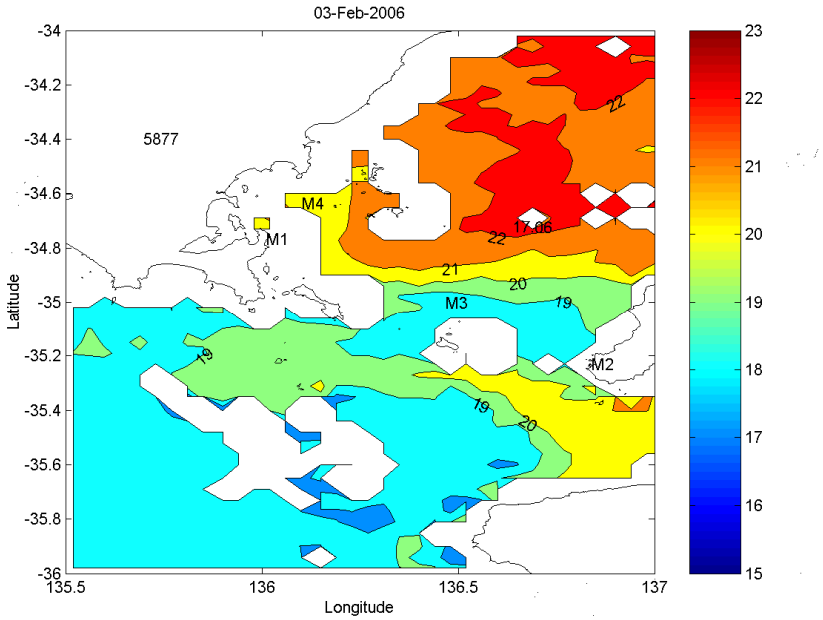

Figure 6.3.4. SST (MODIS) for February 3rd, 2006 (JD 5877).

Transects of temperature and salinity for February 11th 2006 are presented in Figures 6.3.5 and 6.3.6. The transects for temperature provide marginal evidence of upwelling with cooler, fresher water at the bottom and at the eastern side of the transect and close to M4 (boundary). There is also evidence of stratification with a 15 m deep surface mixed layer.

Evidence of evaporation comes from the denser water found on the western transect side that lies in shallower water. This coastal heating and brine water formation is well illustrated in the April 21st 2006 transect shown in Figures 6.3.7 and 6.3.8. The additional salt (0.9 psu) makes the water denser than that offshore with an offshore sub-surface plume structure: the warmest water is at the bottom.

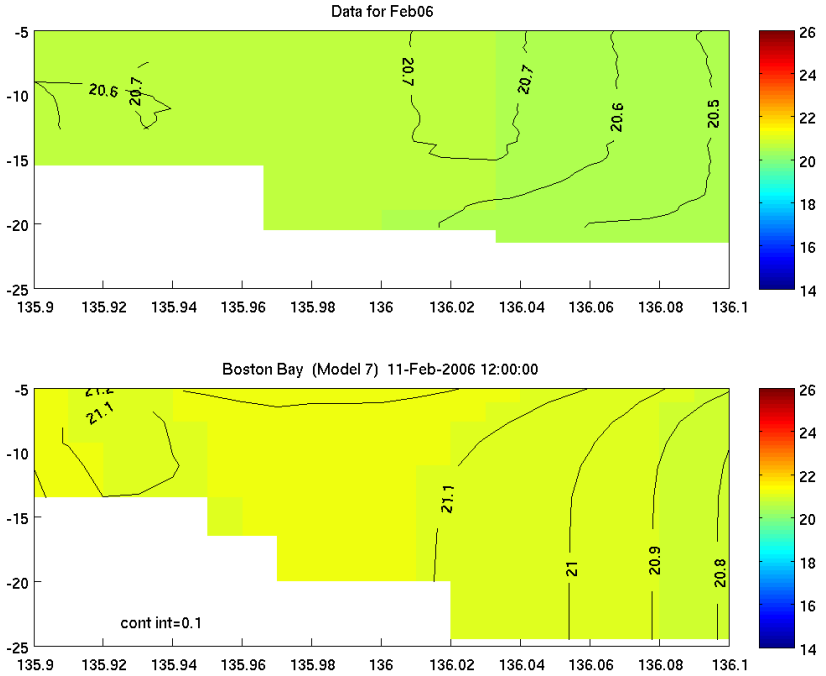

Figure 6.3.5. Upper Panel: observed temperature for February 11th 2006. Lower Panel: model temperature for the same day (12 noon). The vertical scale indicates depths in meters. The horizontal scale is in degrees longitude.

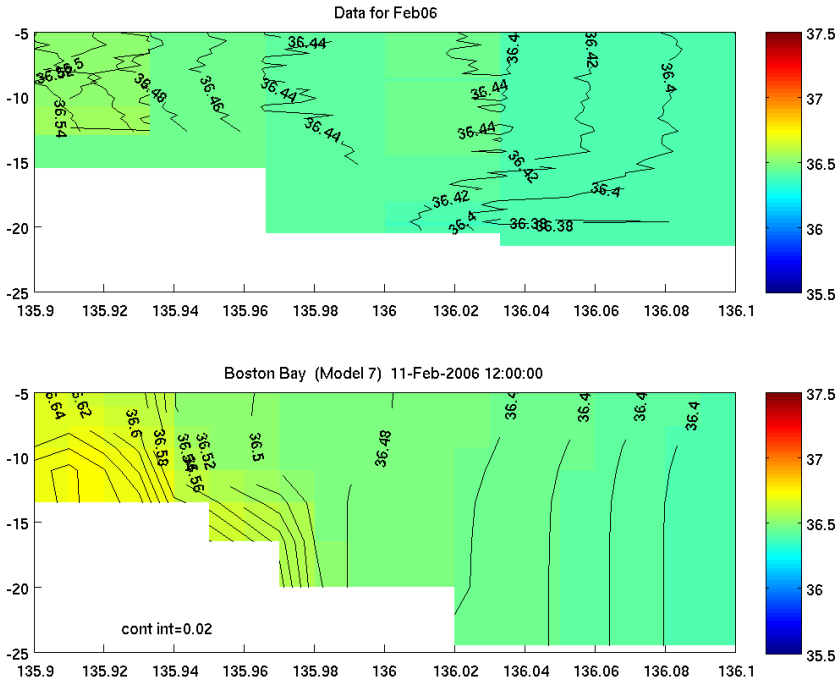

Figure 6.3.6. Upper Panel: observed salinity for February 11th 2006. Lower Panel: model salinity for the same day (12 noon). The vertical scale indicates depths in meters. The horizontal scale is in degrees longitude.

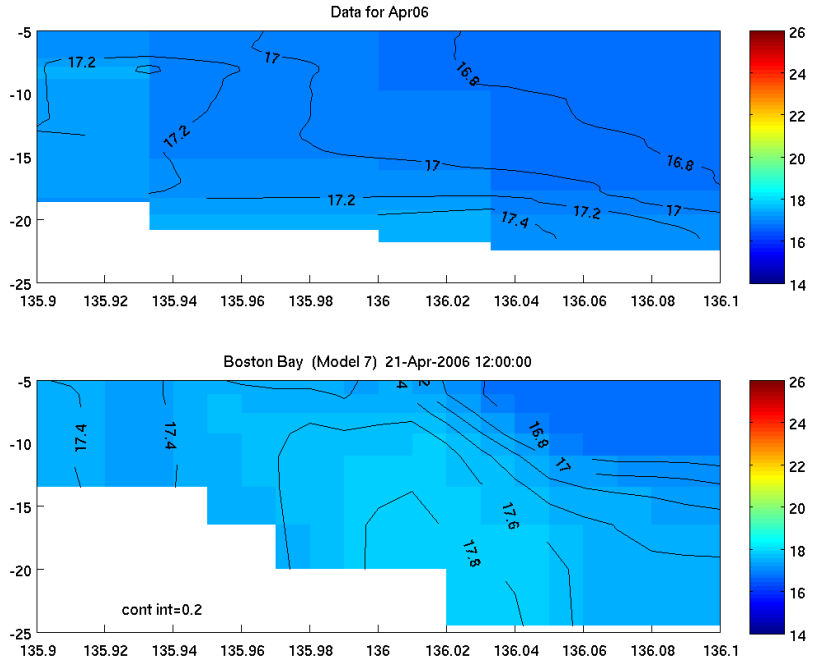

Figure 6.3.7. Upper Panel: observed temperature for April 21st 2006. Lower Panel: model temperature for the same day (12 noon). The vertical scale indicates depths in meters. The horizontal scale is in degrees longitude.

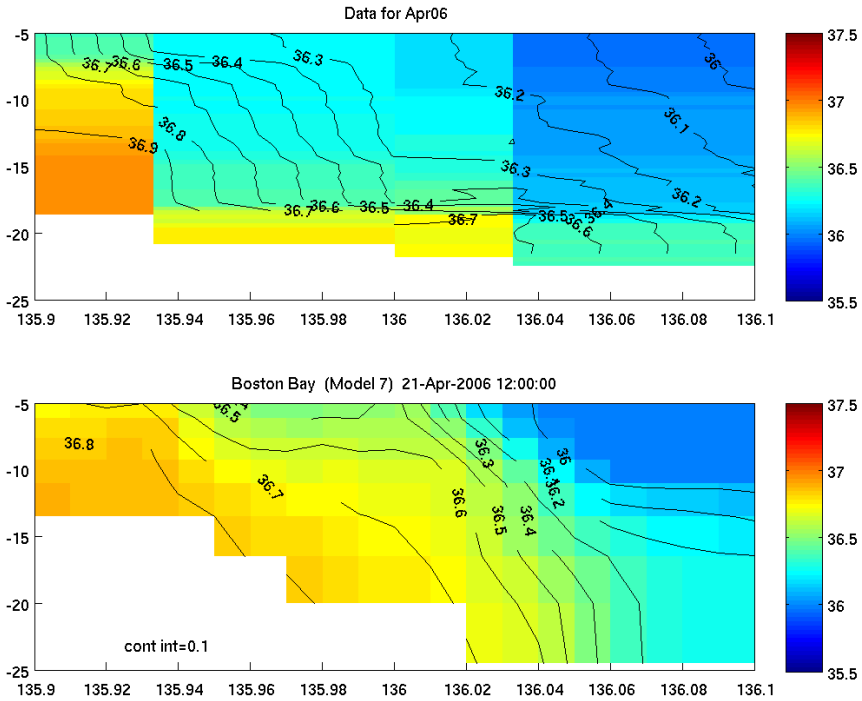

Figure 6.3.8. Upper Panel: observed salinity for April 21st 2006. Lower Panel: model salinity for the same day (12 noon). The vertical scale indicates depths in meters. The horizontal scale is in degrees longitude.

After April, the atmospheric cooling begins to dominate. The transect data for June 20th 2006 are presented in Figures 6.3.9 and 6.3.10 and indicate cold dense water formation at the coast that flows to the east as a 2-3m deep bottom plume. Isotherms near the coast are vertical indicating convective over-turning. Salinity is largely homogeneous.

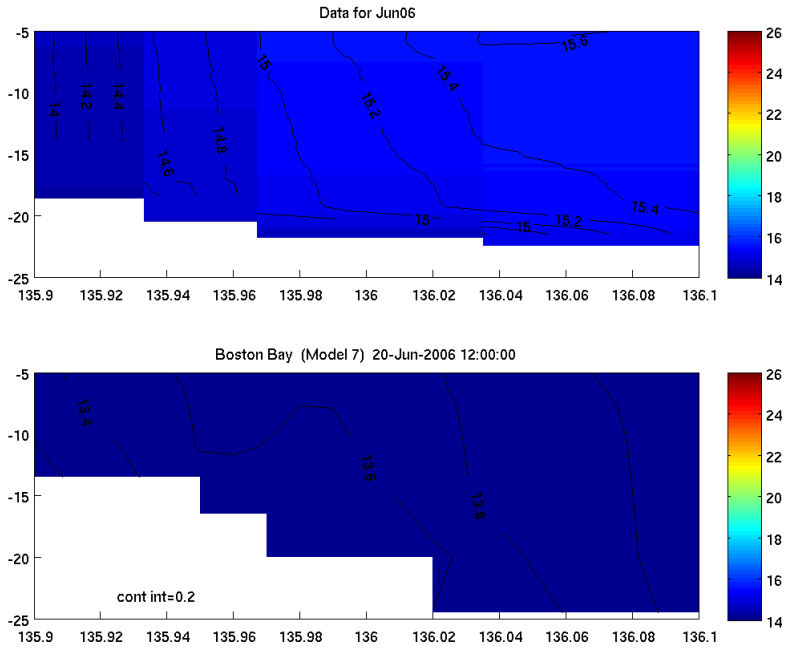

Figure 6.3.9. Upper Panel: observed temperature for June 20th, 2006 (JD 6012). Lower Panel: model temperature for the same day (12 noon). The vertical scale indicates depths in meters. The horizontal scale is in degrees longitude.

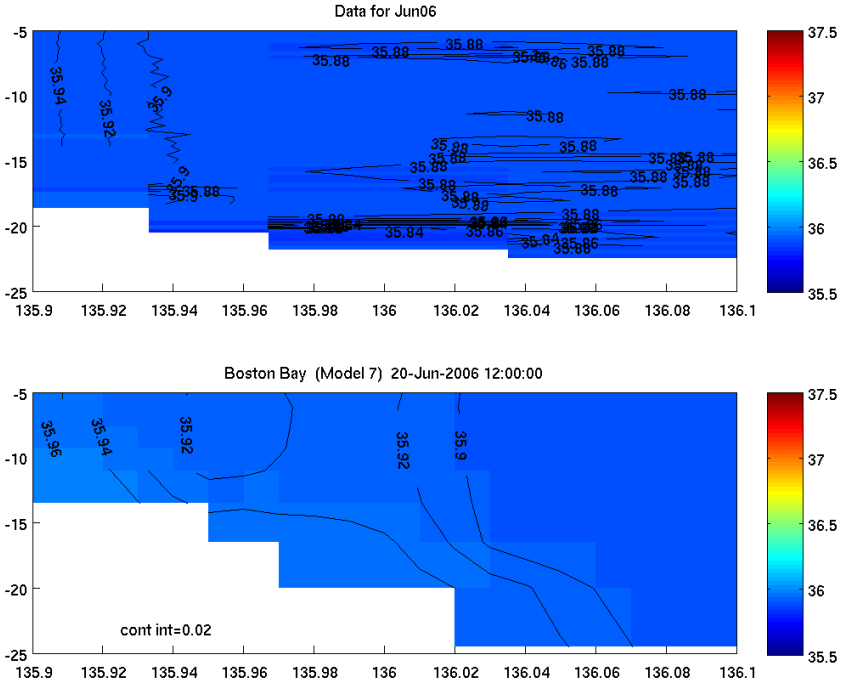

Figure 6.3.10. Upper Panel: observed salinity for June 20th, 2006 (JD 6012). Lower Panel: model salinity for the same day (12 noon). The vertical scale indicates depths in meters. The horizontal scale is in degrees longitude.

The spatial extent of this coastal cooling is illustrated by the SST image (Figures 6.3.11 and 6.3.12). A cyclonic (clockwise) gyre is evident at the large scale as was inferred by Lennon et al (1987).

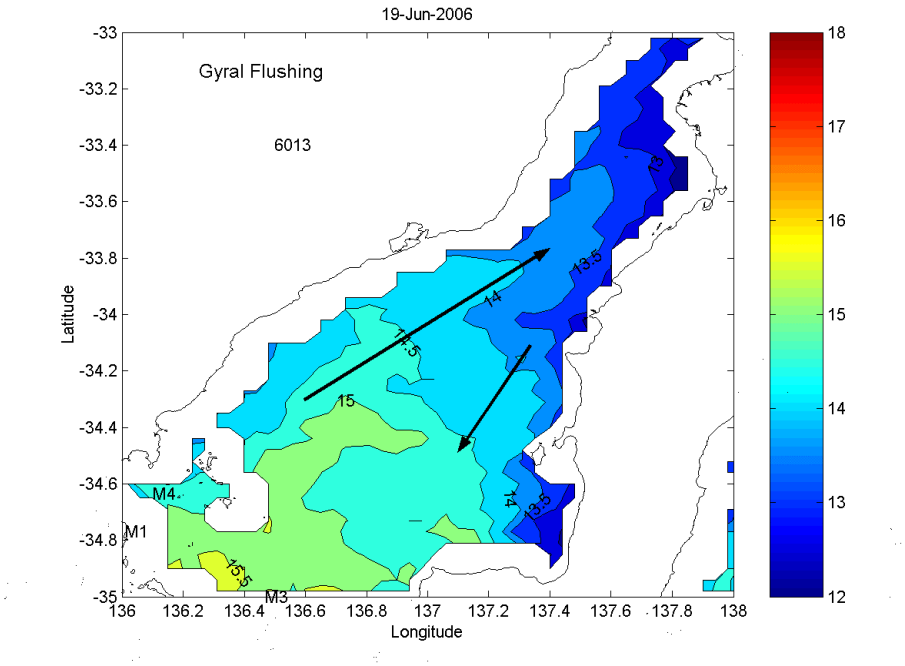

Figure 6.3.11. Sea Surface Temperature (MODIS) for the 19th June 2006(JD 6013). The arrows indicate the expected circulation.

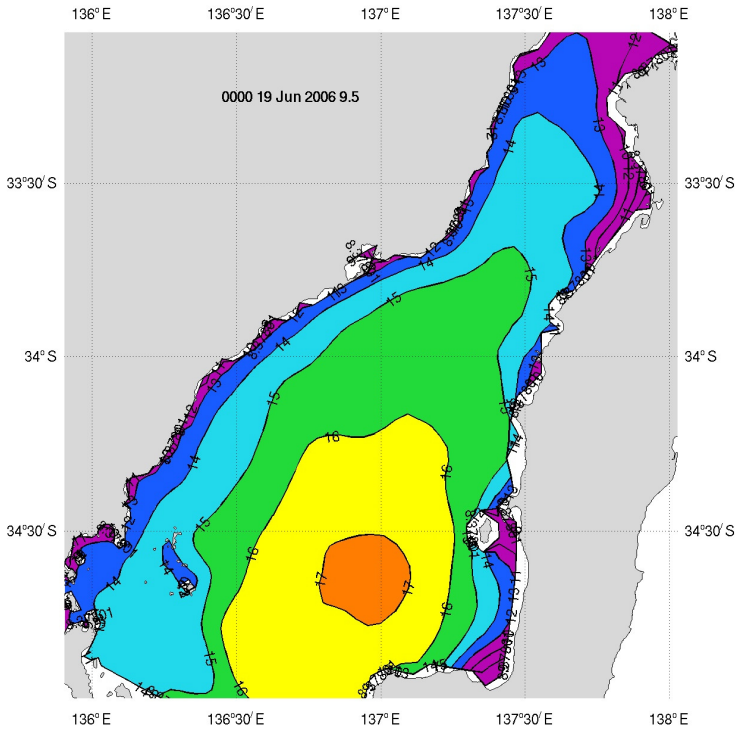

Figure 6.3.12. Modelled Sea Surface Temperature (MODIS) for the 19th June 2006(JD 6013).

6.4. Sea Level Data

The Low-frequency Signals:

Sea level variations are dominated by the tides with amplitudes of up to one meter in the TFZ region (Figure 7.1.1). These will be discussed below. Of interest also is the low-frequency variability that arises from local and remote winds and for periods 3-20 days – the weather-band. While the tides are deterministic (repeatable and predictable), the weather-band signals are less so. Indeed, as we will see, the displacement of fluid parcels that arises from the weather-band circulation exceeds that due to the stronger tidal velocities.

To examine these signals, the sea level data from moorings M4 and M5 were low-pass filtered using the Thompson (1983) algorithm and the results presented in Figure 6.4.1 (the black curves). As can be seen, the signals are dominated by 3-20 day variability with amplitudes of up to 50 cm. Larger variability is found during winter.

Also evident from Figure 6.4.1, is the similarity of sea level signals at the three mooring sites. A similar result is found for the gulf mouth sites. An analysis of the sea level data from moorings M4 and M5 indicates that the geostrophic velocities for the TFZ region are small and less than 5 cm s^{-1} or so. These results will be discussed further in section 6.6 below. For the gulf mouth, differences of 5-10 cm can lead to substantial currents of 20 -30 cm s^{-1}, as discussed next and in Appendix A.

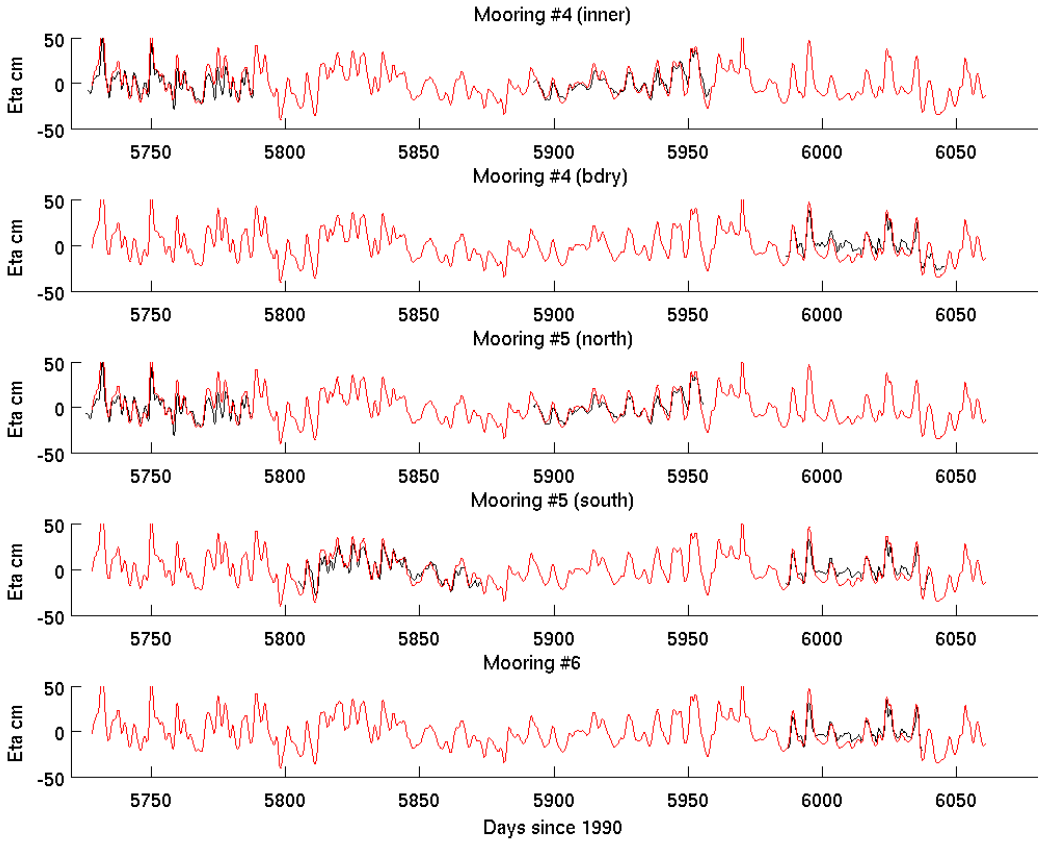

Figure 6.4.1. The low-passed filtered sea level data from the M4, M5 and M6 moorings. Red curve = modelled, black curve = measured.

Circulation at the Gulf Mouth.

As noted, the sea level records from M1 and M2 were found to have datum shifts of 10 –20 cm brought about by re-deployment of the instruments at slightly different depths after servicing (Table 6.1). However, in Appendix A, an analysis of the data suggests a simple conceptual model that likely explains net in/out flows through the gulf mouth that appear to be driven in part by the alongshore wind stress. The data also suggests the existence of anticyclonic (cyclonic) circulation at the gulf mouth during periods of alongshelf upwelling (downwelling) winds. These results are in qualitative agreement with recent numerical studies elsewhere (Middleton and Teixeira 2008).

6.5. Velocity Mooring Data

Hourly averages of velocity data from bottom mounted ADCPs at moorings M4 and M5 were calculated. For M4, currents were measured in 69 bins (each of 0.5 m depth) from the bottom (offset for instrument blanking and mooring infrastructure) to the surface. For M5, currents were measured in 24 (0.5m depth) bins but only from the bottom to 12 m above the sea floor. Note that both moorings were shifted to different sites for the 2nd and 4th deployments (see Figure 6.1.2).

Depth-Averaged Velocities.

As a first step, the data was averaged in the vertical and the Thompson (1983) filter applied. With the filtered data so determined, residual (tidal band) time series were then obtained: simply the residual data being the raw data less the filtered data. Plots of the tidal band signals are presented in Figure 6.5.1 for the M4 inner site. Results for the M4 boundary site are similar. Results for M5 (not shown) are similar but reduced in magnitude to 5-10 cm s^{-1}.

For the east/west and north/south components presented in Figure 6.5.1, it is evident that the latter dominate with speeds of 30 cm s^{-1}. The fortnightly dodge tide is also evident.

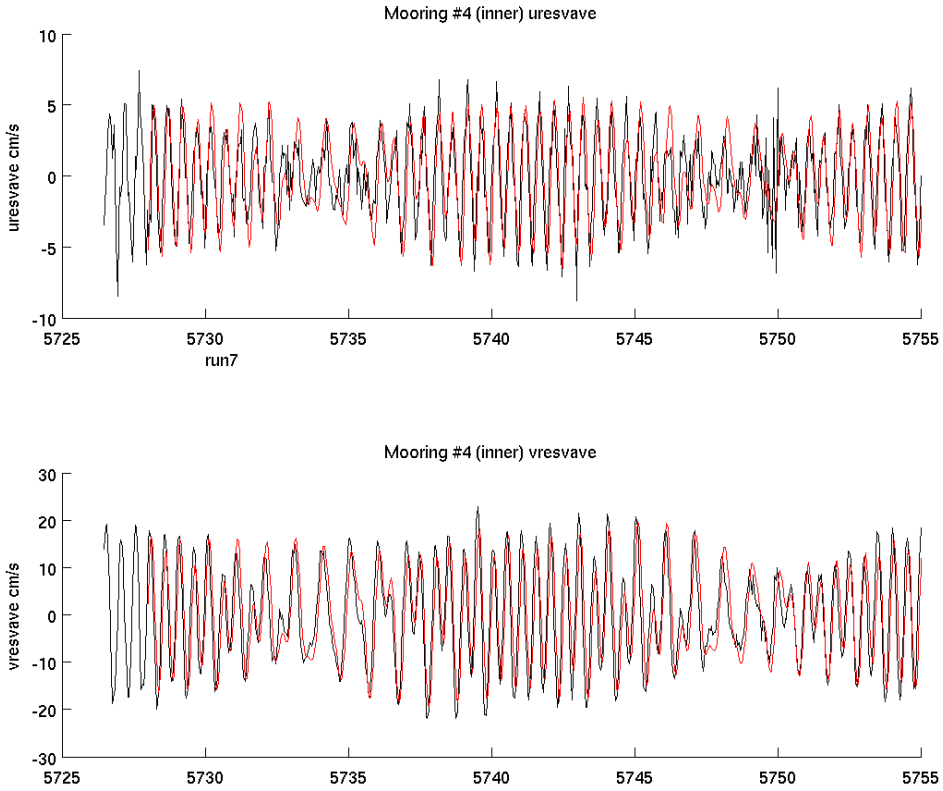

Figure 6.5.1. Upper Panel: the (east/west) tidal-band velocity (depth-averaged) for the M4 inner site. Black values are data while the red values are from the fine scale numerical model. Positive values are to the east. Lower Panel: as in the upper panel but for the (north/south) tidal-band velocity. Positive values are to the north. Note the change of limits on the y- axis.

The filtered depth-averaged velocity field is shown in Figure 6.5.2, again for the inner sites. As is evident, there is again variability in the 2-30 day band. Strikingly, the current speeds of the filtered (weather-band) data are much smaller (< 5 cm s^{-1}) than those of the tides (~ 30 cm s^{-1}) shown in Figure 6.5.1. The small current speeds are, however, consistent with geostrophic currents estimated from the M4 and M5 sea level data.

Results were also obtained for the other sites (including M5) and were similar in character to those shown in Figures 6.5.1-6.5.2, with amplitudes 5 cm s^{-1} or less.

The weather-band currents within the gulf are much smaller than those typically found on the shelf (~ 25 cm s^{-1}). The reason for this is that the coastal boundary conditions of no normal flow penetrate over a distance of the deformation radius which is around 120 km and comparable to the gulf width (Middleton and Teixeira 2008). These authors have also shown that larger weather-band currents will be found in very shallow water (< 5 m), since the deformation radius is effectively smaller.

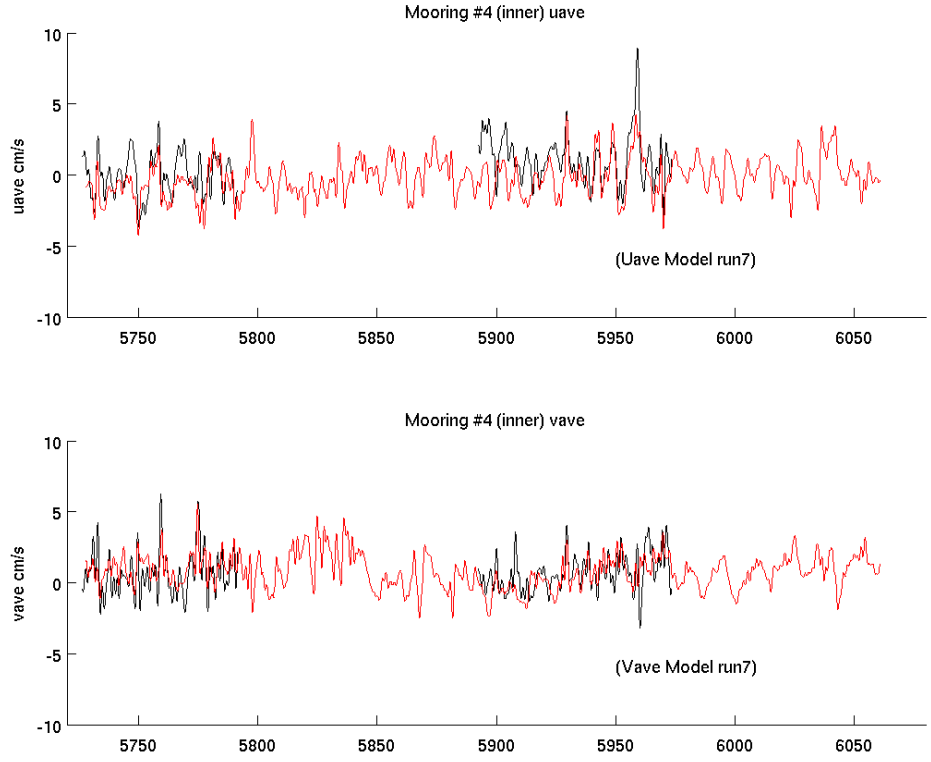

Figure 6.5.2. Upper Panel: the (east/west) weather-band velocity (depth-averaged) for M4 at the inner site. Black values are data while the red values are from the fine scale numerical model. Positive values are to the east. Lower Panel: as in the upper panel but for the (north/south) weather-band velocity. Positive values are to the north.

The stronger semi-diurnal tidal currents shown in Figure 6.5.1 may be implicated in bottom stirring, particularly when wave action is included. A useful measure of their importance to flushing is the net displacement a water parcel would undergo after ¼ period (3 hrs). For the dominant semi-diurnal tide this distance is 1.4 km. For the weaker weather-band currents, the displacements will generally be larger since they persist over a longer time. For example, a 5 cm s^{-1} current with a 10 day period will displace a water parcel by 7 km over a 2.5 day period: five times that of the tide. Thus, the successful modelling of the low-frequency circulation may be more important to predicting cage flushing and nutrient transport than that of the tides.

Mean Currents and Velocity Shear.

The above presents results for the depth-averaged currents. The mean currents may be important to flushing. In addition, vertical current shear may be important to enhanced shear dispersion and also lead to modifications to bottom stirring and flushing through the cages themselves. To this end, we have calculated statistics for the mean currents, shear and deflections (Appendix C).

Means: In summary, the results for M4 show the mean flow to be small (~ 1 cm s^{-1}) and directed to the north-east for most of the year (Appendix C). Such a flow will displace a fluid parcel by 78 km over a 3-month seasonal period. For M5, the mean flow is predominantly to the south or west with speeds of 2-3 cm s^{-1}, i.e. an onshore flow.

Shear: Shear statistics were calculated for the raw, filtered (weather-band) and tidal band components of the flow. The currents in the bottom ADCP bin (~ 1m from the bottom) for M4 were found to be deflected to the left of the depth-averaged currents - an indication of Ekman dynamics. Indeed the results in Appendix C suggest that frictional boundary layer dynamics are important at both the surface and bottom. In summary, the statistics of the depth-averaged velocities ($\bar{u}, \bar{v}$) for M4 are given in Table 6.2 for each deployment period (D=1, 2, 3 or 4).

Table 6.2. $\sqrt{<\bar{u}^2>}, \sqrt{<\bar{v}^2>}$: rms of depth-mean velocity components at M4. The braces <> denote a time average for the given deployment period.

	Unfiltered				Low Frequency				Tidal Band			
D	1	2	3	4	1	2	3	4	1	2	3	4
u	3.3	3.1	3.7	3.4	1.4	1.8	2.0	1.7	2.9	2.5	3.1	3.0
v	10.8	10.0	10.9	12.7	1.7	1.5	1.4	2.6	10.7	9.9	10.8	12.4

D: Deployment; *u* and *v* in cm s^{-1}

For the unfiltered data, the rms (root mean square) variability is largest in the north/south direction and largely accounted for by the tides. Now consider the rms shear statistic:

$$\sigma^{u}{}_{z}(t) = \sqrt{\frac{1}{h}\int_{-h}^{0}(u-\bar{u})^2\,dz}$$

(and similarly for *v* component) and its time average: $<\sigma^{u}{}_{z}(t)>$. Results for the later statistic are shown in Table 6.3.

Table 6.3. $<\sigma_z^u(t)>, <\sigma_z^v(t)>$: time averages of standard deviations along z-axis at M4.

	Unfiltered				Low Frequency				Tidal Band			
D	1	2	3	4	1	2	3	4	1	2	3	4
u	5.0	21.7	7.1	10.6	1.7	2.6	3.4	3.9	4.2	4.9	5.9	3.8
v	11.3	37.6	11.1	23.7	1.6	1.3	1.4	1.8	14.6	13.8	16.3	10.9

D: Deployment; *u* and *v* in cm s^{-1}

The results show that the rms shear is as large as or larger than the variability of the depth-averaged velocities in Table 6.2 for the raw, filtered and tidal band signals.

For M5, the results show the rms depth averaged variability to be much smaller in the tidal band (~ 3-5 cm s^{-1}), although the shear is again comparable to this average (Appendix C).

Finally, we consider a progressive vector diagram (pvd) using the filtered data from the M4 site and second deployment period that covers the wintertime wind conditions (predominantly from the west) to summertime upwelling conditions (predominantly from the south-east). The pvd is a vector plot of the distance a fluid parcel would travel assuming its velocity is given by the (fixed point) mooring (or wind) data.

The pvd in Figure 6.5.3 shows the surface currents starting at zero displacement in x and y on 6th December 2005 (JD 5818 in the figure) and proceeding to 3rd February 2006 (JD 5877).

The surface flow was generally to the north or northeast throughout the summer period, with no pronounced change in direction during the deployment period.

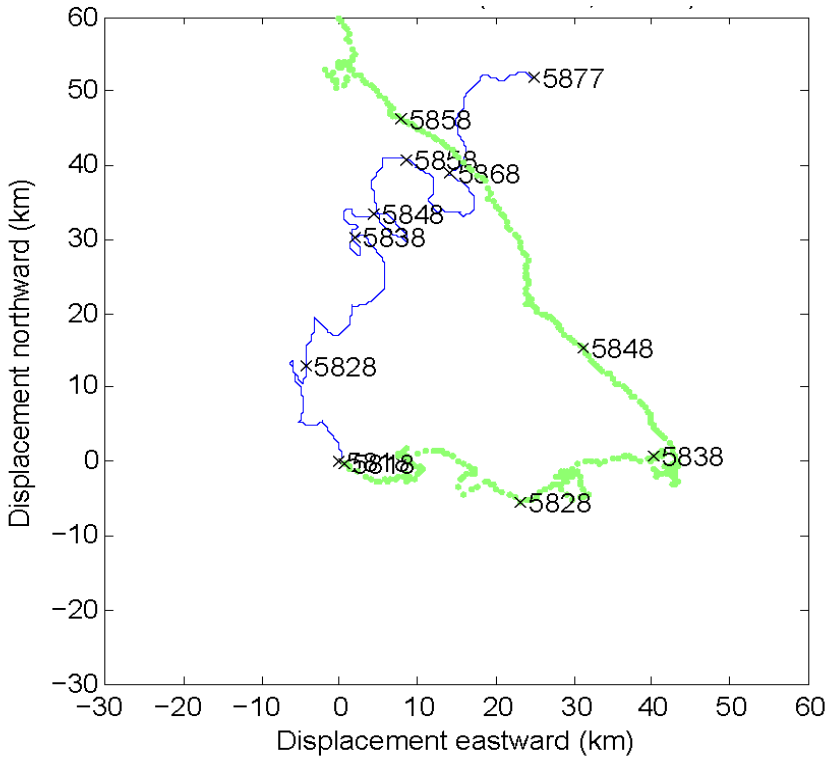

Figure 6.5.3. Progressive Vector Diagram of near-surface currents at Mooring 4 (blue line). The green line is the predicted "surface drift" based on 2% of the local winds. The times are in Julian Days since 1990. and begin (JD5818) on December 6th 2008.

The surface drift shown is that based on a simple empirical formula, which states that the water within a meter or two of the surface moves in nearly the same direction as the wind, at approximately 2% of the wind speed. Essentially, it gives an integrated measure of the wind and direction. Over the first 22 days, the winds are directed to the east. At JD 5838 (December 28th), the winds shift to become directed to the north-west and are typical of those for summer (shelf upwelling). Paradoxically, the surface currents are directed to the north/north-east and remain so regardless of the wind direction.

The flow at the bottom (Figure 6.5.4) is to the northwest for the first 20 days and approximately opposite to the direction of the winds. That is an onshore (local upwelling) flow is found. As the winds change direction, so does the bottom current, becoming directed to the east and more or less in the opposite direction to the surface winds: local downwelling.

These results (and those above for the CTD transects) indicate that the shear in the oceanic velocity field can be large and that local winds can lead to on/offshore flows and associated upwelling and downwelling. The model results will illustrate this further below.

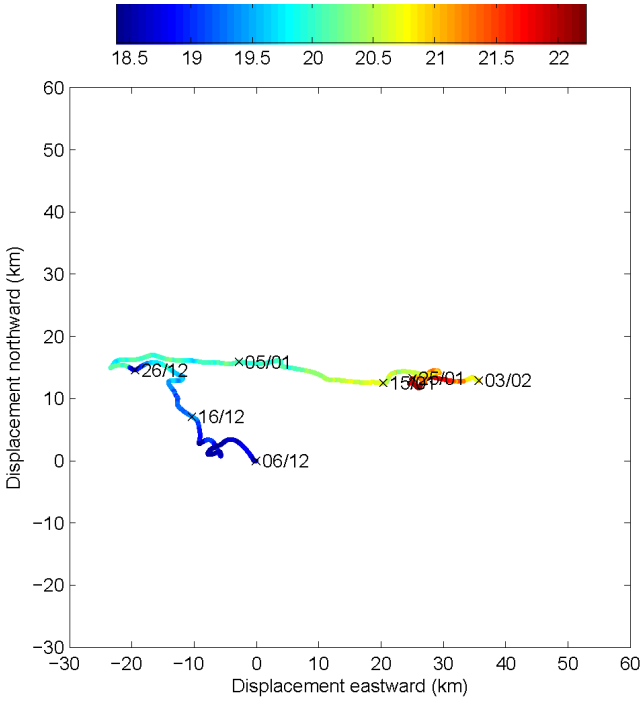

Figure 6.5.4. Progressive vector diagram of near-bottom currents at Mooring 4. The times (December 2006 - January 2006) are indicated by dd/mm. The colour gives the near-bottom temperature from the M5 mooring at the dates indicated: colour bar at top of figure

7. Calibration

The model was primarily calibrated against sea level, temperature and salinity. The latter two variables reflect the larger scale circulation, which is of interest in this study. Elevation calibration provides confidence that tidally driven flow is accurate. Comparisons were also made to velocity measurements obtained from the ADCP, however, these comparisons are not always informative since ADCP measurements often reflect localized small-scale processes, which may not be captured by the model. Nonetheless, a comparison with the data will be made.

7.1. Regional Model

The model parameters were tuned so that modelled solutions optimally compared to data collected during the field campaigns (the calibration procedure). Model – data comparisons are outlined below.

Sea level measured at Port Lincoln, Wallaroo and Whyalla (courtesy of Flinders Ports) was compared to modelled sea level for December 2005 (Figure 7.1.1). The low pass filtered (long period) sea level for these two sites is displayed in Figure 7.1.2. This figure shows that the model performs well in terms of sea level, capturing the semi-diurnal tidal character and neap spring cycles, in addition to the long period fluctuations.

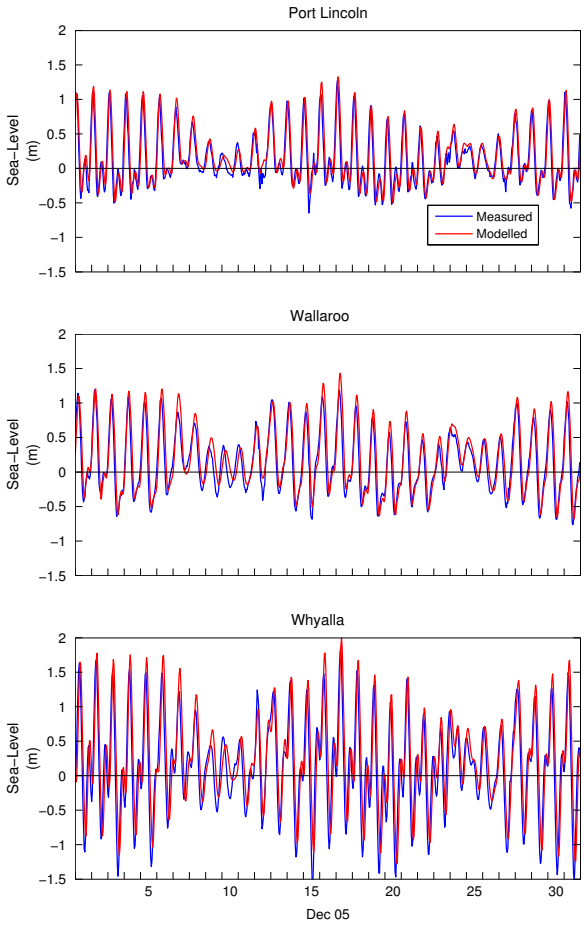

Figure 7.1.1. Modelled and measured sea level at Port Lincoln, Wallaroo and Whyalla.

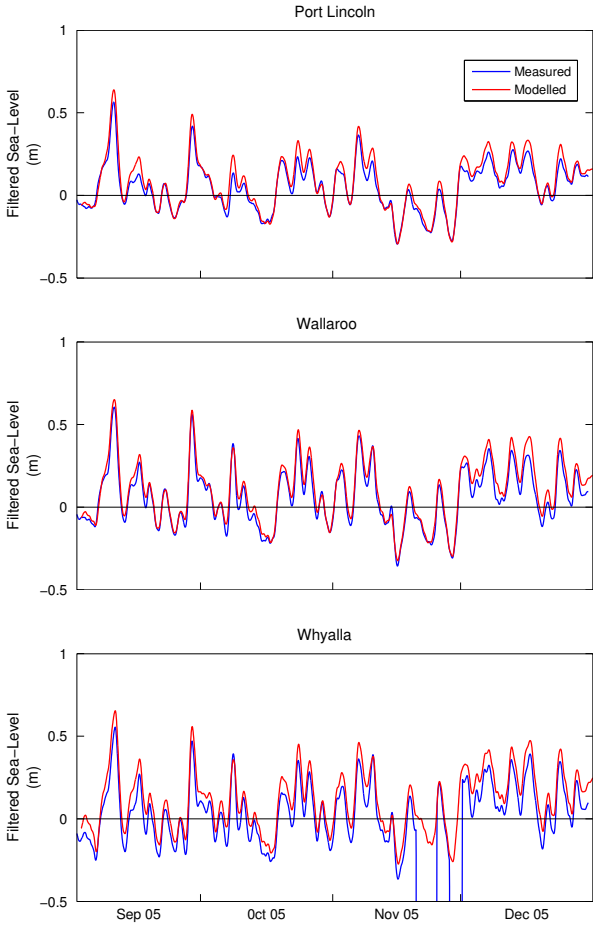

Figure 7.1.2. Modelled and measured low frequency sea level.

High evaporation within Spencer Gulf results in warm (> 17 ºC), salty (> 37 psu) water residing within the gulf. These waters are density compensated resulting in no significant horizontal density gradients. The onset of autumn leads to cooling of the salty water in the head of the gulf, increasing the density to result in density currents flowing out of the gulf on its eastern margins, with compensating inward flow at the surface on the western side. This dense outflow has been captured by Lennon et al., (1987) on 16-23 June 1986, and is reproduced here as Figure 7.1.3. The bottom salinity diagnosed from the model on 29 June 2006 is shown in Figure 7.1.4 for comparison. It is observed that the dense gravity plume is indeed captured by the model, possessing features comparable to that of observation.

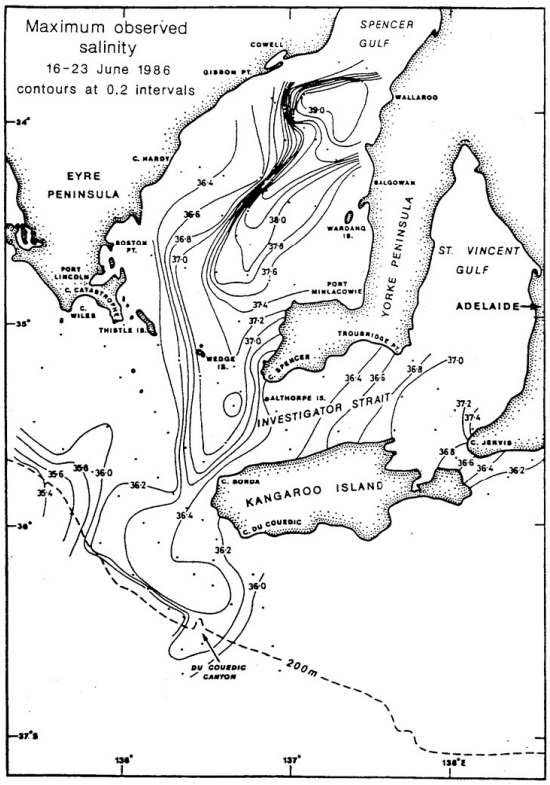

Figure 7.1.3. Maximum salinity throughout the water column for 16-23 June 1986. Reproduced from Lennon et al. (1987).

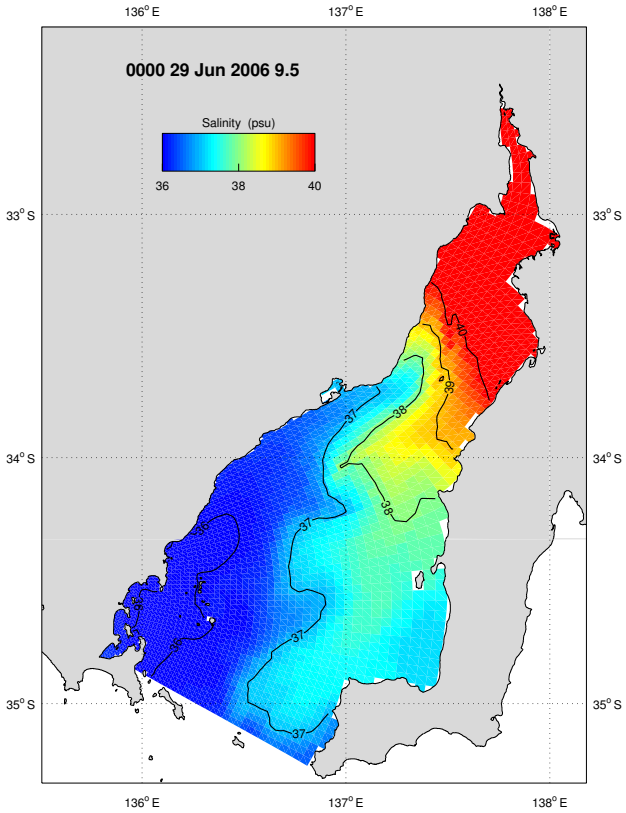

Figure 7.1.4. Model bottom salinity on 29 June 2006.

The temperature and salinity derived from the model at the locations of Moorings 4, 5 and 6 are compared to observation in Figure 7.1.5. The annual variability is well captured by the model both in terms of temperature and salinity. Model temperature is, however, cooler than observation towards the end of the simulation. This is attributed to the coarse resolution of the regional model in the shallower parts of the TFZ under-resolving differential heating during summer in conjunction with large numerical diffusion. This leads to too little heat input into the shallows, and excessive mixing of this heat with the deeper waters of the TFZ.

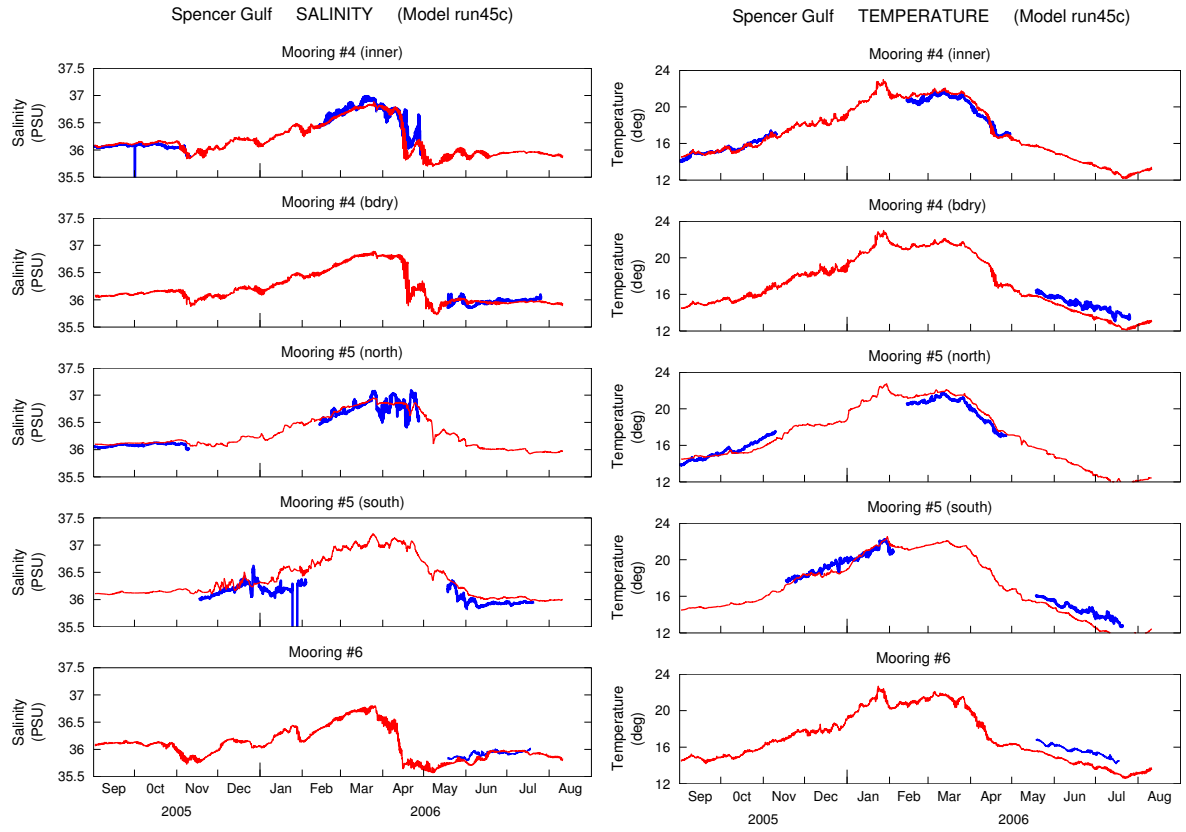

Figure 7.1.5. Comparison of modelled (red) and measured (blue) temperature and salinity at mooring locations in the TFZ.

Overall, the regional model is performing well in terms of sea level, temperature and salinity, with the spatial distribution, magnitude and timing of events consistent with those observed in the measured data. This allows data corresponding to these variables to be extracted from the regional model for use as boundary forcing for the local model.

Finally, we present plots of the time averaged circulation as inferred from the regional scale model. These plots (Figure 7.1.6 to 7.1.7) illustrate the larger scale depth-averaged flow for summer (January – March), and winter (April-August). A one month delay is added to the seasons since the summertime upwelling winds (and associated circulation) did not begin until December 28th 2005. As expected, the circulation for spring, autumn and winter is characterized by a clockwise circulation with an inflow (outflow) on the western side of the gulf mouth. This flow is predicted by other studies and would match the south-eastward flow along the adjacent shelf that is driven by the predominantly downwelling favourable winds (see the review Middleton and Bye 2007).

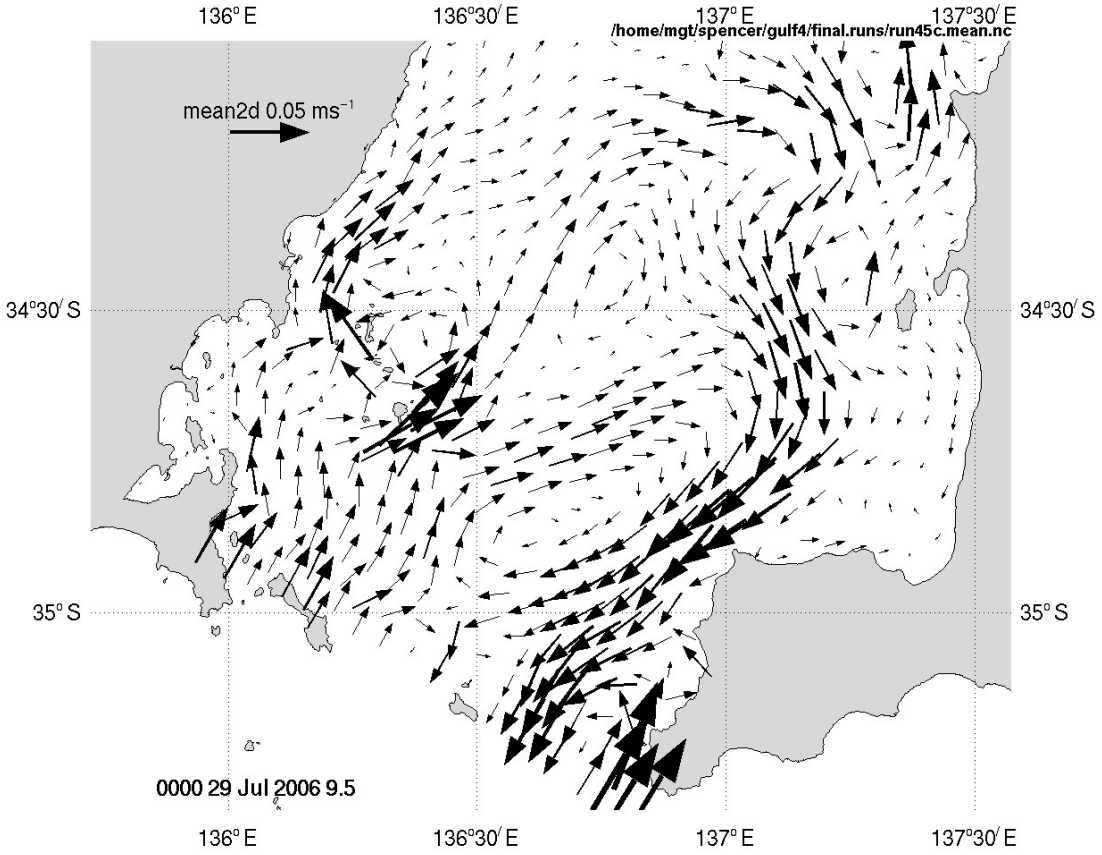

Figure 7.1.6 The time- and depth-averaged flow for July 2006. A legend vector of length 0.05 m s^{-1} is indicated.

Surprisingly, the results for summer (Figure 7.1.7) also show a clockwise circulation near the mouth of the gulf, opposite to that expected (eg., Middleton and Platov (2003), Middleton and Teixeira (2008)), and to observations of cold water intrusions into the eastern gulf mouth (see Figure 6.3.4). Moreover, in Appendix A, we show that an anti-clockwise (clockwise) circulation is consistent with the gulf-mouth sea level data when alongshelf winds are upwelling (downwelling) favourable. Indeed, the explanation for this anomalous result may involve the boundary condition adopted for weather-band sea level variability. This necessarily assumed a linear relation across the gulf mouth and implies that the model is relaxed towards a (geostrophic) velocity field that is directed either into or out of the gulf but not both at the same time. This precludes the in/out flow needed for a clockwise or anticlockwise gyre. Inspection of Figure 7.1.7 suggests that the boundary condition at the gulf mouth acts to "block" the inflow/outflow of the evident clockwise gyre. On the other hand, the results for winter in Figure 7.1.6 suggest the boundary condition is "well behaved".

At any rate, we note that the model does have reasonable predictive skill for the TFZ region for both the mean and weather-band flow.

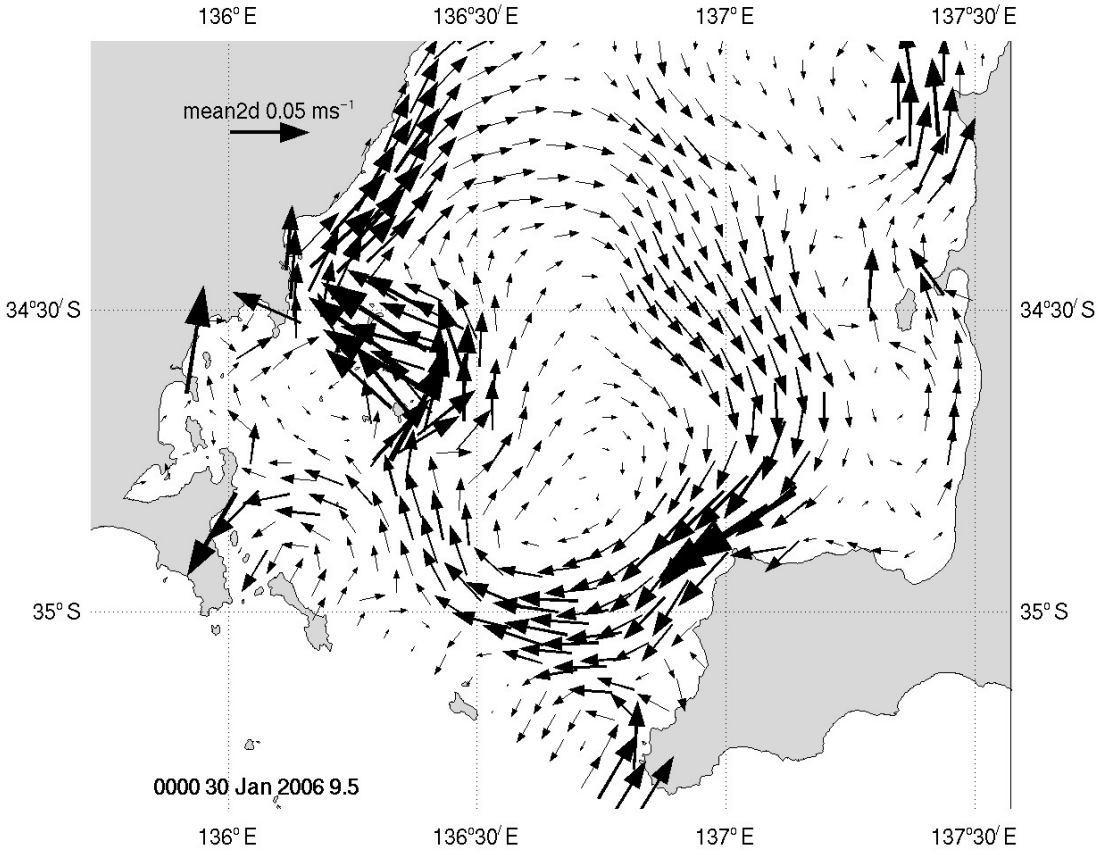

Figure 7.1.7 The time- and depth-averaged flow for January 2006. A legend vector of length 0.05 m s^{-1} is indicated.

7.2. Local Model

Model results obtained from the high-resolution TFZ (local) model are here compared with the data collected. We largely follow the order of material presented in Section 6.

Temperature and Salinity

Time series of temperature and salinity were obtained at each of the mooring sites and the results are very similar to those obtained from the regional model that are presented in Figure 7.1.5. No real improvement in adopting the local model is found for these variables although we again note that the results for temperature are considerably affected by the local heat flux, which is largely model independent.

Model results corresponding to the CTD transect data were also obtained and are presented in Figures 6.3.5-6.3.10. For February, the local model results are broadly similar to the data (Figure 6.3.5-6.3.6) in that warmer, saltier water is found nearer the coast: evidence of near bottom upwelling of colder, fresher water is not found.

For April, (Figure 6.3.7-6.3.8), both model and data show the formation of a near bottom coastal plume of warm, salty water where water is warmest away from the coast.

For June, (Figure 6.3.9-6.3.10) the model is able to reproduce the formation of a dense cold, salty water plume near the coast. The model salinity agrees well with the data while the temperature is almost 2 ºC cooler than the data.

Sea Level and Currents.

Both the local and regional models reproduce sea level variations in the tidal band reasonably well. For the low-pass filtered data, this is also the case (Figure 6.4.1).

A comparison of the local model tidal currents with data is shown in Figure 6.5.1 for the M4 inner site. The model is able to reproduce both the timing and amplitude of the observed tide extremely well at this site. We note that the comparison is less favourable at the M4 site that lies adjacent to the local model open boundary. The explanation here is that the open boundary condition does not locally require that both the normal and tangential velocities exactly match: mass transport between the regional and local models is conserved through the open boundary so that results from the local model farther from the boundary are in good agreement with the data. The model tidal band results for M5 are also in good agreement with the data.

A comparison of the local model results for the M4 inner site and for the weather-band signals is made in Figure 6.5.2. The results show the model to have reasonable predictive skill. As noted, errors here can arise simply from inaccuracies in the adopted topography and this may be the cause of the poor predictive skill found for the weather-band at the M5 sites. Moreover, errors in the open boundary condition for weather-band sea level will lead to loss of predictive skill.

The mean depth-averaged currents estimated from the model are in reasonable agreement with the data (Appendix C). At the M4 sites a north-east circulation of 2 cm s^{-1} is generally found in the data and this is in qualitative agreement with the model (see Figures 8.2.1-8.2.4 below). At the M5 sites, the data indicates a west to southward mean flow of 2-3 cm s^{-1}, which again is consistent with the model results.

7.3. Sensitivity

During the calibration procedure an assessment of the sensitivity of model parameters and processes was made. This provides insight into the parameters and processes, which may critically affect the model solutions. The calibrations presented in Section 7.1 and 7.2 are the end result of the sensitivity analysis; the key parameters of the calibration procedure and model process requirements are detailed below.

The regional model was found to be sensitive to elevation prescribed at the open boundary, surface heat & salt fluxes, and horizontal diffusion. Once these were optimized and acceptable calibrations achieved for sea level, T and S, similar configurations were applied to the local model to also result in acceptable calibrations. No doubt the local model also exhibits sensitivity to elements that were sensitive in the regional model, however, only the regional model sensitivity is presented here for these elements. Additionally, the local model was found to be sensitive to the treatment of the open boundary condition, which is detailed below.

The most critical process required to be included in the model was the inclusion of atmospheric heat and freshwater fluxes across the ocean surface. The fluxes were computed from standard meteorological measurements (Herzfeld, 2005, Chapter 9). These fluxes added

heat to the system and allowed the temperature solution to realistically mirror the seasonal cycles. The data used in the computation of the heat fluxes resulted in sensitivity in the temperature solution. The best solutions were obtained when meteorological data from Warooka was used to compute the heat flux, as opposed to data interpolated from all the measurement stations (Figure 5.2.1). The choice of bulk scheme used for the latent and sensible heat fluxes also resulted in temperature sensitivity. There are numerous bulk schemes in existence; Blanc (1985) reviews ten schemes and concludes that each scheme provided different results when applied to the same data, highlighting the uncertainty inherent in the bulk method. Best results were obtained using the scheme of Kitaigorodskii et al. (1973), although the schemes of Kondo (1975), Masagutov (1981) and Large and Pond (1981) were also trialled.

The short wave radiation (swr) component incident on the sea surface may be partitioned so that a fraction is input as the surface boundary condition (in addition to the sensible, latent and long wave components) and the remaining fraction is allowed to penetrate the water column, subject to attenuation with depth determined by an extinction coefficient. This partitioning represents the preferential absorption of longer wavelengths of swr within the first few meters (Simpson and Dickey, 1981). A transmission coefficient controls the partitioning; details of the swr parameters optimized for regional and local models are listed in Table 7.1.

Table 7.1. Optimum transmission and attenuation coefficients for short wave radiation.

Model	Transmission (fraction)	Extinction (m^{-1})
Regional	1	0.3
Local	0.85	0.4

Sensitivity was observed to the evaporation gradient from the mouth to the head of the gulf. This was regulated by the pan factors applied at the gulf mouth and head; optimum pan factors for the mouth/head were found to be 0.8/0.9. Sub-optimal pan factor ratios trialled were 0.7/1.0, 0.5/0.9, 0.9/1.0, 0.7/0.8 and 0.7/0.9.

The formation of the density current in the regional model exhibited sensitivity to the value of the horizontal diffusion and background vertical mixing coefficients. The optimized regional model used horizontal diffusivities of $A_H = 20\ m^2s^{-1}$ and background vertical mixing of $V_z = K_z = 1x10^{-5}$. An example of the lack of density current when larger friction was used ($A_H = 200\ m^2s^{-1}$ and $V_z = K_z = 5x10^{-4}$; compare with Figure 7.1.4) is displayed in Figure 7.3.1.

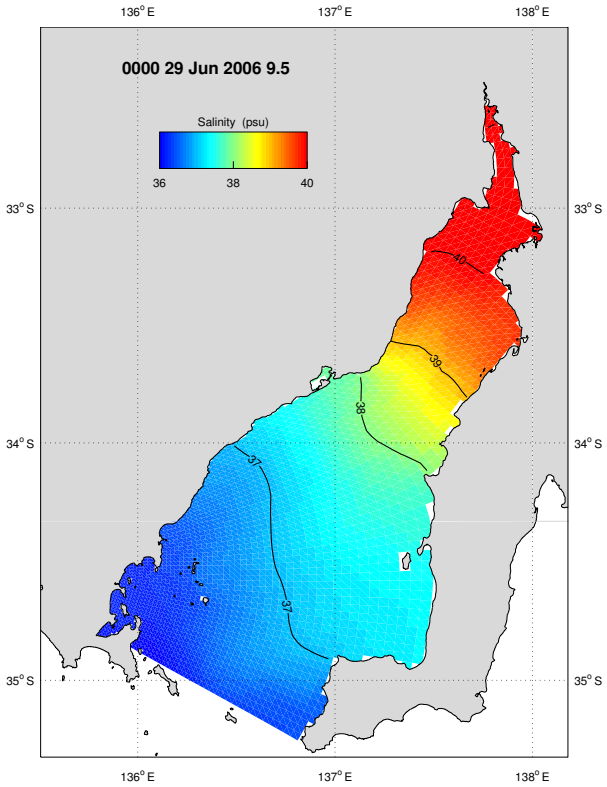

Figure 7.3.1. Model bottom salinity on 29 June 2006 using large friction.

Boundary specification problems were evident on the eastern side of the open boundary, requiring the addition of a radiation condition with relaxation timescale (see Blumberg and Kantha, 1985). These boundary problems are observed in Figure 7.3.2 (a) where the model is simulated without the radiation condition showing spurious currents on the eastern side of the open boundary due to reflection of wave energy at that location. The addition of a gravity wave radiation condition using a relaxation time-scale of 30 minutes is displayed in Figure 7.3.2 (b), where it is observed the spurious currents are absent due to adequate transmission of wave energy. The removal of the spurious currents was sensitive to the choice of radiation condition and length of relaxation time.

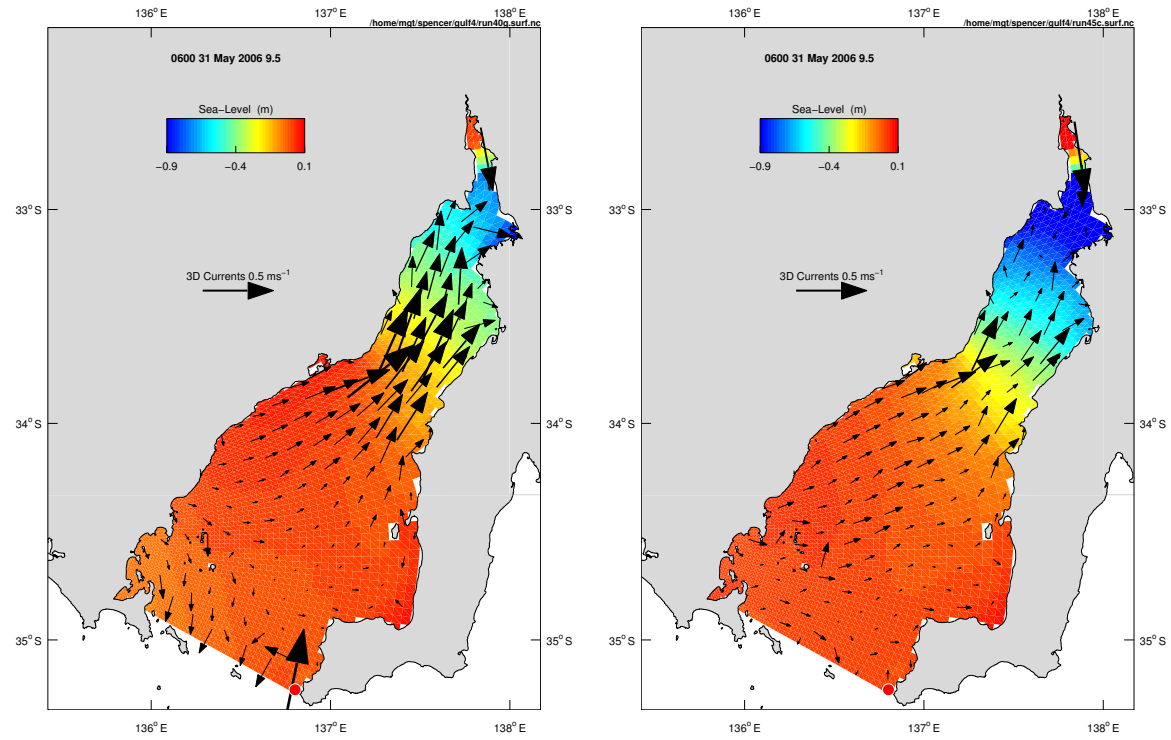

(a) No radiation condition (b) Gravity wave radiation

Figure 7.3.2. Effect of radiation on velocity.

The regional model solutions were also sensitive to prescription of the sea level signal on the open boundary. Sea level was retrieved from moorings 1 – 3 and post-processed to a common datum for each 3-month deployment period. This process assumed zero net geostrophic flow through the boundary over that period. Comparisons of temperature and salinity using this method of prescribing sea level is displayed in Figure 7.3.3, from which significant degradation in the correlation between measured data and model output is observed. This indicates that either the instruments were inaccurately measuring sea level, or the zero net flow assumption is invalid. Note that Moorings 1 and 2 had non-integrating pressure sensors installed from which sea level was retrieved, and it is possible aliasing with the wave-field had occurred. Instrument drift of the datum is also a possibility.

Two approaches were used for forcing the open boundaries of the local model; (a) elevation forcing and (b) velocity forcing, with both using forcing data derived from the regional model. The elevation forcing was used in conjunction with a gravity wave radiation condition and relaxation time-scale of 2 minutes, and the radiation condition of Miller and Thorpe (1981) was used on 3D tangential velocity. To maintain model stability the 2D tangential velocity was required to be clamped to zero (i.e. normal boundary 2D flow only).

The 3D components of velocity were used for the velocity forced method, and depth averages of these data were used for the 2D velocities. The 3D velocities for both normal and tangential components were simply interpolated onto the fine scale open boundary from the regional model solutions. Using this methodology, there is no guarantee that the flux through the open boundary in the regional and fine grid are identical (e.g. due to differences in bathymetry resolution, hence cross sectional area of the open boundary). This may lead to a gradual filling or emptying of the domain over time. To avoid this, the flux prescribed at the normal boundary face that is required to achieve a target elevation via the flux divergence may be inversely computed and added to the normal boundary velocity.

Although both methods of forcing produce similar solutions in terms of temperature and salinity (Figure 7.3.4), the condition of normal-only 2D flow through the boundary resulted in inferior velocity solutions near the boundary (Figure 7.3.5), where tangential components are underestimated (note that for #4(bdry) the normal and tangential components are approximated by east and north components respectively, whereas #6 has these components rotated by ~45^{o} to the open boundary; see Figure 6.1.2). Velocities away from the open boundary in the interior are similar, however, the velocity forced boundary was considered to be superior overall and was preferentially used.

No significant sensitivity was observed to the choice of vertical mixing scheme used.

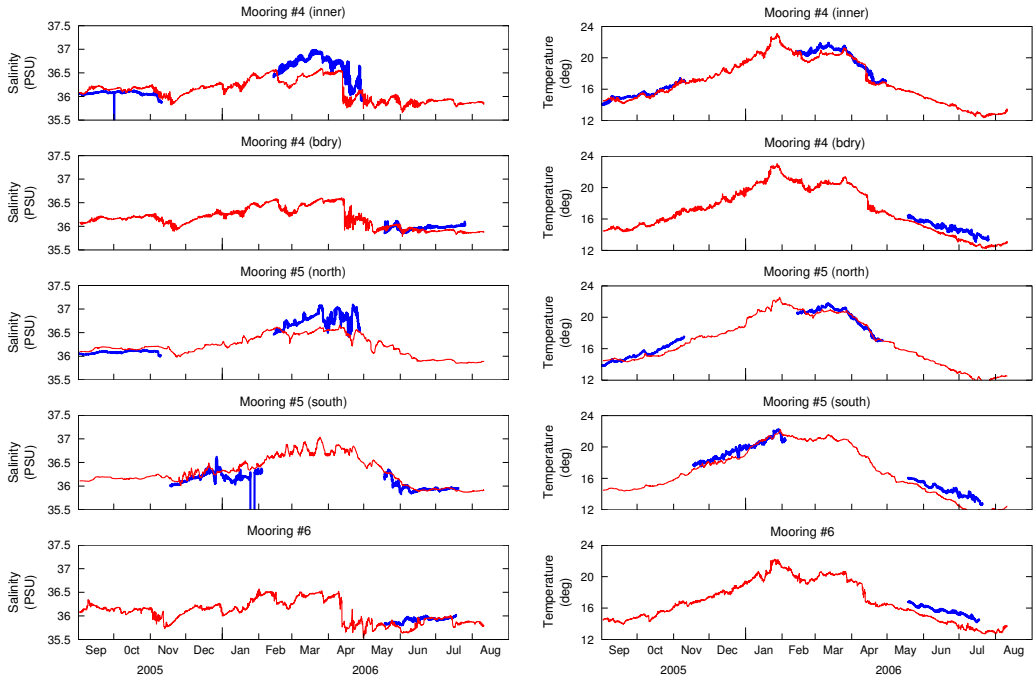

Figure 7.3.3. Regional model temperature and salinity comparison using mooring derived sea level on the open boundary. Red = modelled, blue = measured.

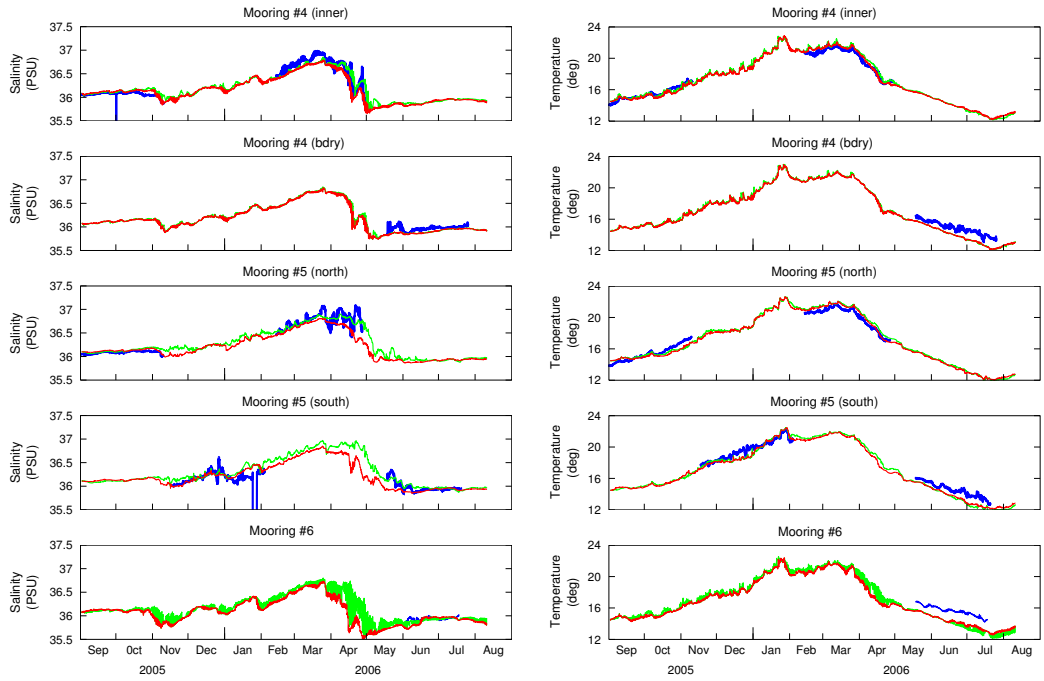

Figure 7.3.4. Local model temperature and salinity using different open boundary forcing. Green = eta forced, red = velocity forced, blue = measured.

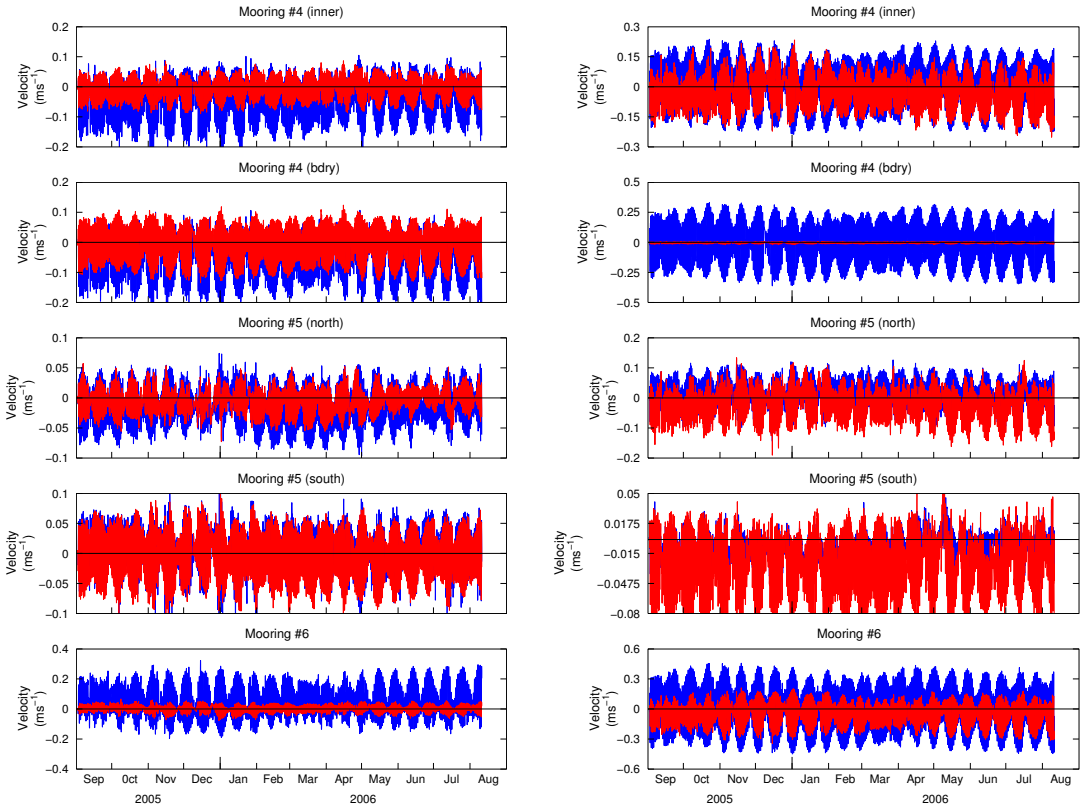

(a) East component

(b) North component

Figure 7.3.5. 2D velocity comparison using different open boundary forcing. Red = eta forced, blue = velocity forced.

8. Solutions

8.1. General Solutions

Flow in the TFZ region is dominated by the barotropic tide, with tidal currents approaching 0.3 m s^{-1} during spring tides (Figure 8.1.1). Currents are approximately half this value during the neap phase of the tide (Figure 8.1.2), and may be absent altogether during the dodge tide (see below). Flow is generally into the TFZ during the flood tide, and out on the ebb, with strongest currents near Cape Donnington on the ebb.

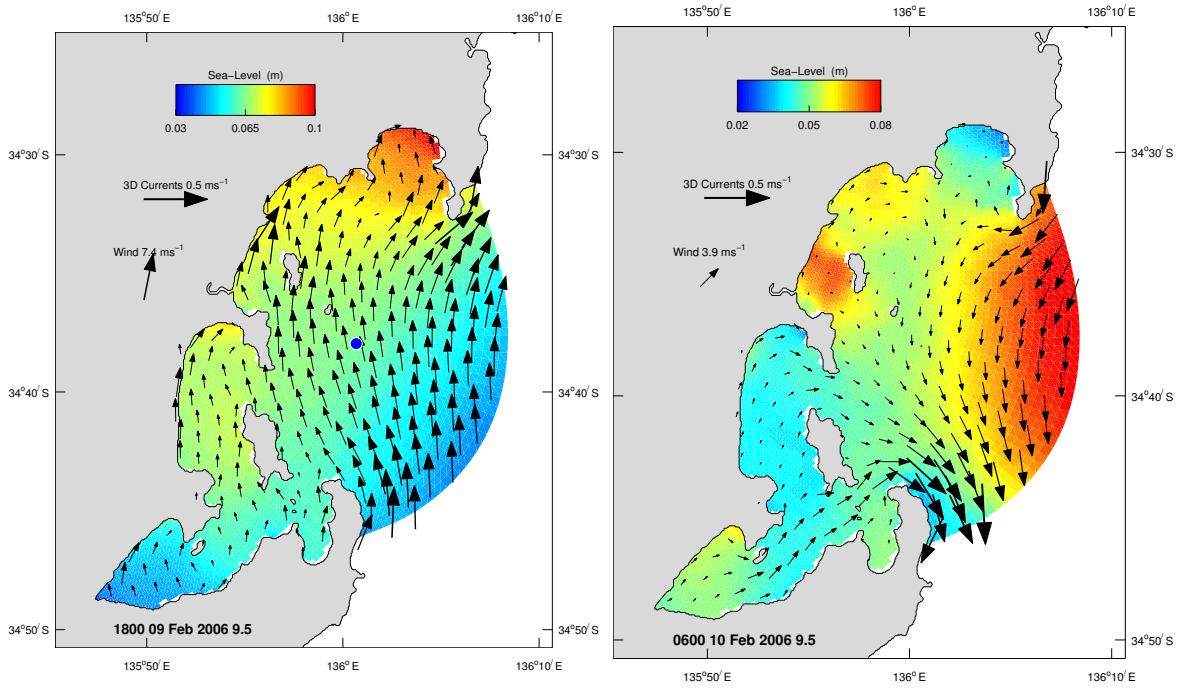

(a) Flood Tide (b) Ebb tide

Figure 8.1.1. Surface currents and sea level in the TFZ on flood and ebb spring tides.

The tidal flows can be modified by the influence of wind, and under strong winds the effects of wind forcing may dominate the tidal flow, particularly during neap tides when wind forcing may reverse the flow due to tides (Figure 8.1.3). During these periods of strong offshore flow the surface layer is driven offshore also, with a compensatory onshore flow at depth (Figure 8.1.4). This onshore flow is capable of transporting sub-surface features toward the coast by several kilometres; e.g. the offshore edge of the warm temperature anomaly in Figure 8.1.4. A similar “2-layer” flow was identified for summer in the transect and velocity data.

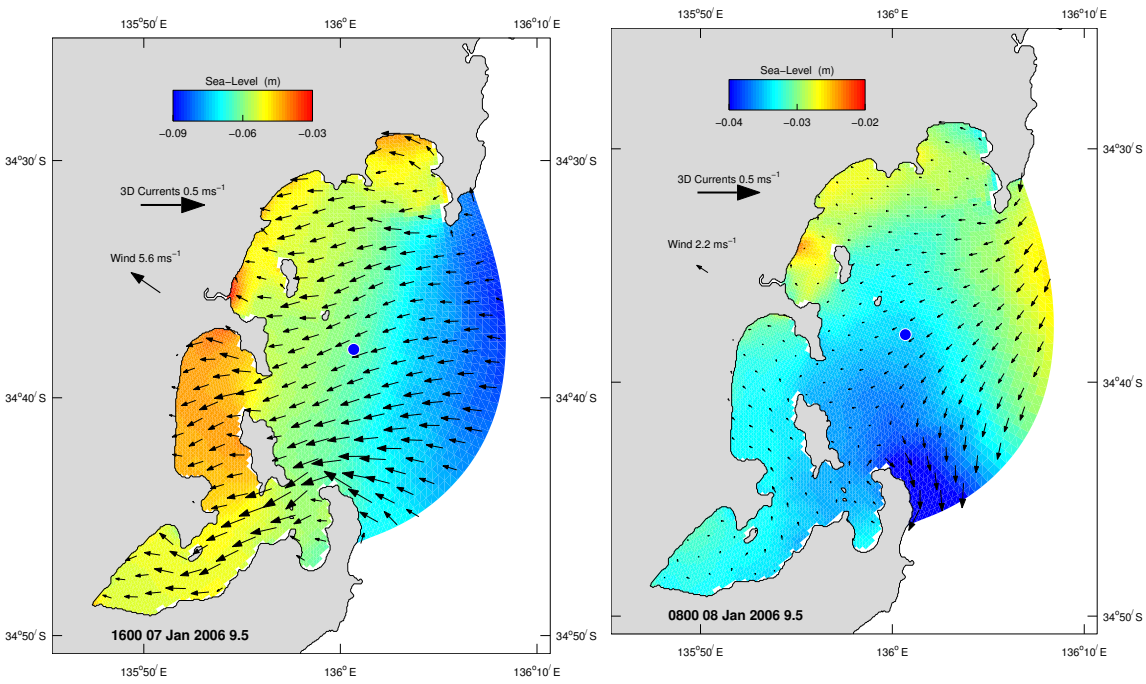

Figure 8.1.2. Surface currents and sea level on flood and ebb neap tides.

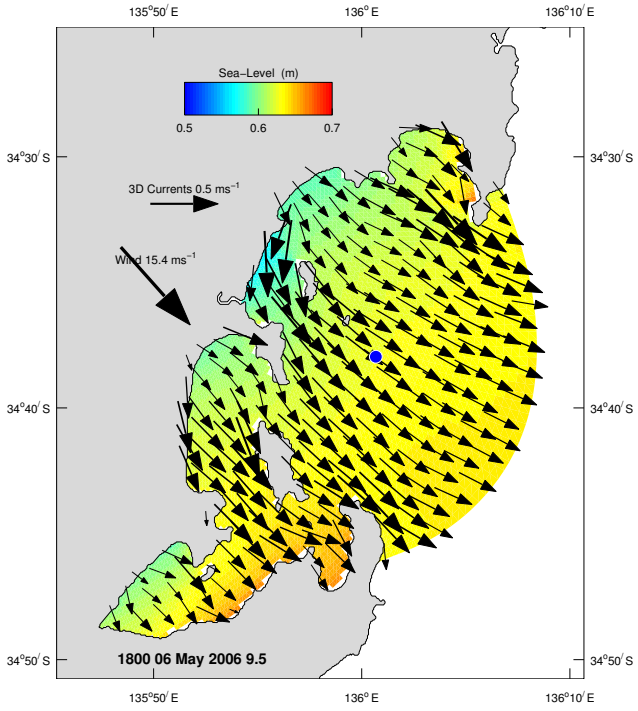

Figure 8.1.3. Surface currents and sea level during a neap flood tide and strong winds.

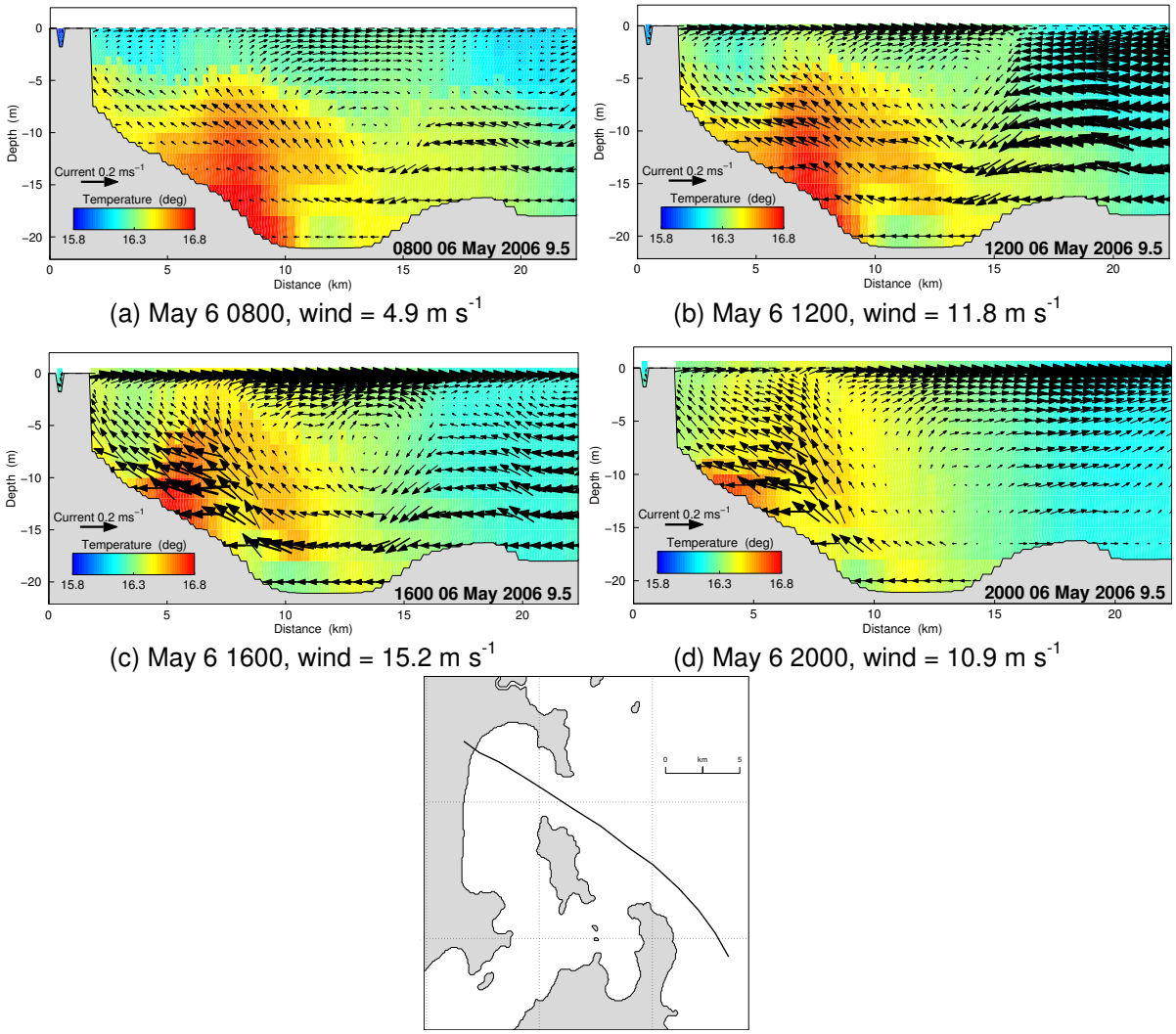

Figure 8.1.4. Section of temperature and currents during strong offshore wind.

The modelled surface elevation at a mid-domain location is displayed as a function of time in Figure 8.1.5. This shows that tidal ranges are approximately 1 m during spring tides and are generally confined to < 0.5 m during neaps. The neap – spring cycle has a period of ~14 days. The tide is mixed mainly semi-diurnal in character, which may be quantified by the form factor F = ratio of diurnal to semi-diurnal amplitudes ($F = (K_1+O_1)/(M_2+S_2)$). In the case of the TFZ F~0.88, verifying that the tide falls into the semi-diurnal mixed category ($0.25 < F < 1.5$). Interestingly, the major tidal constituents, M_2, S_2, K_1 and O_1 all have approximately the same amplitude of ~0.18 m (Table 8.1). This gives rise to the unique phenomenon of the dodge tide, which occurs at neap tides when the two major semi-diurnal components (M_2 & S_2) are 180° out of phase, in conjunction with the diurnal (K_1 & O_1) components opposed in phase, resulting in an approximate cancellation of all amplitudes and relatively stationary sea level accompanied by negligible tidal currents for an extended period. This can be observed on 8th Jan 2006, when a dodge tide exists during a period of low wind-speed (Figure 8.1.6). The corresponding sea level time series is displayed in Figure 8.1.7.

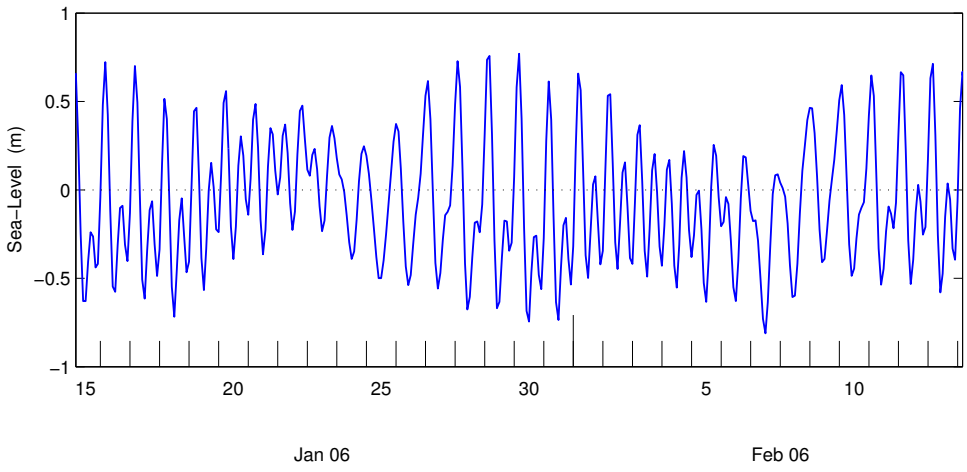

Figure 8.1.5. Time series of sea level in the middle of the TFZ over a neap-spring cycle

Table 8.1. Tidal characteristics of major constituents on the local grid open boundary.

Constituent	Amplitude (m)	Phase (°)
S2	0.176	125.96
M2	0.180	85.59
K1	0.187	237.89
O1	0.128	215.79

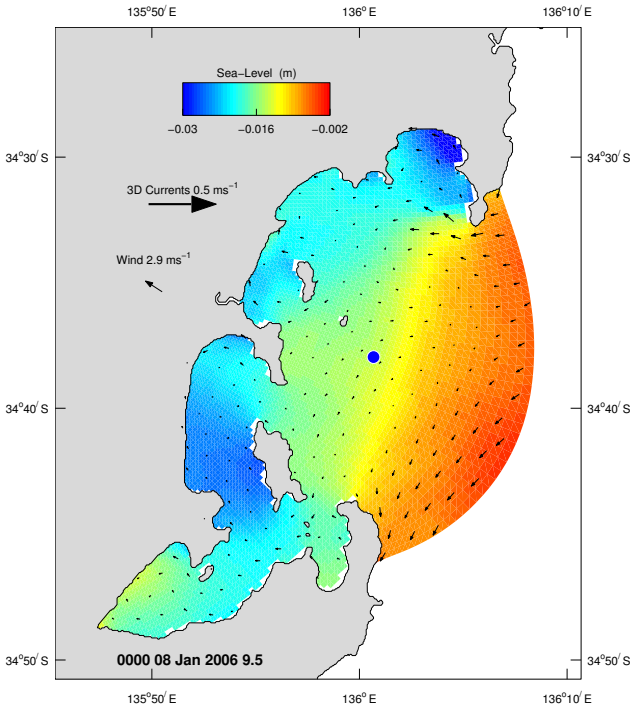

Figure 8.1.6. Sea level and currents during the dodge tide, 8th January 2006.

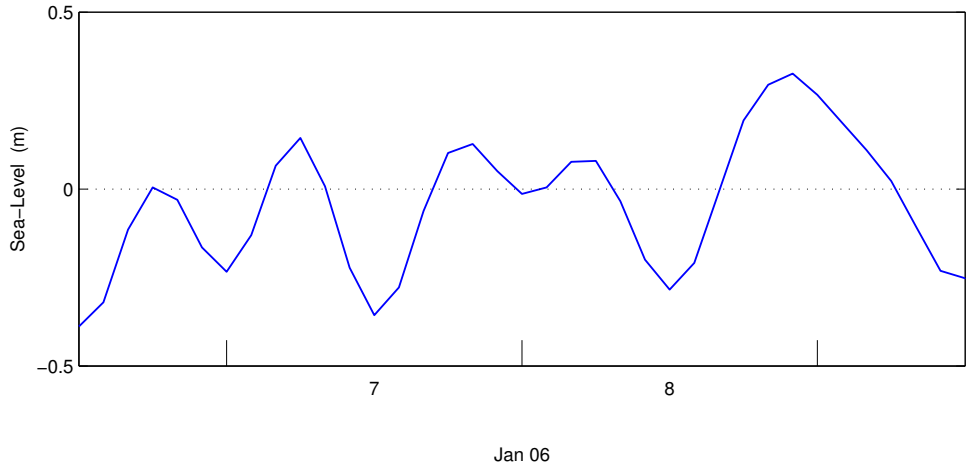

Figure 8.1.7. Time series of sea level in the middle of the TFZ during a dodge tide: 8th January 2006.

Depth averaged currents exhibit the inflow on the flood tide and outflow on the ebb observed in the surface current field (Figure 8.1.8; compare with Figure 8.1.1), reflecting the tidal dominance of the flow. Profiles of current speed show a sheared current profile during summer and a uniform profile during winter (Figure 8.1.9), indicative of a stratified and well mixed water column in summer and winter respectively. In summer, currents are maximum at the surface on the flood spring tide, and very little flow is observed during the neap tide. A subsurface maximum is also observed at the location of the profile on the flood tide (e.g. 1 January 1400, wind: south-easterly ~7 m s^{-1}), and during spring ebbs the current becomes more well mixed (12 January 2200, wind: southerly ~10 m s^{-1}). These phenomena appear to be more prevalent when the tide assumes a more mixed semi-diurnal character and currents are stronger, and when stronger winds combine with the flood and oppose the ebb.

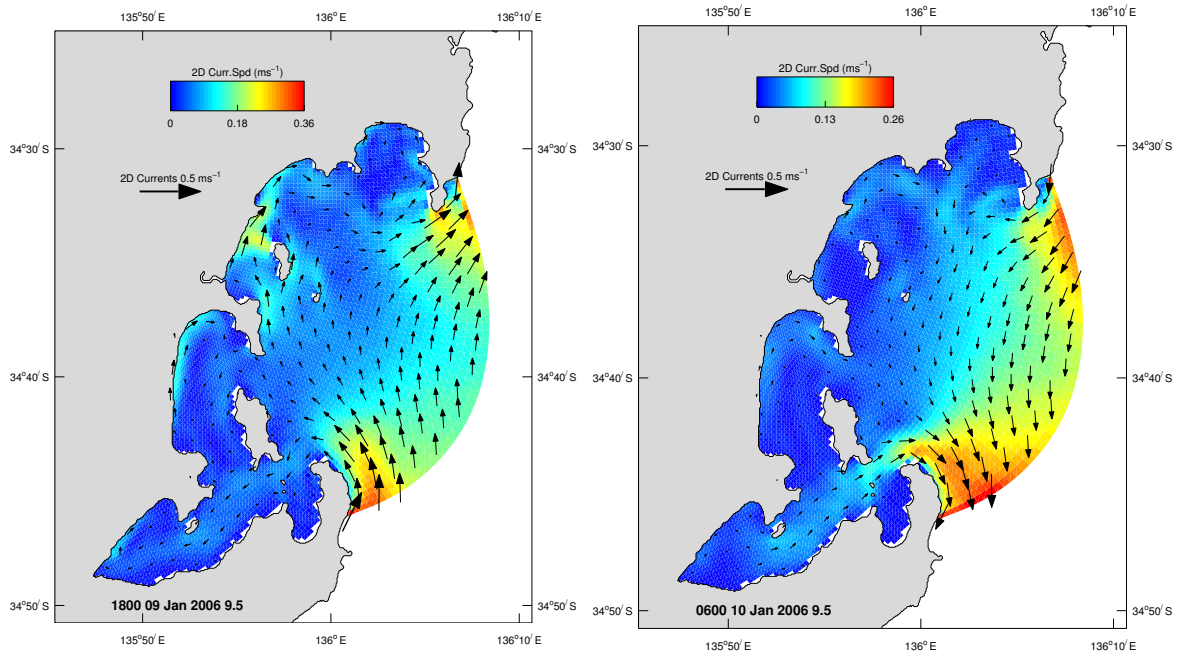

(a) Flood Tide (b) Ebb tide

Figure 8.1.8. Depth averaged currents and sea level on flood and ebb neap tides.

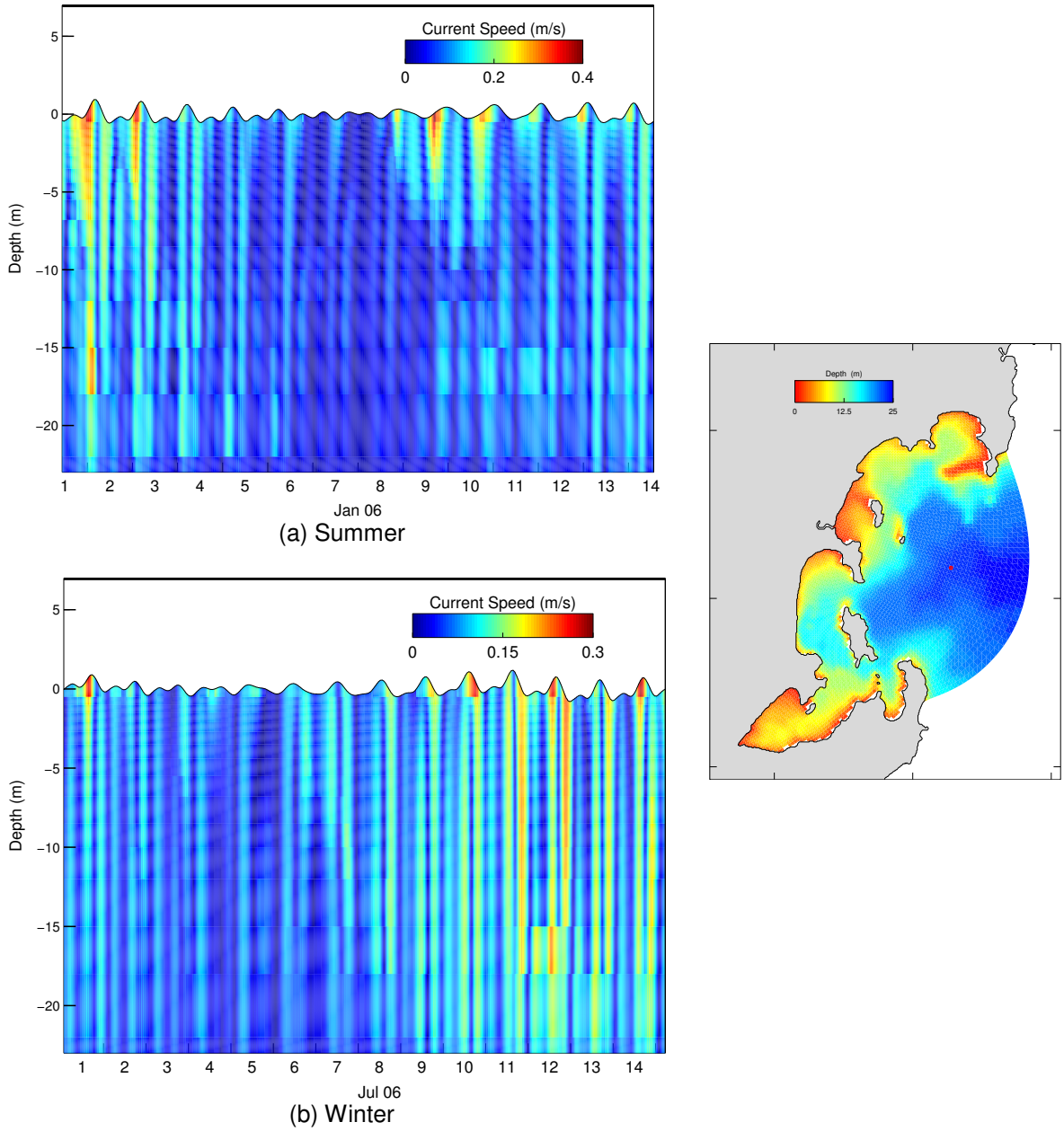

Figure 8.1.9. Time profile of current speed at a mid-TFZ location (red dot in image at right) demonstrating vertical distribution of flow.

Consistent with the velocity profiles, density distributions reveal the TFZ to be stratified during summer (Figure 8.1.10) and well mixed during winter (Figure 8.1.11). However, in summer periods of uniform properties exist through the water column and the variability in the depth of the mixed layer is large; instances of stratification typically occur during periods of light winds and large net heat input into the surface, and strong winds in conjunction with strong tidal mixing can destroy this stratification on a time-scale of days. Lighter water is found in the shallow coastal regions and Proper Bay as a result of differential heating (Figure 8.1.12). In the winter this trend is reversed. Convective cooling in conjunction with tidal mixing maintains the well mixed nature during winter. Note that Figure 8.1.11 is taken at midnight when solar input is zero and a negative heat flux contributes towards cooling at the sea surface. This results in the inverted density profile near the surface observed in Figure

8.1.11 (b), which subsequently leads to convective mixing. The annual temperature cycle in the TFZ is partly controlled by the surface heat flux, whereas advective processes play a more dominant role in determining the salinity distribution, with large decreases in salinity in autumn (Figure 8.1.13) when the flushing of Spencer Gulf occurs and fresher compensatory oceanic flows enter western Spencer Gulf, and impact on the TFZ. Local salinity increases exist due to evaporation near the coast and in Proper Bay; the latter local salinity increase is persistent throughout the year (Figure 8.1.14). The dense coastal underflow that was observed in the data (Fig 6.3.7-6.3.8) is captured by the model for April (Figure 8.1.15). Cooler temperatures are observed in this underflow in winter; the density structure does not readily illustrate this underflow due to the compensatory effect of lower salinity during that time.

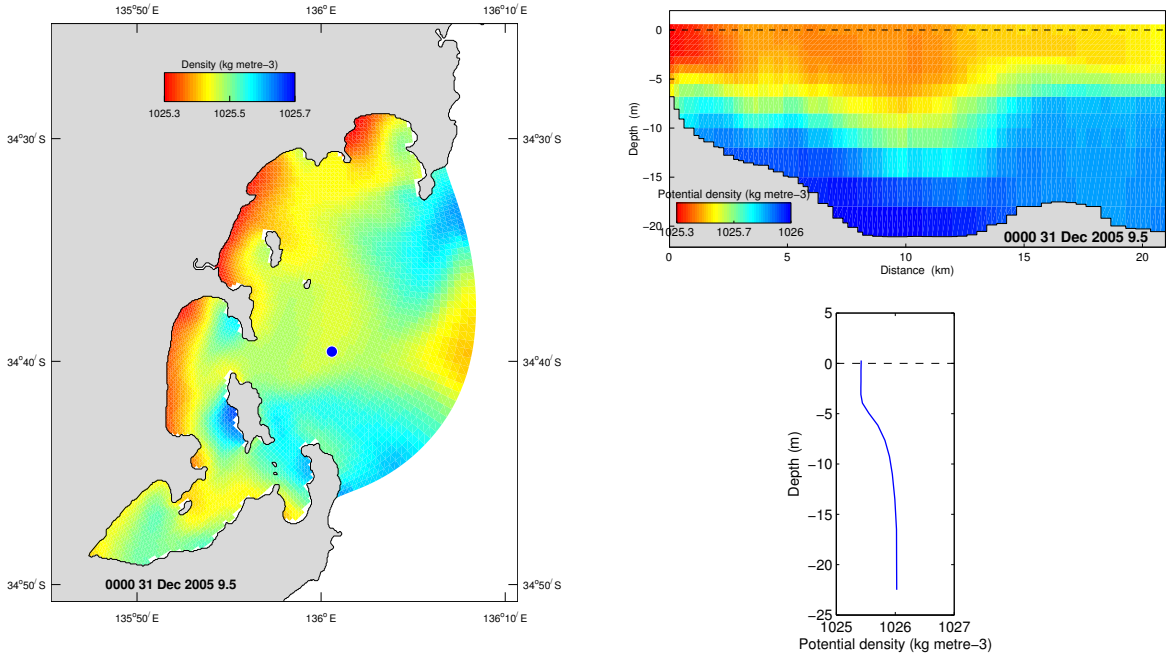

(a) Surface distribution (b) Profile & section

Figure 8.1.10. Summer surface potential density, with profile at the location of the blue dot.

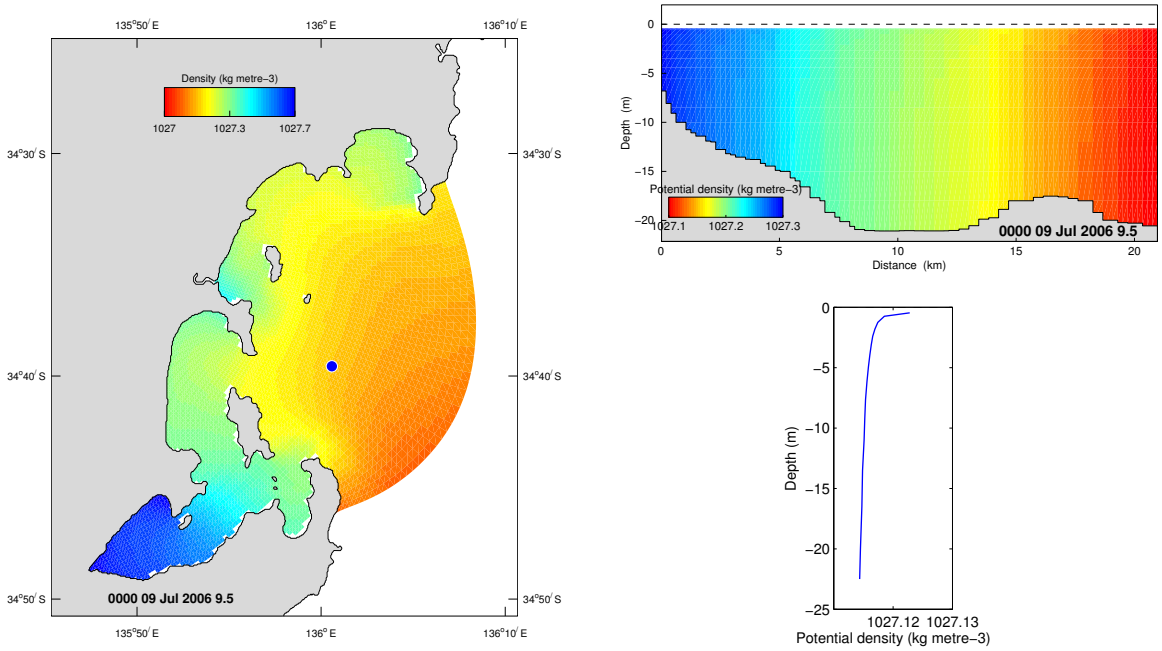

(a) Surface distribution (b) Profile & section

Figure 8.1.11. Winter surface potential density, with profile at the location of the blue dot.

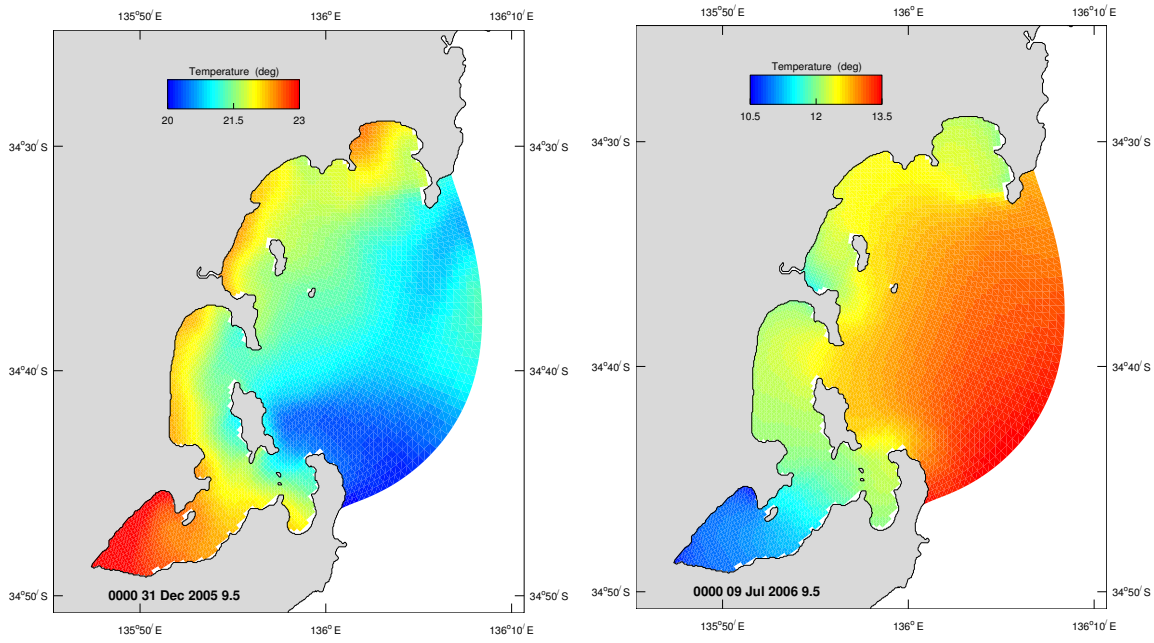

(a) Summer (b) Winter

Figure 8.1.12. Surface temperature.

Figure 8.1.13. Time series of surface salinity mid-TFZ.

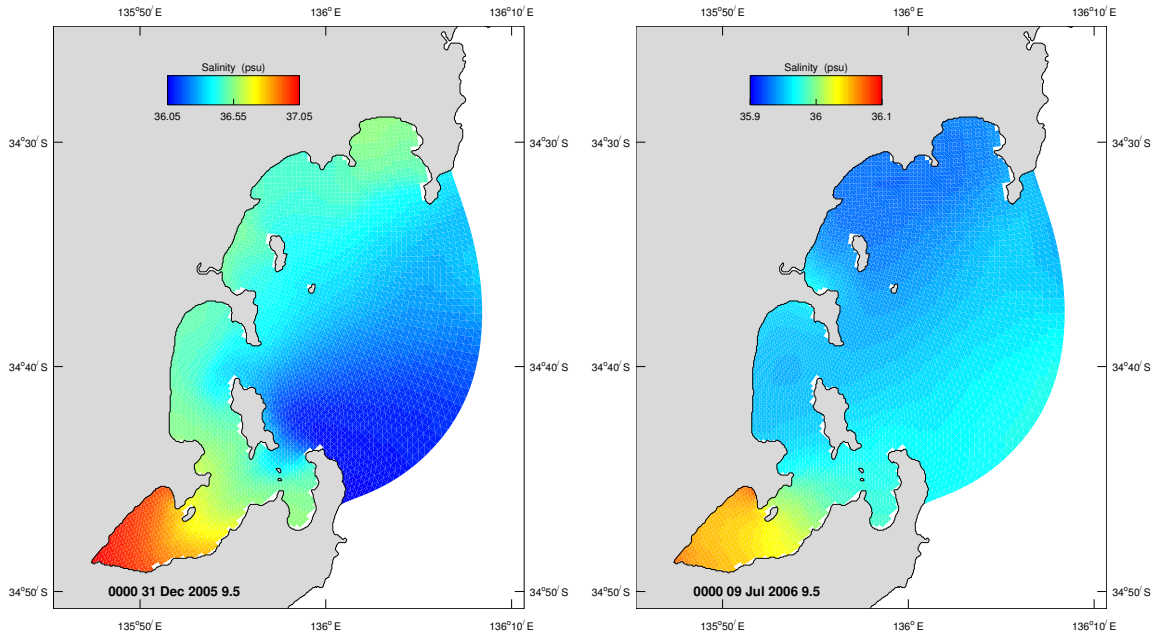

(a) Summer (b) Winter

Figure 8.1.14. Surface salinity.

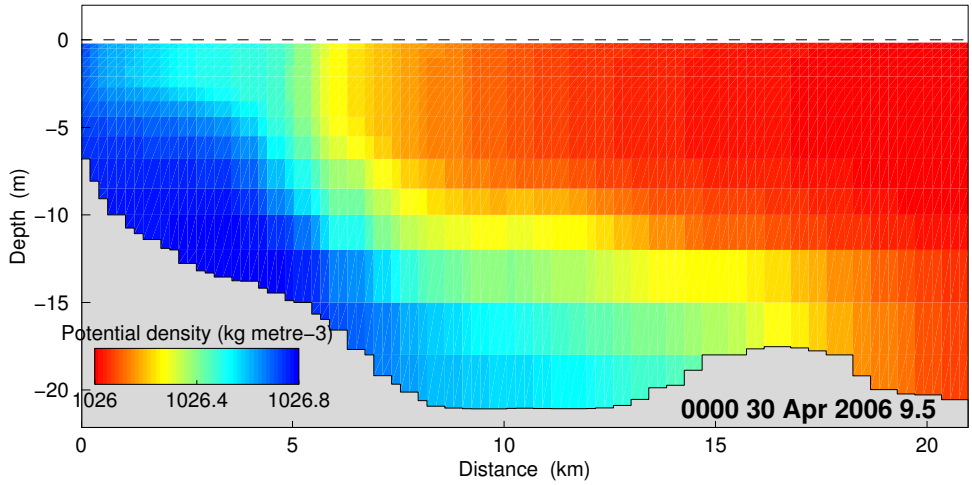

Figure 8.1.15. Salinity section in April demonstrating the dense coastal underflow.

8.2. Residual (Net) Currents

The long term net flow in the domain was obtained by calculating a Eulerian average of the model velocity components at every time-step over 90 day (i.e. seasonal) periods. It is the net flow that is important from a flushing perspective, since transport by this flow provides a mechanism that may potentially remove material permanently from the TFZ. These flow patterns reflect the distribution passive tracers are expected to follow in the long term. Seasonal depth averaged residual flows are displayed in Figures 8.2.1 – 8.2.4, surface residual flows in Figures 8.2.5 – 8.2.8, and bottom residual flow for summer and winter in Figures 8.2.9 and 8.2.10 respectively.

The depth averaged seasonal flow can be characterised into three main sub-regions within the domain. Firstly, offshore of Boston Island flow enters the domain in the south and exits in the north, with little penetration into the coastal margins. Secondly, the Boston Bay / Proper Bay area can be treated as a separate system, with flow generally entering north of Boston Island, flowing south to loop through Proper Bay and exiting to the east of Boston Island, where a persistent anti-clockwise gyre exists off Cape Donnington. Thirdly, Louth and Peake Bays exhibit northwards flow along the coast, fed by water seaward of Point Boston, and seasonally exhibiting gyres within Peake Bay and off Louth Island. This circulation is schematically illustrated in Figure 8.2.11.

Surface seasonal currents exhibit generally onshore flow during summer and autumn and offshore flow during winter and spring. Summer flows are strongest, with surface waters moving north in Boston and Louth Bays. In winter the surface flow in Boston Bay reverses to be southwards. These surface flows are generally compensated by bottom flow in the opposite direction, e.g. offshore in summer. Therefore, the winter situation (Figure 8.2.10) corresponds to an upwelling situation where the potential exists for deep water in the gulf to be advected into the TFZ region.

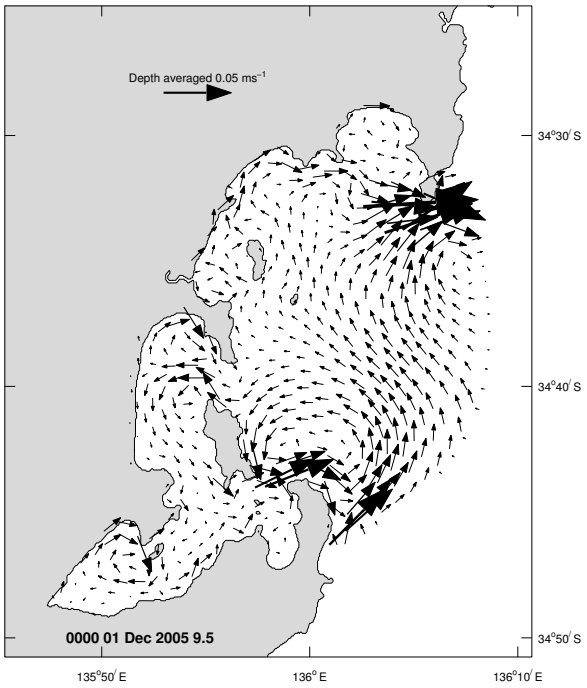

Figure 8.2.1. Spring depth averaged velocity.

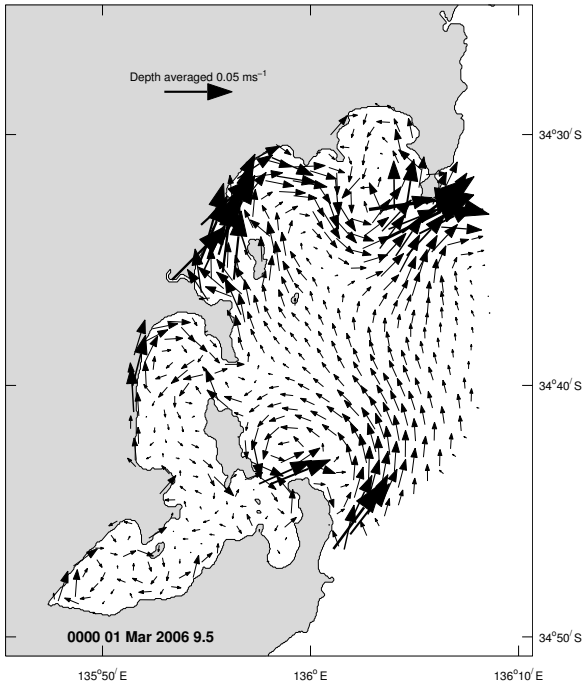

Figure 8.2.2. Summer depth averaged velocity.

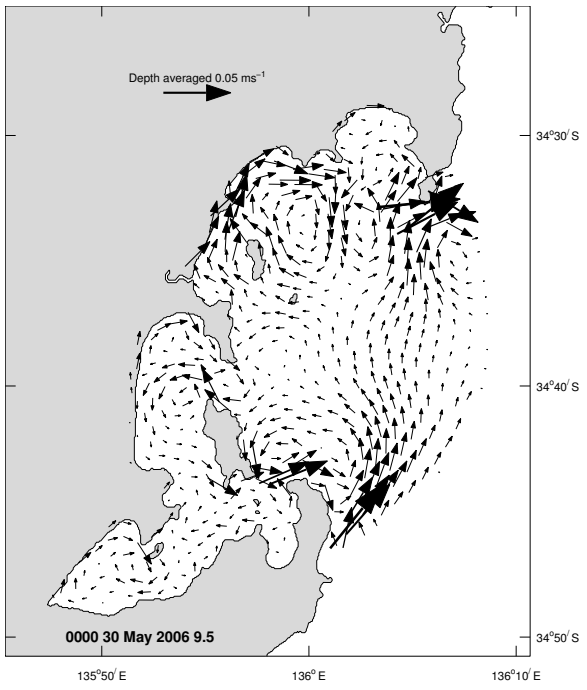

Figure 8.2.3. Autumn depth averaged velocity.

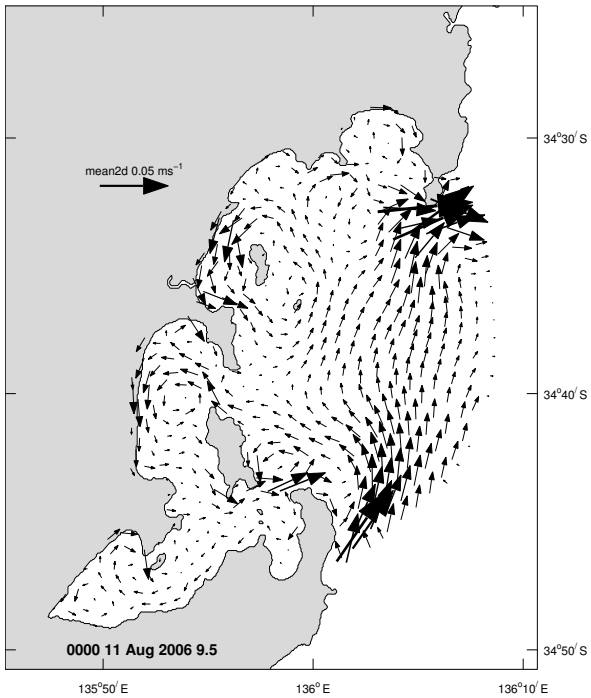

Figure 8.2.4. Winter depth averaged velocity.

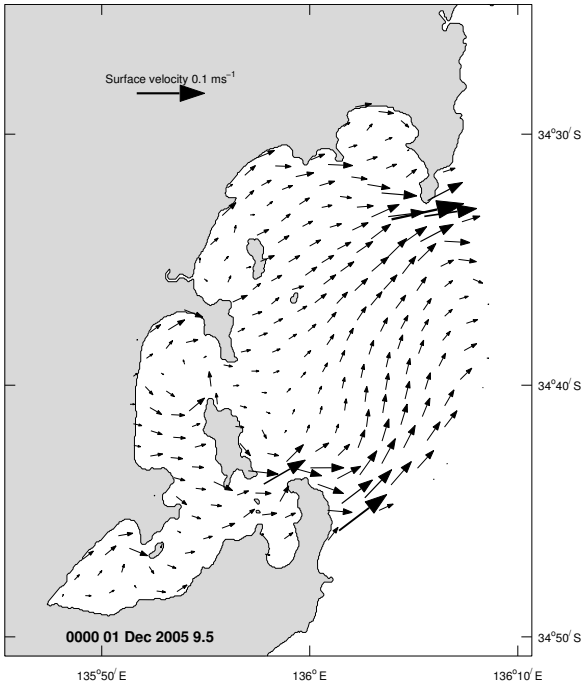

Figure 8.2.5. Spring surface velocity.

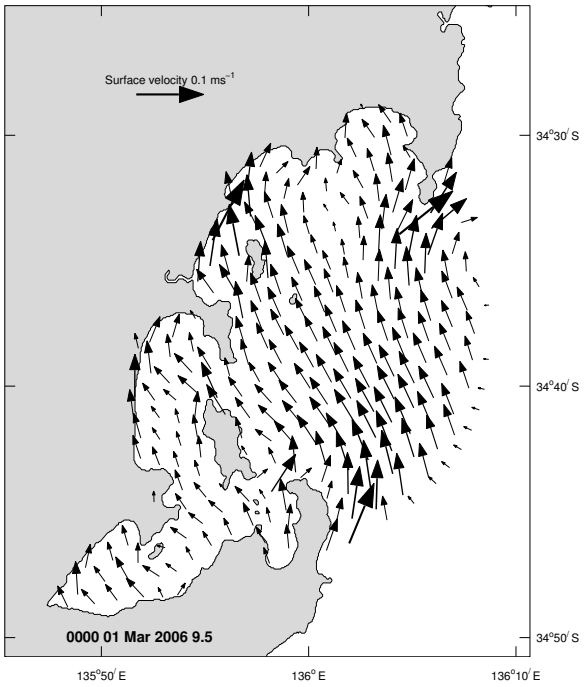

Figure 8.2.6. Summer surface velocity.

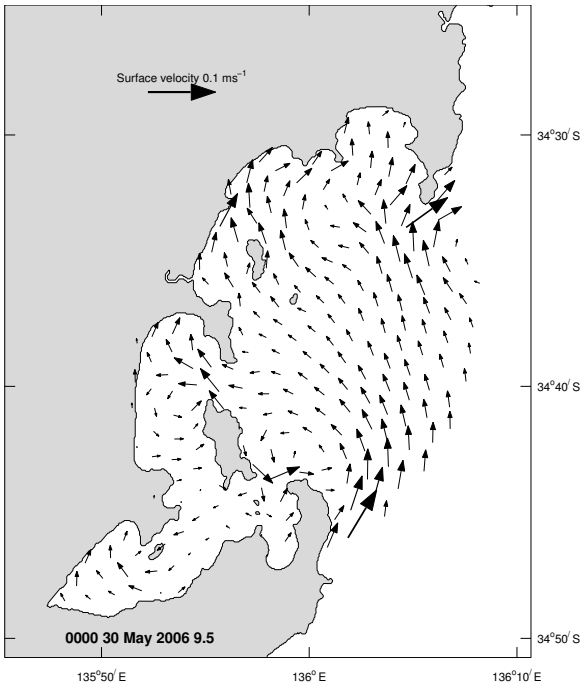

Figure 8.2.7. Autumn surface velocity.

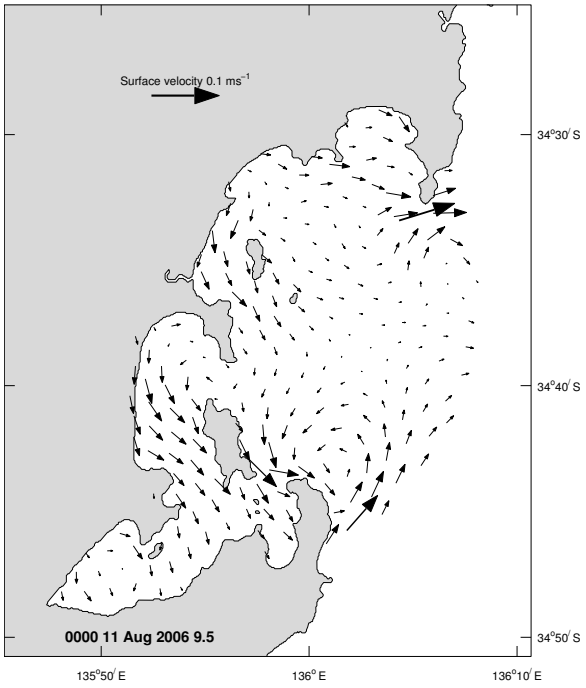

Figure 8.2.8. Winter surface velocity.

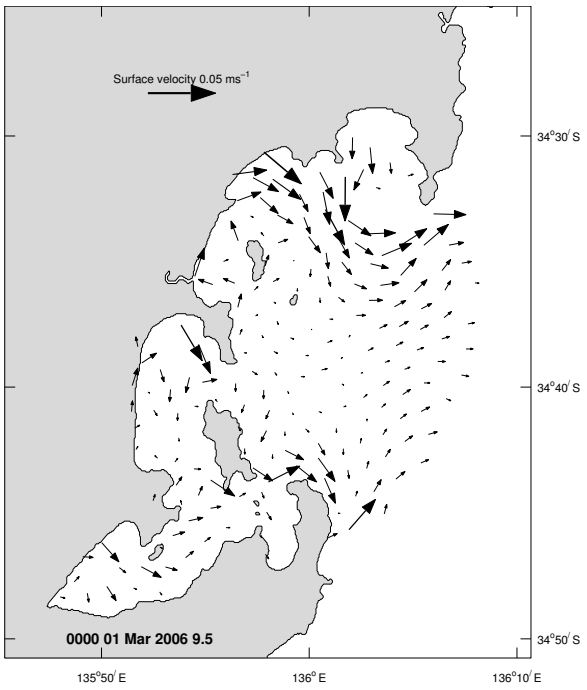

Figure 8.2.9. Summer bottom velocity.

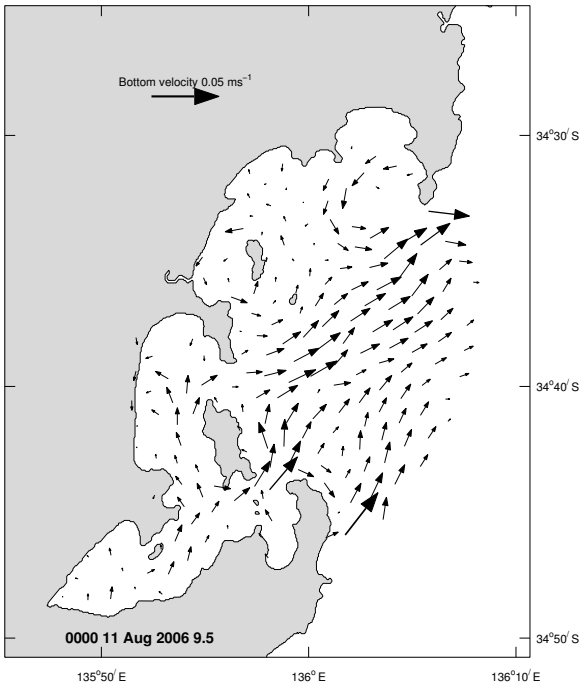

Figure 8.2.10. Winter bottom velocity.

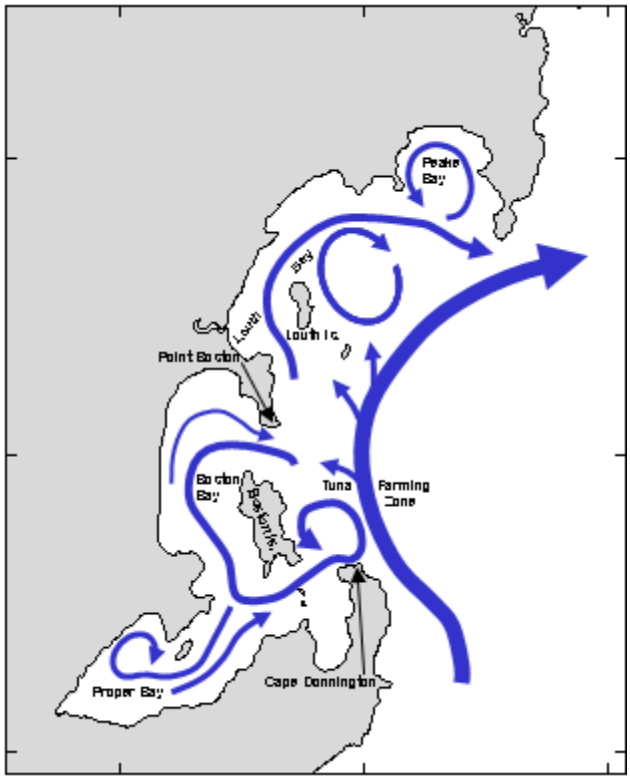

Figure 8.2.11. Schematic of depth averaged mean flow.

8.3. Summer Circulation and Upwelling

During summer (January to March), strong south-easterly winds over the shelf offshore from the mouth of the gulf create an upwelling favourable environment that results in cooler surface water residing off Eyre Peninsula and south-west Kangaroo Island (Middleton and Bye 2007). This upwelled water is hypothesized to have its origin in slope waters south of Kangaroo Island and may be a potential source of nutrients if advected into Spencer Gulf and the TFZ area. Strong upwelling favourable winds were observed during January and early February 2006 (Figure 6.3.2), with associated upwelling evident.

The model shows cooler bottom water residing at the open boundary, with a cooler pool adjacent to the west of Yorke Peninsula (Figure 8.3.1). Cool water is not observed to strongly intrude into the TFZ region (the local model domain), although a temperature drop is observed around January 28th in bottom waters off Cape Donnington (Figure 8.3.2). Diurnal variability is observed to be evident during this period, associated with diurnal heating and convective cooling due to the surface heat flux. This temperature drop was also observed in modelled and measured data at mooring site M5 (Figure 8.3.3). The February 11th CTD transect (Figure 6.3.5-6.3.6) also indicates the existence of an onshore subsurface plume of cold fresh water. No clear propagation of a cool plume was observed into the TFZ region, indicating advection of upwelled water probably did not play a dominant role in decreasing bottom temperature during this time. However, we note that the calculated synthetic temperature presented in Section 6.3 is too warm, indicating that atmospheric heating alone is insufficient to account for the lower observed temperatures. That is, advection of cool water into the region may also be important.

In order to assess the role of advection during the upwelling period, the regional model was simulated with a passive tracer initialized to zero and having an open boundary condition equivalent to that of temperature. Two experiments are considered. In the first, the model is initialized on September 1st 2005 and results are presented for January 1st 2006. During this period, the winds are strongly from the north-west (Figure 6.3.2) and for the shelf are downwelling favourable. For the gulf mouth, such winds will drive a cyclonic (clockwise) circulation at the lower part of the gulf and near the mouth (Section 6.4; Middleton and Teixeira 2008). The result of this circulation on the passive tracer is evident in Figure 8.3.4. Results show that there is a gradual inflow of water on the western side of the gulf from October onwards (Figure 8.3.4).

Now consider the results of a second experiment with the passive tracer initialised using the open boundary temperature on January 1st 2006. The results are presented for JD 5935 (end of March) when the upwelling favourable winds cease (Figure 6.3.2). The results at this time show (Figure 8.3.5) an anticlockwise circulation near the gulf mouth with upwelled water moving from the shelf, east gulf coast and past the TFZ region.

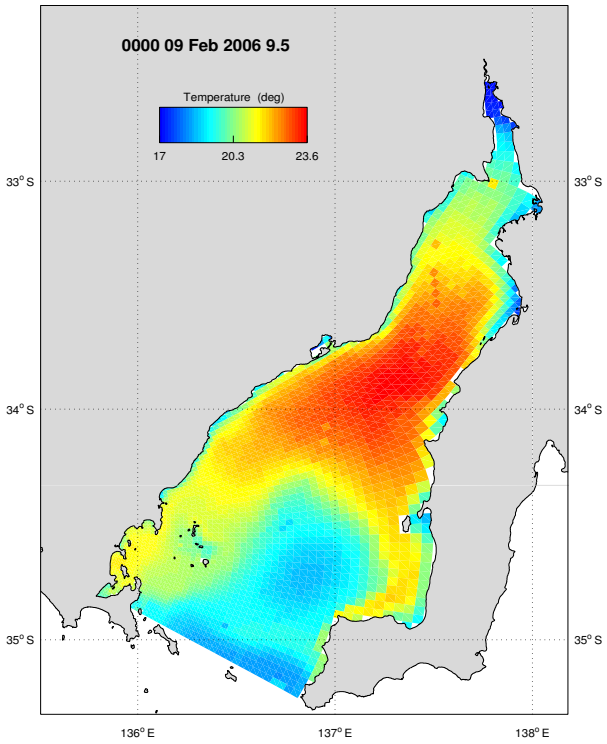

Figure 8.3.1. Regional modelled bottom temperature.

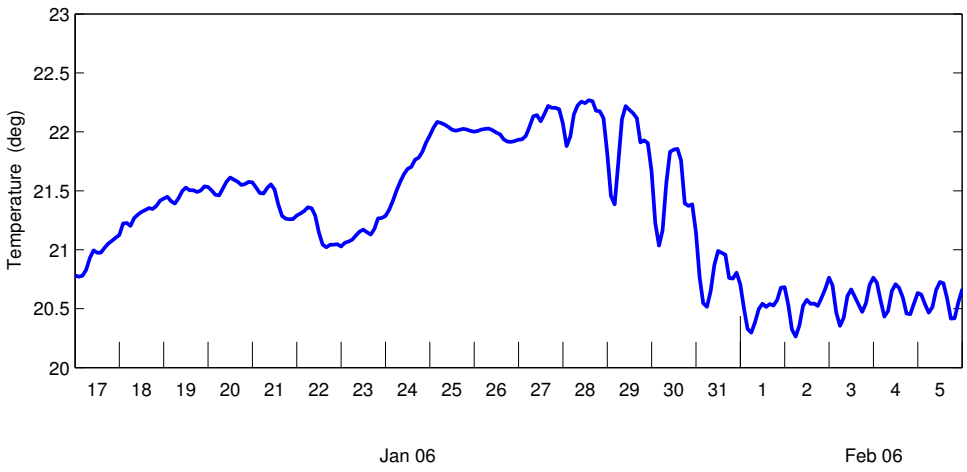

Figure 8.3.2. Modelled time series of bottom temperature off Cape Donnington.

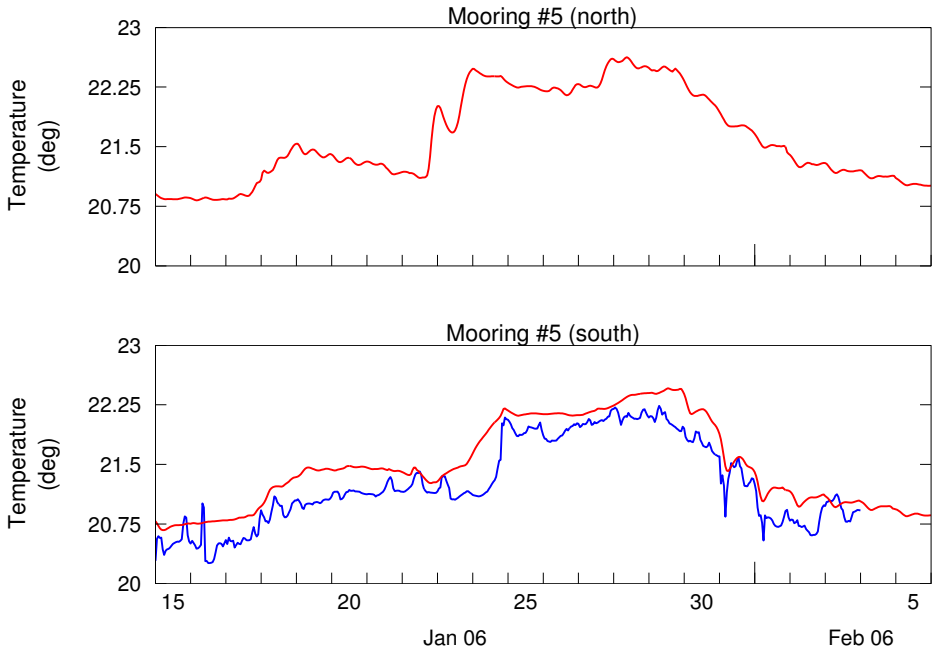

Figure 8.3.3. Measured (blue) and modelled (red) time series of temperature at Mooring #5.

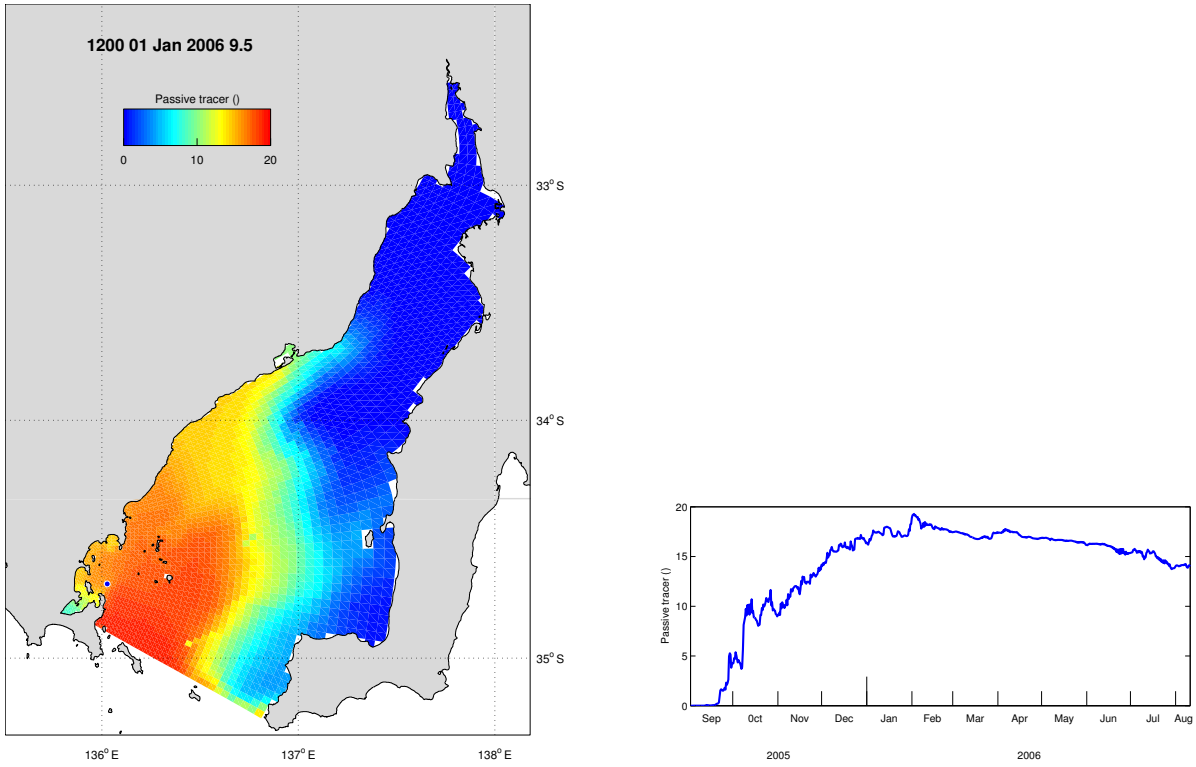

(a) Bottom temperature (b) Bottom time series in at Cape Donnington.

Figure 8.3.4. Passive tracer distribution using temperature open boundary condition to illustrate advective effects.

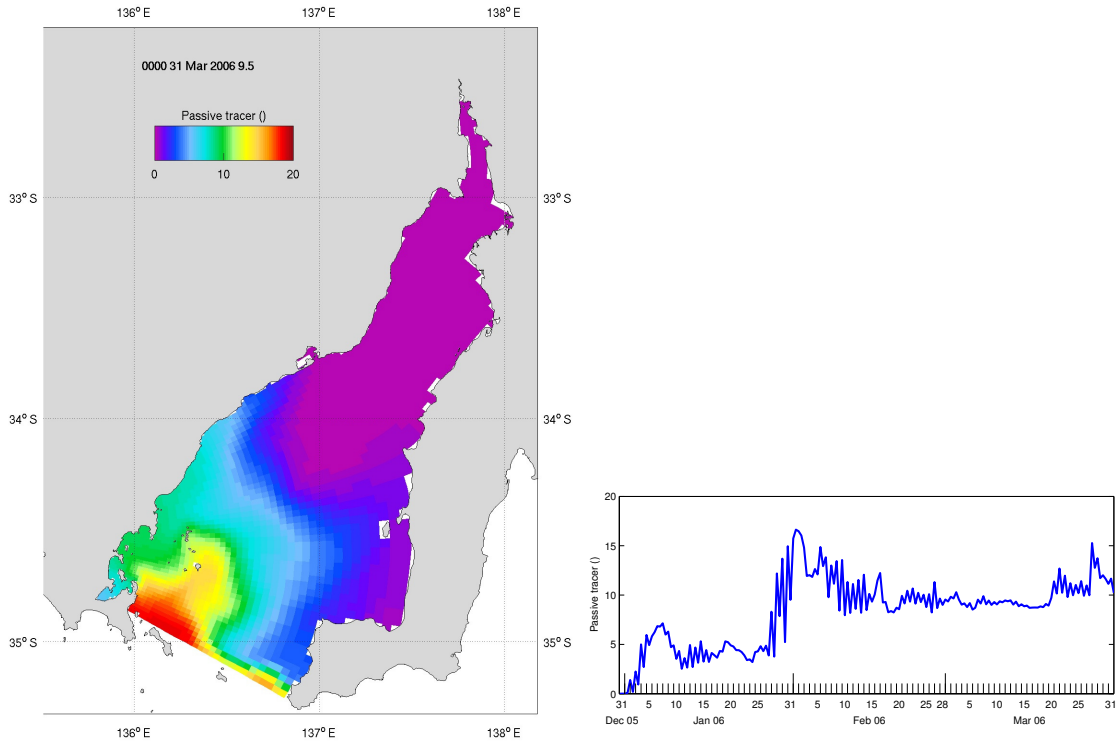

(a) Bottom temperature

(b) Bottom time series in at Cape Donnington.

Figure 8.3.5. Passive tracer distribution initialised in January 2005, using temperature open boundary conditions to illustrate advective effects.

8.4. Flushing Characteristics

Passive tracers were used to obtain an estimate of the flushing characteristics of various regions around the TFZ. A passive tracer was initialised in a sub-region with a concentration of 1 and zero elsewhere, and the total mass in this sub-region was calculated throughout the simulation. Full forcing was applied to the domain (i.e. wind, tide, low frequency sea level and temperature / salinity effects). The e-folding time for flushing this sub-region is encountered when the total mass was reduced to 1/e (~38%) of the initial mass. This representation of the flushing time assumes that tracer is well mixed in the sub-region and the total mass is assumed to decrease exponentially according to:

$$M(t) = M_0 e^{-t/\tau} \qquad 8.4.1$$

where M_0 is the initial mass and τ is the flushing time scale (Tartinville et al, 1997). When $M = M_0/e$ then $t = \tau$, hence the flushing time can be recovered.

Summer (January 2006) flushing times for various sub-regions of the domain are displayed in Figures 8.4.1 to 8.4.6. These figures include the initial tracer distribution which defines the sub-region, the tracer distribution at the flushing time, and the temporal evolution of normalized total mass in the sub-region. The flushing times are tabulated in Table 8.4.1; included in this table are the flushing times for the various sub-regions during winter (July 2006). The general trend of tracer decrease is obtained by fitting a 2nd or 3rd order polynomial to the total mass, which aids in identifying the time τ when total mass is reduced to 1/e. The exponential curve of equation 8.4.1 is also fitted to the data, using the time scale τ identified from the polynomial fit.

Table 8.4.1 indicates that there exists a wide range of flushing times depending on which region is flushed. The computed flushing estimates are a somewhat subjective measure of exchange, since there are various methods of computing flushing (e.g. Tartinville et al, 1997) which may potentially yield different results, and the assumptions made in deriving flushing times are often violated. The final tracer concentration distributions clearly show that tracer is not always well mixed throughout the flushing region, hence flushing estimates may be compromised. The forcing in effect also has a large impact on the flushing rate; computations for a different time period under the influence of differing wind, heatflux and tidal conditions are expected to produce different flushing times. During the computation of these flushing times winds were relatively strong (5 – 10 m s^{-1}) southerly to south-easterly during the end of the neap tide (minimum neap tide on 8th January) with maximum spring tides around 16th January. Therefore the flushing times presented in Table 8.4.1 should be treated with caution, and should not be assumed to be a definitive measure. They are, however, a useful indication of the relative flushing rates of various regions within the domain.

Proper Bay appears to have poor connectivity with the remainder of the domain and consequently has relatively slow flushing. Boston Island diminishes the connectivity of the bay westwards of the island with open water to the east, resulting in longer flushing times than Louth and Peake Bays. The zone encompassing the tuna farming region is also flushed relatively quickly, however, the tracer in this region has not exited the domain completely but rather has been re-distributed to other areas within the domain. This highlights one of the limitations of the application of these flushing estimates; the region in question may be

flushed, but the material flushed quite often is relocated to another area within the system and hence not completely removed. If tracer is distributed throughout the whole region then this is not possible, and reduction in total mass is only possible via transport through the open boundary resulting in the longest flushing estimate of ~14 days. This estimate is again dependent on the forcing in effect; using particle tracking provides a more accurate estimate of ~20 days for flushing the entire region (Section 8.6).

The winds imposed during the flushing calculations drove an onshore surface flow that was compensated with an offshore bottom flow, representing a downwelling situation. This was particularly evident in Louth Bay (Figure 8.4.7 a) and is reflected in the tracer distribution in Louth Bay, where tracer is rapidly subducted to lower levels in the water column and rapidly disappears from the surface layer (Figure 8.4.7 b).

Table 8.4.1. Flushing times.

Region	Flushing time (days)
Whole domain	13.9
Boston Bay	8.2
Proper Bay	10.8
Louth Bay	1.5
Peake Bay	2.7
Tuna zone	2.0

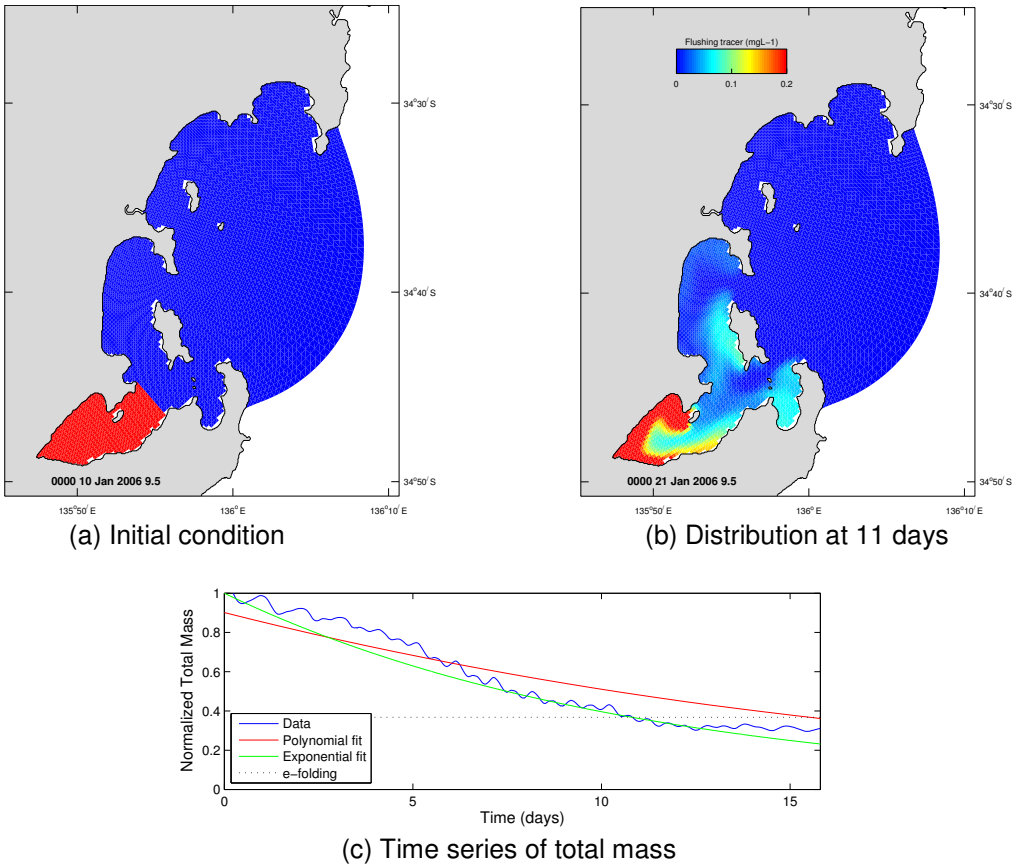

Figure 8.4.1. Flushing for Proper Bay.

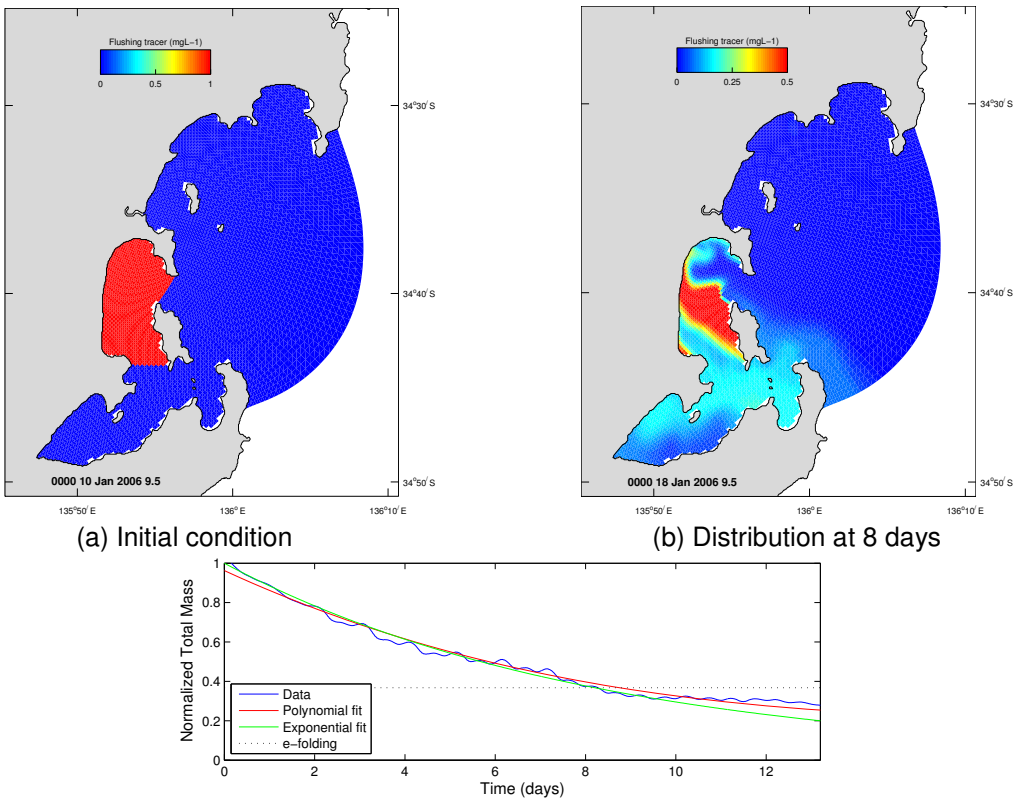

Figure 8.4.2. Flushing for Boston Bay.

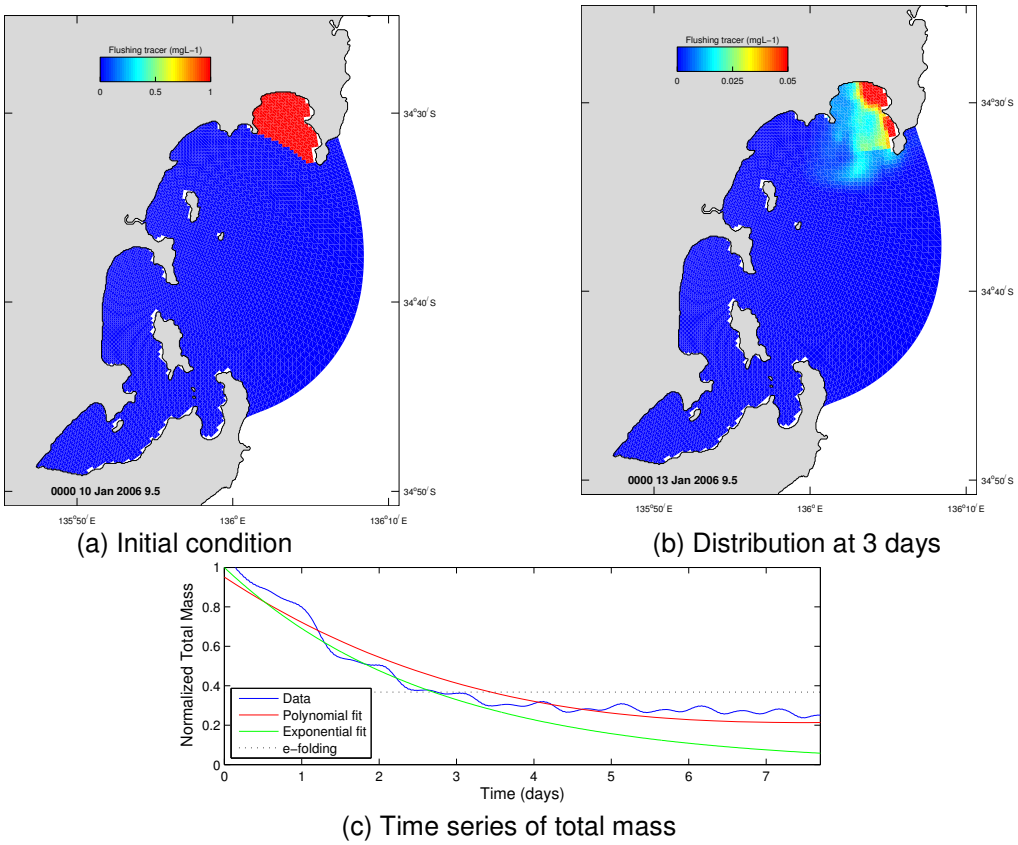

Figure 8.4.3. Flushing for Peake Bay.

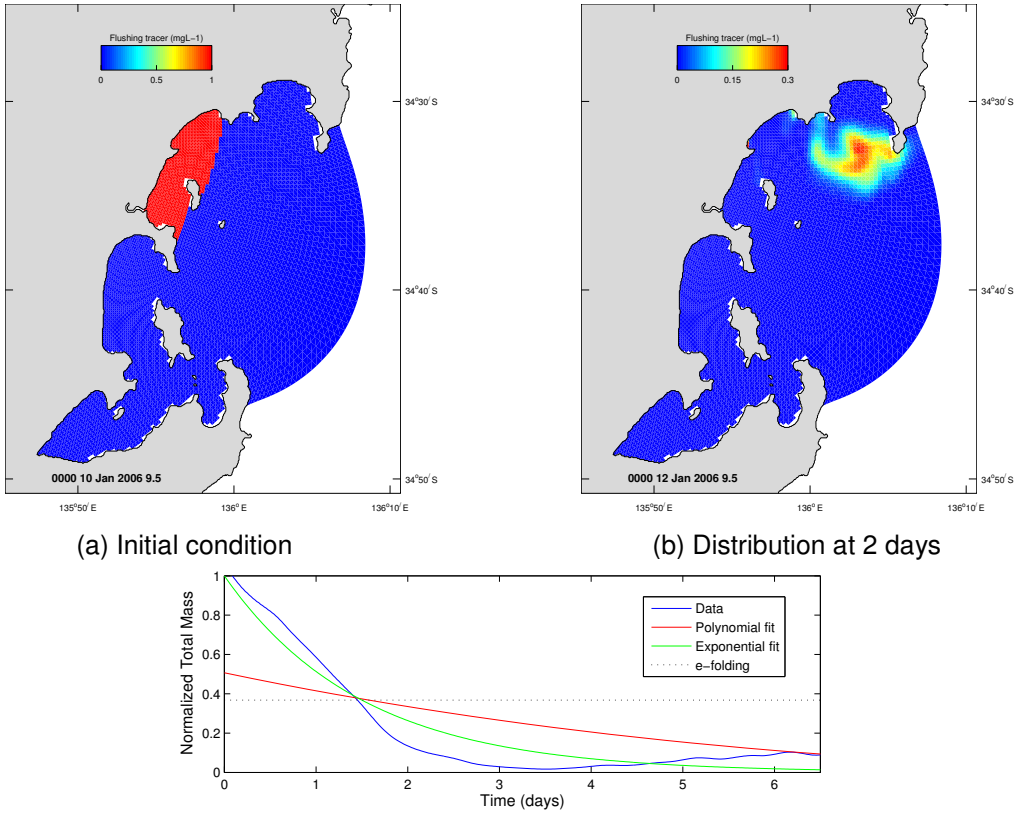

(a) Initial condition (b) Distribution at 2 days

(c) Time series of total mass

Figure 8.4.4. Flushing for Louth Bay.

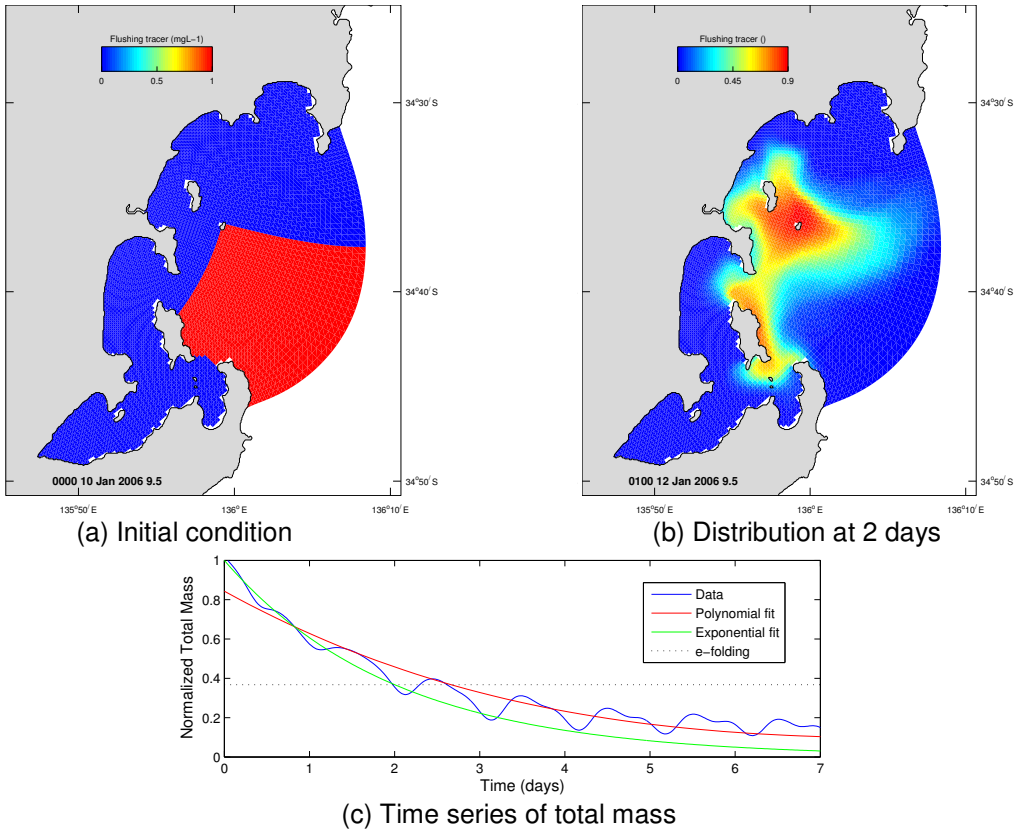

(a) Initial condition (b) Distribution at 2 days

(c) Time series of total mass

Figure 8.4.5. Flushing for the TFZ region.

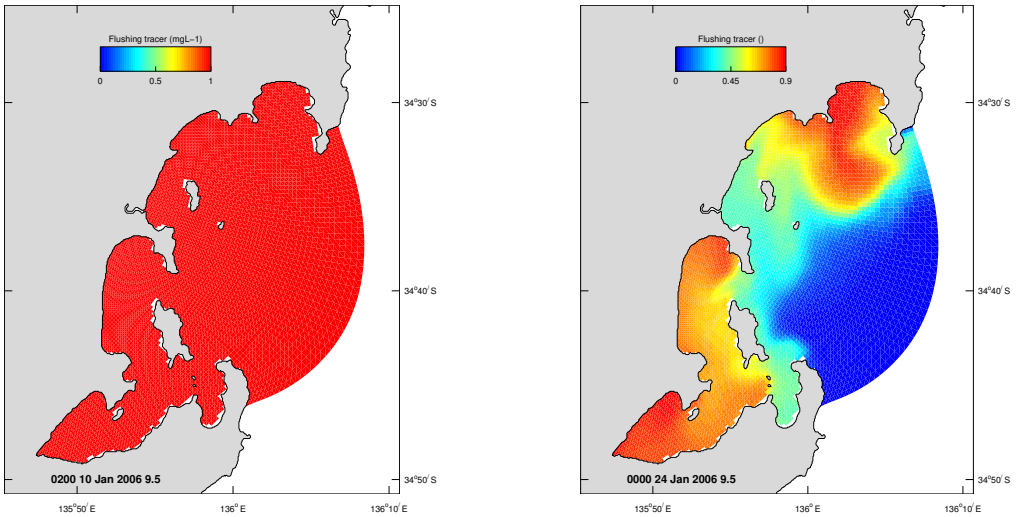

(a) Initial condition

(b) Distribution at 14 days

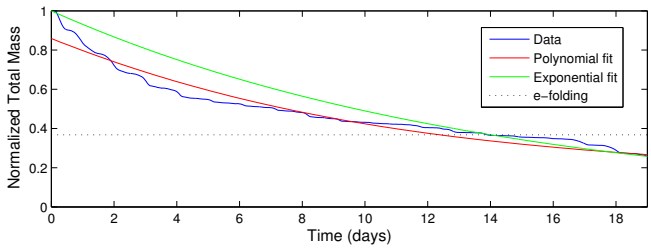

(c) Time series of total mass

Figure 8.4.6. Flushing for whole domain.

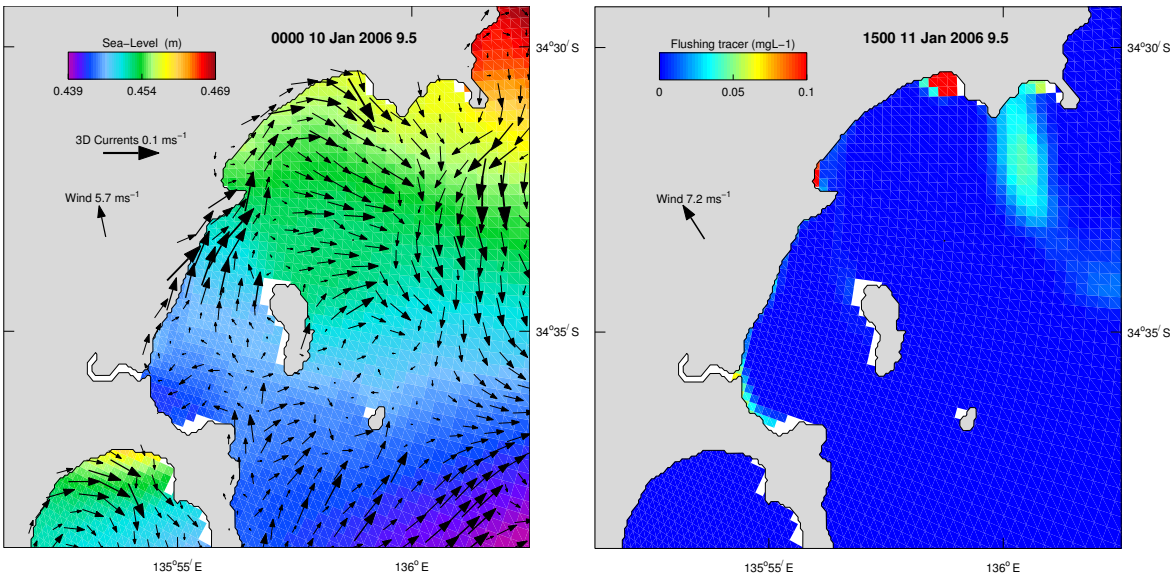

(a) Bottom flow

(b) Surface tracer distribution after 1.25 days

Figure 8.4.7. Flow characteristics demonstrating downwelling in Louth Bay.

8.5. Mixing zones

Point sources of tracers were continuously input into the water column at locations corresponding to a number of sites (Figure 8.5.1) with unit loads (assumed to be 1 g s^{-1} ~ 31,500 kg $year^{-1}$, giving output concentrations in units of gm^{-3}, or mgL^{-1}) for the 12 month simulation period of September 2005 - August 2006. Tracers were released into the top 1 m of the water column. The continuous tracer input will be advected and mixed to result in a quasi steady distribution, which will vary according to the forcing (wind, tide) in effect at any point in time. These distributions at any given time are not particularly useful to characterise the general tracer distribution, hence a statistical tracer distribution representing the whole simulation period was generated. Surface tracer distributions were output at 4 hour intervals and post-processed to compute the 5^{th}, 50^{th} (median) and 95^{th} percentile concentration distributions for the whole simulation, providing a statistical description of the distributions resulting from tracer transport over this period. Owing to the volume of information that must be stored to compute the statistical distributions, only distributions for the surface layer were attempted and it was not feasible to create plots for bottom waters or along sections. Note that the response of the tracers to the interaction of the point source input with the system dynamics is linear, so that if the load were scaled by some arbitrary factor then the corresponding concentrations can be scaled accordingly.

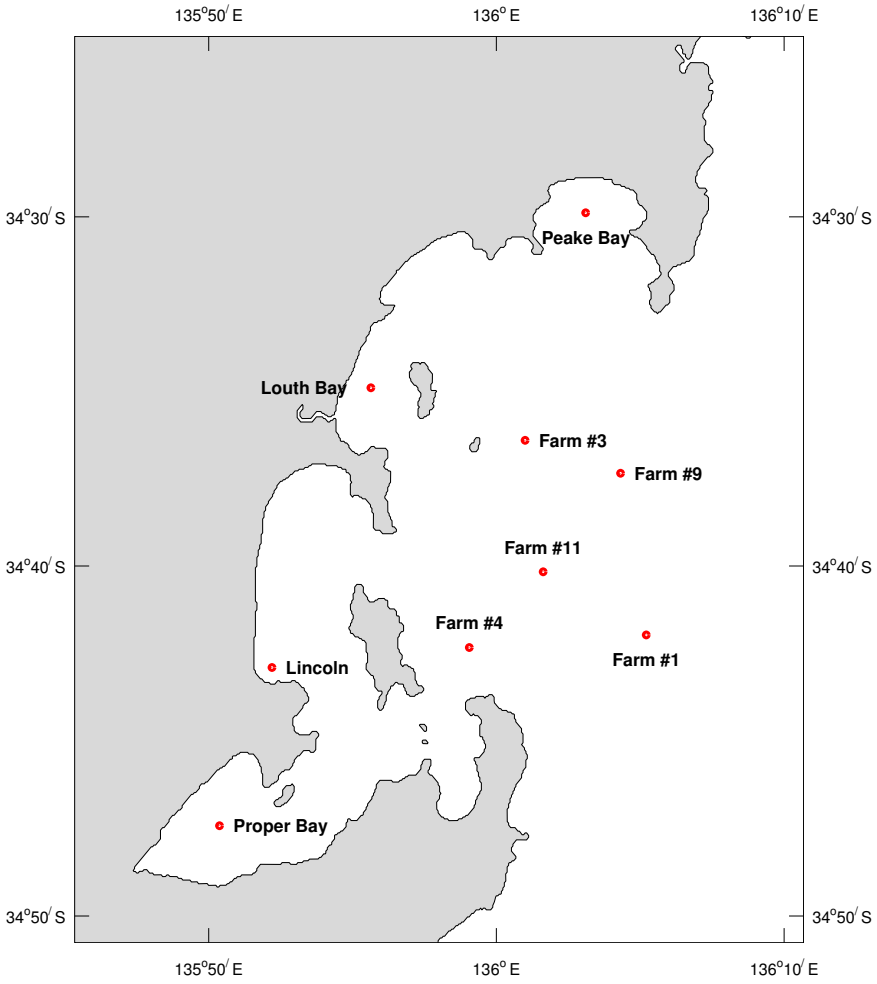

Figure 8.5.1. Point source release locations.

Results are displayed as Figures 8.5.2 to 8.5.11. Results are interpreted thus: given that a continuous unit load is input at the Port Lincoln site and its distribution throughout the domain allowed to reach quasi-steady state, at any given location in the domain one would expect to find the concentrations less than those shown in Figure 8.5.2 (a) for 5% of the time, less than those in Figure 8.5.2 (b) for 50% of the time and less than those in Figure 8.5.2 (c) for 95% of the time. These percentile plots provide a statistical description of the tracer concentration throughout the domain expected from various point source releases. Note that the concentration scales in the figures for the three percentiles generally differ from one another.

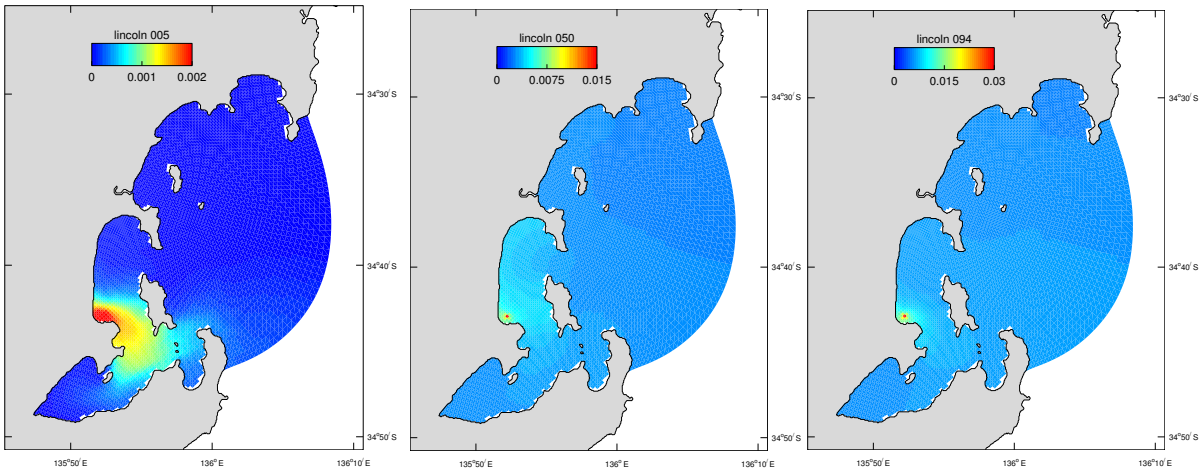

(a) 5 percentile (b) Median (c) 95 percentile

Figure 8.5.2. Quasi-steady state tracer distribution for Port Lincoln release.

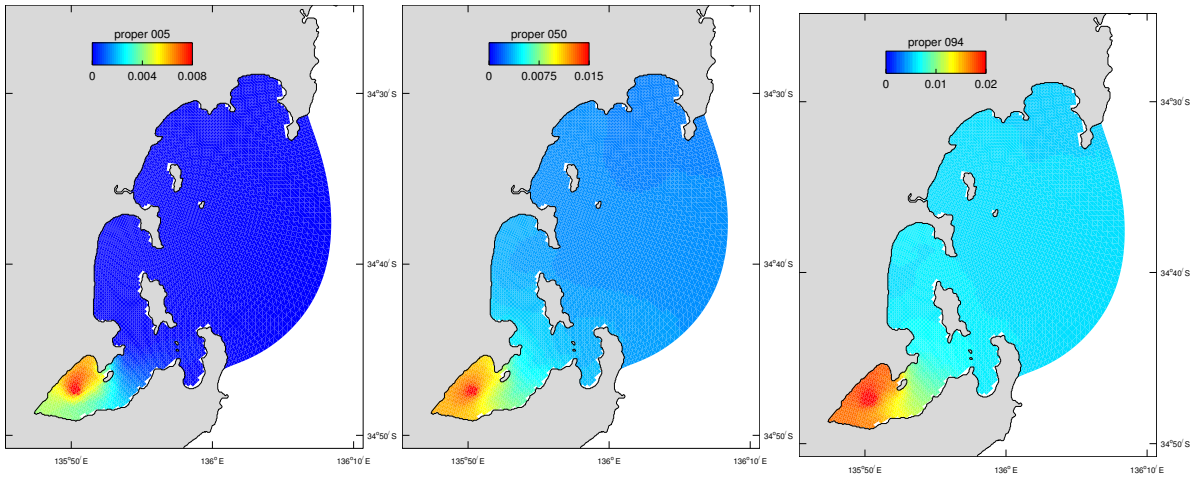

(a) 5 percentile (b) Median (c) 95 percentile

Figure 8.5.3. Quasi-steady state tracer distribution for Proper Bay release.

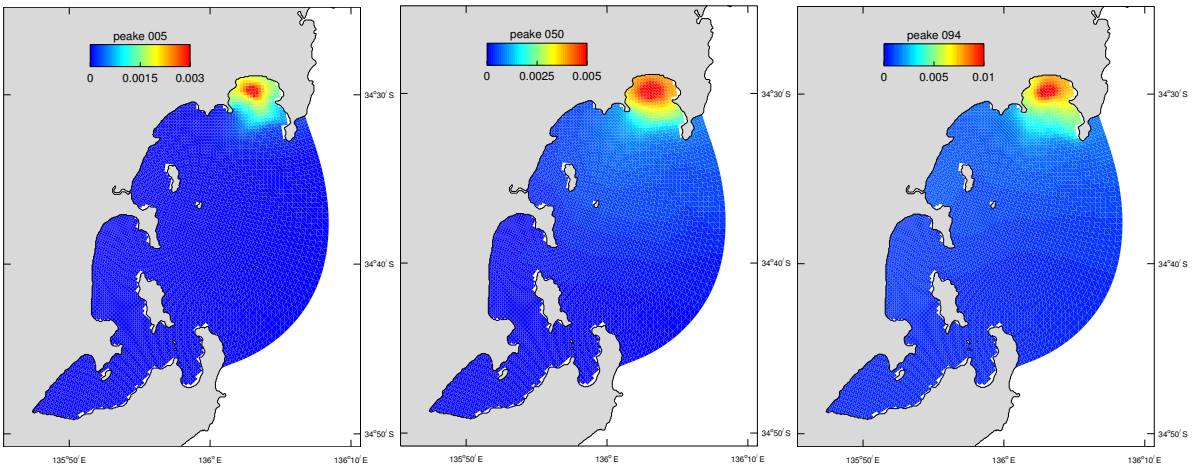

(a) 5 percentile (b) Median (c) 95 percentile

Figure 8.5.4. Quasi-steady state tracer distribution for Peake Bay release.

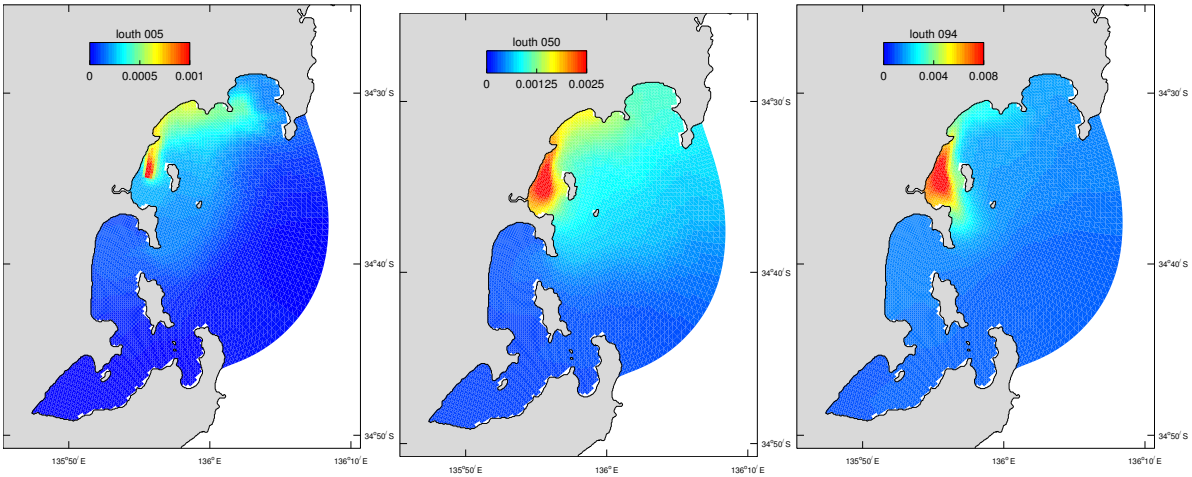

(a) 5 percentile (b) Median (c) 95 percentile

Figure 8.5.5. Quasi-steady state tracer distribution for Louth Bay release.

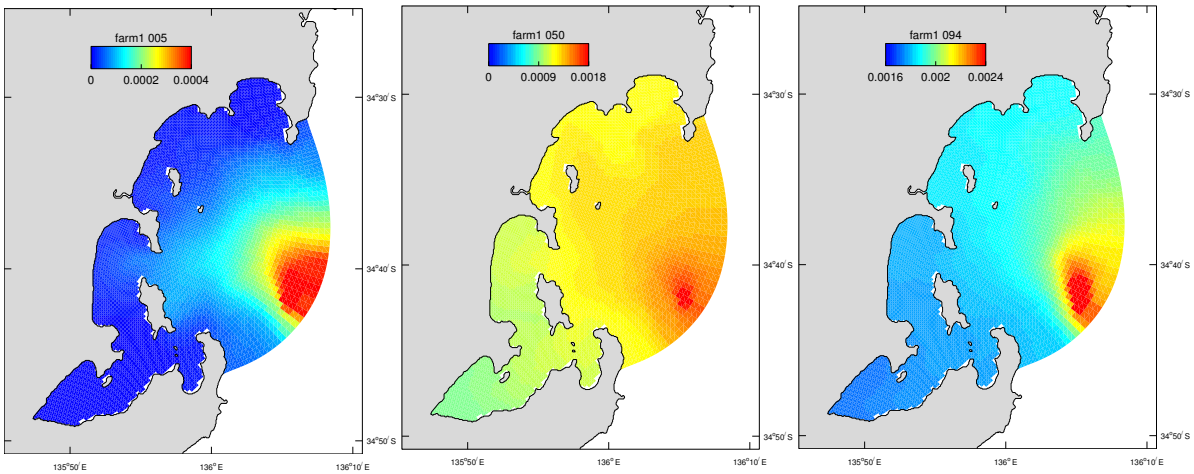

(a) 5 percentile (b) Median (c) 95 percentile

Figure 8.5.6. Quasi-steady state tracer distribution for Farm #1 release.

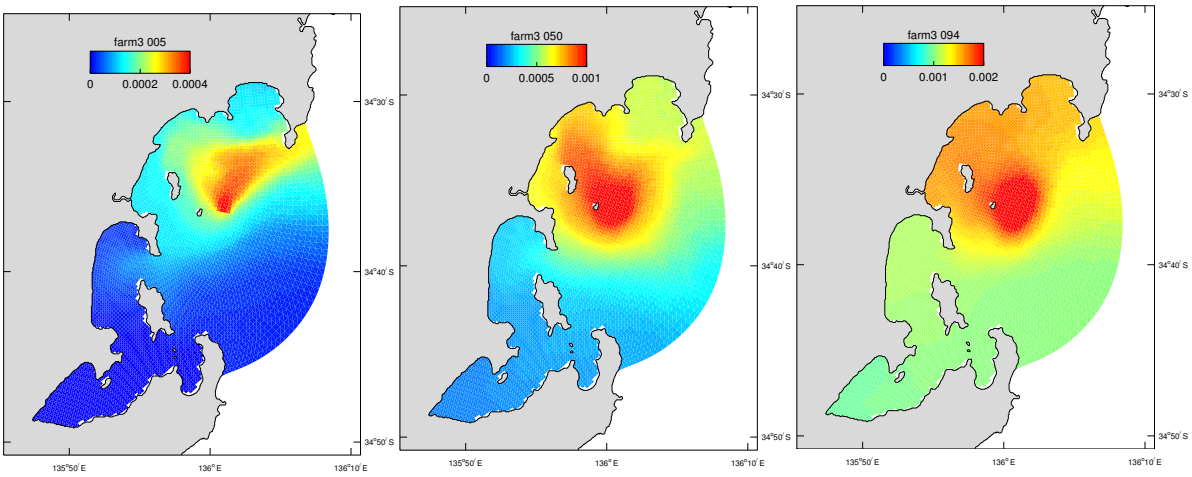

(a) 5 percentile (b) Median (c) 95 percentile

Figure 8.5.7. Quasi-steady state tracer distribution for Farm #3 release.

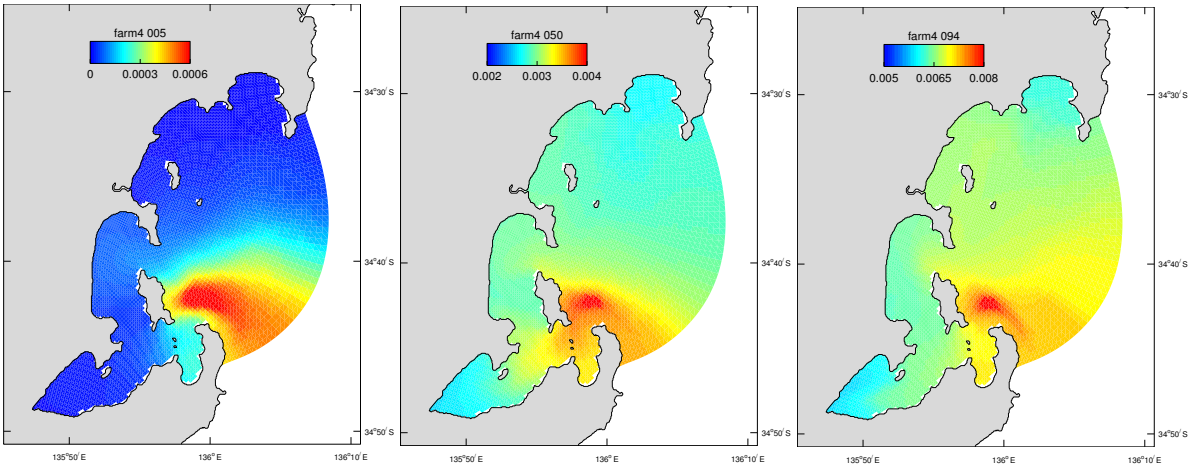

(a) 5 percentile (b) Median (c) 95 percentile

Figure 8.5.8. Quasi-steady state tracer distribution for Farm #4 release.

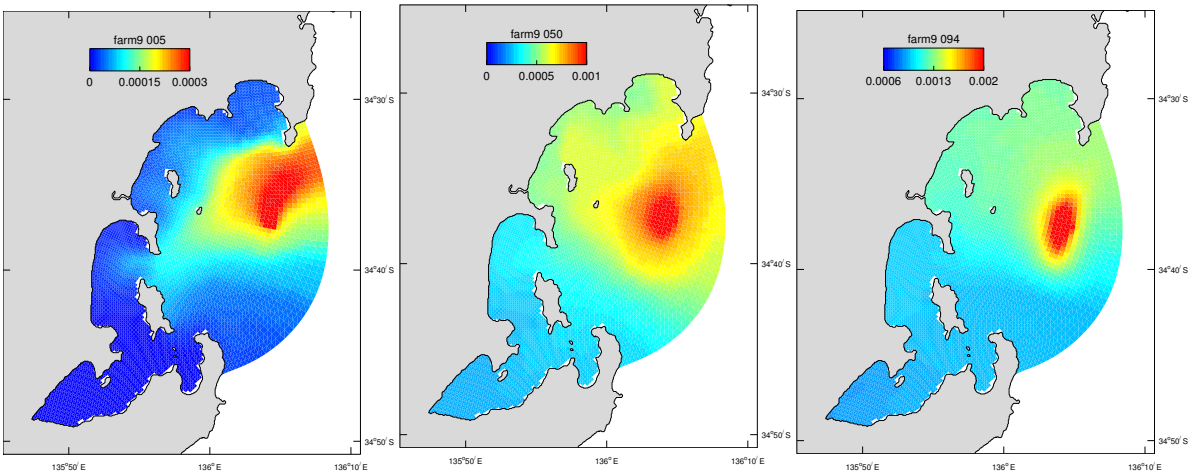

(a) 5 percentile (b) Median (c) 95 percentile

Figure 8.5.9. Quasi-steady state tracer distribution for Farm #9 release.

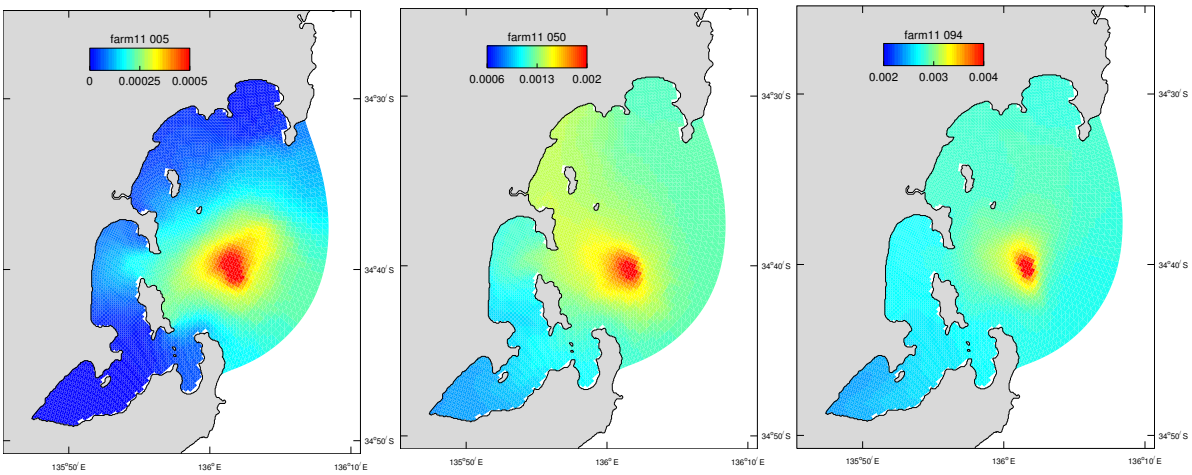

(a) 5 percentile (b) Median (c) 95 percentile

Figure 8.5.10. Quasi-steady state tracer distribution for Farm #11 release.

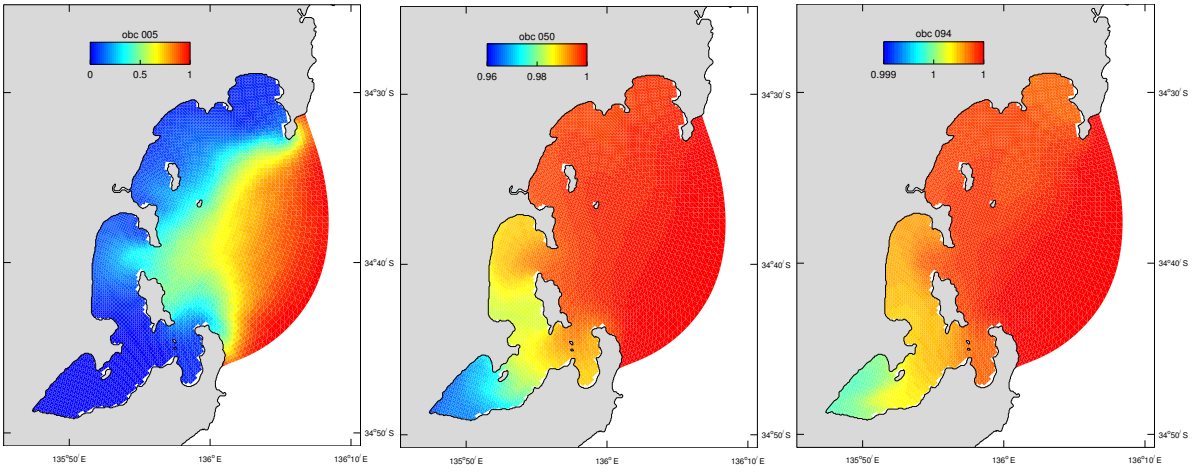

(a) 5 percentile (b) Median (c) 95 percentile

Figure 8.5.11. Quasi-steady state tracer distribution for Open boundary release.

The distributions above indicate that tracer released in the Proper Bay / Port Lincoln area tends to remain in that area; similarly tracer released in Louth or Peake Bays remains restricted to those areas. Tracer released offshore of Boston Island is distributed throughout most of the domain, although concentrations are lower indicating a larger amount of tracer is removed from the system. Connectivity therefore appears to be divided into three separate regions:

1. Landward of Boston Island and Proper Bay, with poor connectivity with the rest of the domain,
2. Louth and Peake Bays, with poor connectivity with the rest of the domain,
3. Regions outside these bays and offshore of Boston Island, with good connectivity with the remainder of the domain, but subject to greater flushing.

The farm sites having tracer released offshore of Boston Island which impinge on the bay regions tend to assume the character of those respective regions; e.g. farm #3 release near

Louth / Peake Bays is less well connected with Proper Bay than tracer released closer to that region (farm #4). Tracer input along the open boundary rapidly finds its way throughout the whole domain, with Proper Bay being the least accessible region. The connectivity of the domain as diagnosed from the point source releases is consistent with the mean depth averaged flow schematic of Figure 8.2.11, where circulation cells are established in Boston / Proper and Louth / Peake Bays, fed by south to north throughflow in the deeper parts of the domain seaward of Boston Island. The circulation cells are of a closed nature and do not promote good connectivity with the remainder of the region.

8.6. Connectivity

The connectivity of the domain can be examined by observing the behaviour of neutrally buoyant particles released from the same locations and depths as the point source releases in Section 8.5. The particles were released at a rate of 2 particles hour^{-1} from an initial pool of 10,000 particles. These particles were subsequently advected with the circulation to provide insight into how various regions of the domain are connected. The particles are also subjected to random motion representing the effect of diffusion (i.e. sub-grid scale effects). Therefore, any two particles released from the same place at the same time are expected to undergo different trajectories due to this random motion. When a particle crosses the offshore open boundary it is placed in the initial pool for subsequent re-release. The particle distributions after 12 months of simulation are displayed in Figures 8.6.1 to 8.6.9. This distribution is the projection of particles at all depths onto the surface. Particles are colour coded according to their age since being released over the range 0 – 30 days (i.e. blue particles are 0 days old, red particles are > 30 days old).

The connectivity of the domain inferred from the particle distributions is in agreement with the point source distributions (Section 8.5). Particles released at Port Lincoln in Boston Bay are confined to that area, whereas those released in Louth Bay remain in the northern vicinity of the domain. Those released near the open boundary (Farm #1 and #9) are rapidly removed, with few particles distributed throughout the domain. Particles within the domain for these release sites are associated with an older age. These distributions are consistent with the depth averaged net flow conceptualized in Figure 8.2.11. The average age of the 122,428 particles that exited the domain was 19.9 days, which is indicative of the flushing time for the whole domain.

Note that these images represent a snapshot of the particle distributions, and will vary in accordance with the forcing in effect. An animation of the particle motion over time best conveys the connectivity of the region, although observation of isolated particle trajectories does supply insight into the dynamics of the system. Trajectories were plotted during spring and neap tides for one tidal cycle (low water to low water). Note that circles correspond to the start of the trajectory and squares to the end in these figures, with the net displacement of start and end locations being indicative of the residual flow. Particle trajectories are superimposed on the surface from all depth levels.

Trajectories under the influence of spring tides show the oscillatory nature of the tide (Figure 8.6.10), especially near the offshore boundary. Gross displacements may be large, over 8 km, but small net displacements are observed. Neap tide trajectories exhibit little tidal motion, with particle displacement dominated by the wind (Figure 8.6.11 on 7 January 2006 for an easterly wind, showing net westward motion). Dodge tides reveal a similar situation to neap tides (Figure 8.6.12).

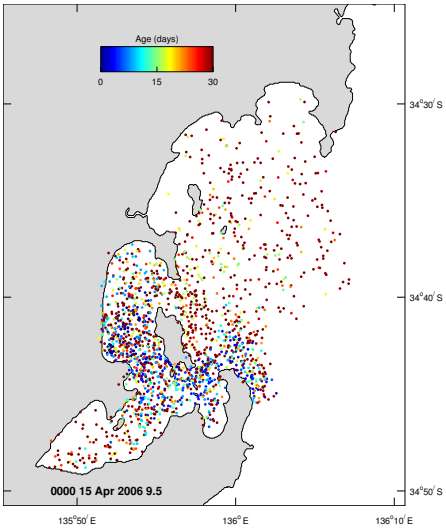

Figure 8.6.1. Particle distribution by age for particles released at Port Lincoln.

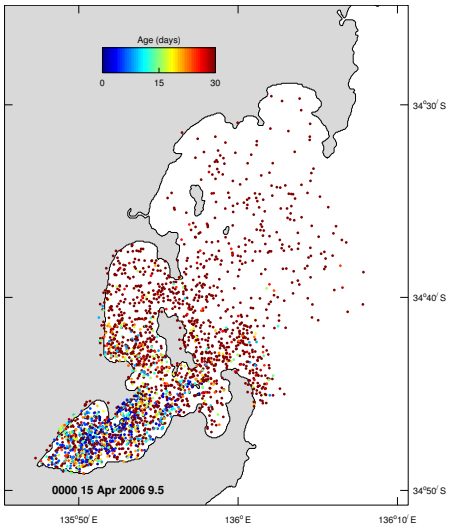

Figure 8.6.2. Particle distribution by age for particles released at Proper Bay.

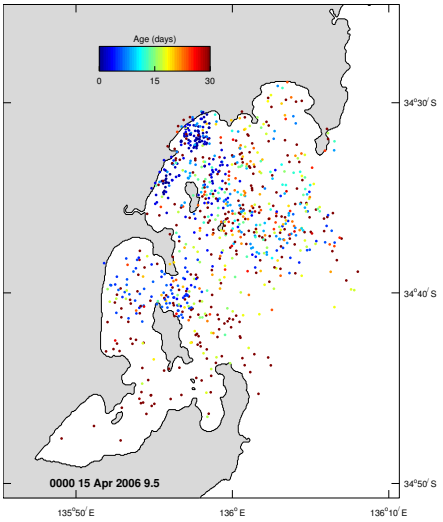

Figure 8.6.3. Particle distribution by age for particles released at Louth Bay.

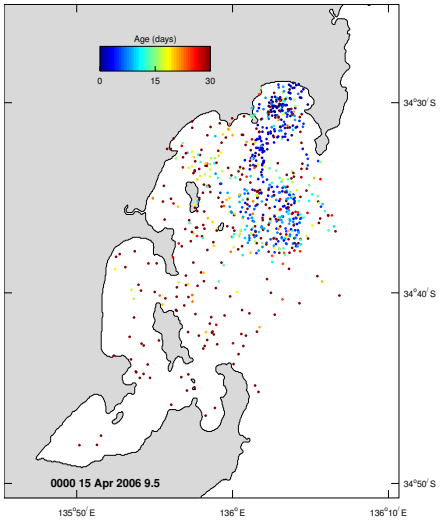

Figure 8.6.4. Particle distribution by age for particles released at Peake Bay.

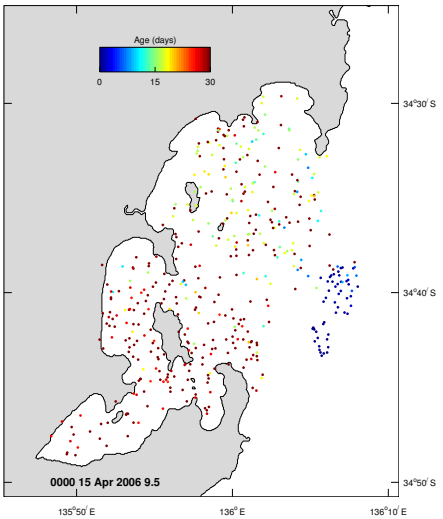

Figure 8.6.5. Particle distribution by age for particles released at Farm #1.

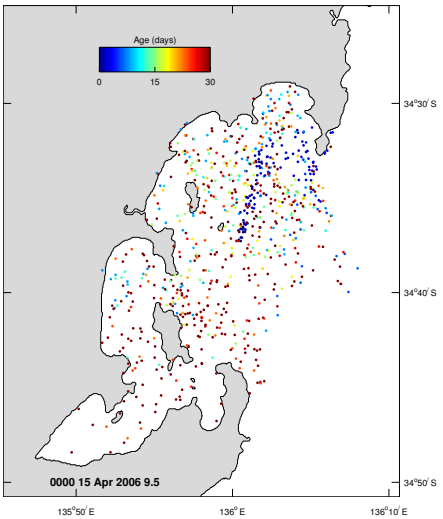

Figure 8.6.6. Particle distribution by age for particles released at Farm #3.

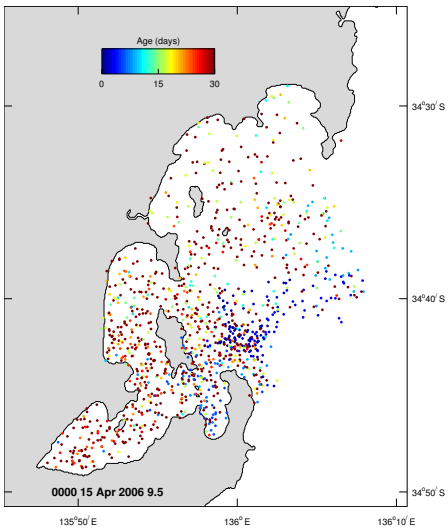

Figure 8.6.7. Particle distribution by age for particles released at Farm #4.

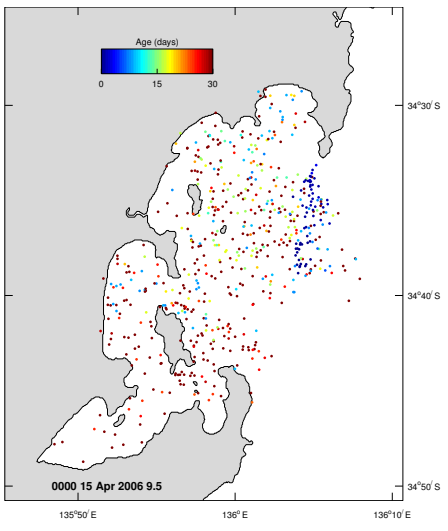

Figure 8.6.8. Particle distribution by age for particles released at Farm #9.

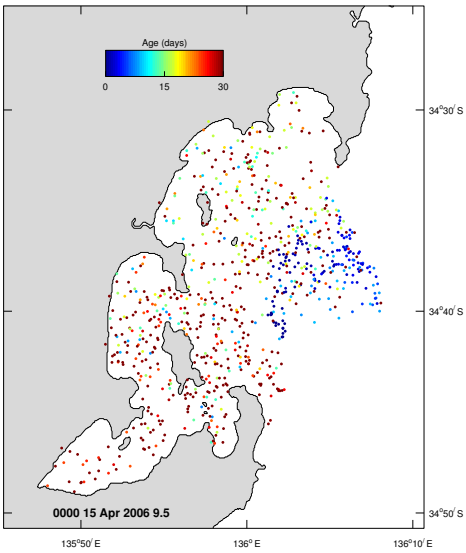

Figure 8.6.9. Particle distribution by age for particles released at Farm #11.

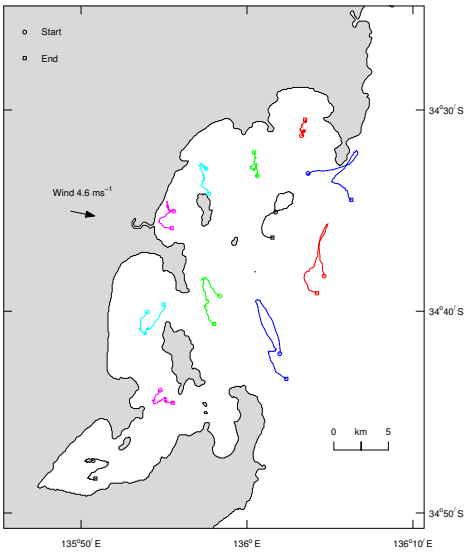

Figure 8.6.10. Spring tide trajectory, 22 Oct.

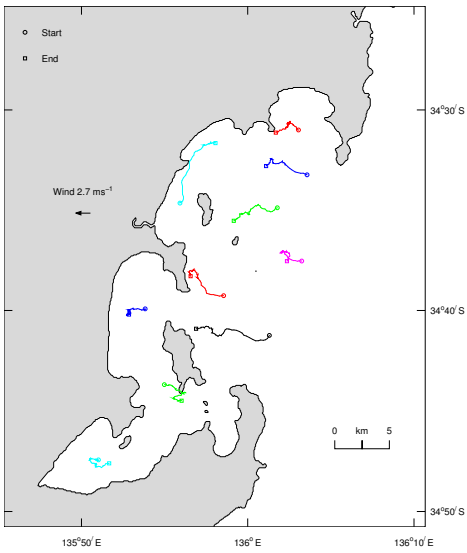

Figure 8.6.11. Neap tide trajectory, 7 Jan.

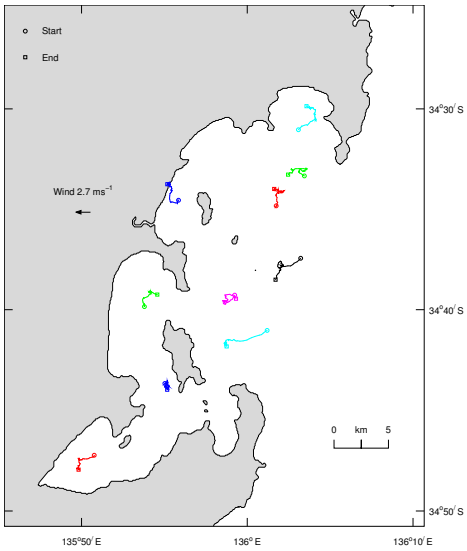

Figure 8.6.12. Dodge tide trajectory, 8 Jan.

9. Conclusions

A 3D primitive equation model was applied to the TFZ to examine the hydrodynamics of the region. Using a nesting process to provide boundary conditions for the TFZ model, the region was represented with high resolution while incorporating forcing due to wind stress, tides, low frequency sea level oscillations and pressure gradients due to temperature and salinity distributions. The open boundaries of this model were supplied from a larger scale regional model that encompassed the whole of Spencer Gulf. This model was in turn forced with data collected in the field. The model was simulated for 12 months for the period Sep 2005 – Aug 2006 and calibrated to sea level measurements at Port Lincoln, Whyalla and Wallaroo, and temperature, salinity and velocity at numerous locations in the TFZ region obtained from a dedicated field program. The model was able to successfully reproduce tidal and low frequency sea level oscillations in both regional and TFZ models. Temperature, salinity and currents corresponding to tidal (diurnal) and weather band (periods 3-20 days) frequencies were also successfully reproduced by the model.

Both the data and model results showed there to be strong (~20 cm s^{-1}) tidal currents that may be implicated in bottom stirring. Although the tide may be responsible for trajectories of over 8 km, the net displacements due to these currents are small (less than 1.4 km over a 3 hr period). Magnitudes of the weather-band currents are smaller than the tidal currents (< 5 cm s^{-1}), but due to their longer periods these currents are the dominant contributor to residual flow and hence primarily responsible for transport and flushing of the region. Both data and model indicate the residual currents eastward of Boston Island (in the tuna farming zone) to be weak (~ 1 cm s^{-1}) and to the north/north east during both summer and winter. The transport due to these flows over a 3-month period is around 80 km. The currents were also found to be strongly sheared in the vertical and so may be important to shear enhanced diffusion and dispersal. However, estimates of the flushing times based on tracers and Lagrangian tracking show flushing time-scales of 10 days (Boston Bay) to 2 days for the outer bay region. The flushing time for the whole domain based on particle tracking is ~20 days.

The tide in the region is classified as semi-diurnal mixed and is dominated by the semi-diurnal constituents M2 and S2, and the diurnal constituents K1 and O1. Coincidentally, all these constituents have approximately the same amplitude of ~0.18 m, and when they are out of phase they destructively combine to produce very little tidal variation for several days. During these periods, called the ‘dodge tide’, the tidal currents are small and transport is primarily wind driven. If wind-speed is low, then it is possible that the region is very poorly flushed. The model was able to reproduce the occurrence of the dodge tide, allowing predictive capability of the timing of these events.

There exists a degree of connectivity between the coastal zone and the TFZ region in summer that can be caused by local upwelling. Offshore (eastward) winds force surface waters offshore, resulting in compensatory onshore interior or bottom flow. In addition, the larger evaporation that occurs near the coast leads to dense water formation and bottom plumes that flow to the outer bay region. During winter, similar plumes result from coastal cooling rather than evaporation. The annual temperature cycle in the TFZ region is largely driven by atmospheric heating and cooling. Salinity is also controlled by atmospheric exchanges, but to a lesser extent, with advective processes playing a dominant role. Large decreases in salinity in autumn occur, coincident with the flushing of Spencer Gulf when fresher compensatory

oceanic flows enter western Spencer Gulf. Due to the atmospheric exchanges, the TFZ was found to be stratified during summer and well mixed during winter.

The depth averaged seasonal flow can be divided into three main sub-regions within the domain. Firstly, offshore of Boston Island flow enters the domain in the south and exits in the north, with little penetration into the coastal margins. Secondly, the Boston Bay / Proper Bay area can be treated as a separate system, with flow generally entering north of Boston Island, flowing south to loop through Proper Bay and exiting to the east of Boston Island, where a persistent anti-clockwise gyre exists off Cape Donnington. Thirdly, Louth and Peake Bays exhibit northwards flow along the coast, fed by water seaward of Point Boston, and seasonally exhibiting gyres within Peake Bay and off Louth Island.

This residual flow determines the connectivity of the region, which consequently can be categorised into three main sub-regions, consistent with passive tracer and particle tracking analyses;

1. A region encompassing Proper Bay and the area landward of Boston Island, which has poor connectivity with the rest of the domain,

2. Louth and Peake Bay's, which also have poor connectivity with the rest of the domain,

3. Regions outside these bays and offshore of Boston Island with good connectivity with the remainder of the domain, but subject to greater flushing.

The TFZ numerical model was found to have satisfactory predictive skill, and as such is a suitable tool to couple to sediment transport and biogeochemical models to allow transport of nutrients/sediments etc through the model domain, and thus to provide a realistic spatial model of the dynamics of these substances.

10. References

Atkinson I. et al (2004) Field report on the second survey of dry season water column and sediment properties in the Fitzroy Estuary and Keppel Bay, Rockhampton Queensland, August 15 – September 1, 2004. Coastal CRC, Contaminants dynamics sub-project. Milestones AC09, AC11,AC43 and AC44.

Blanc, T.V. (1985) Variation of bulk-derived surface flux, stability, and roughness results due to the use of different transfer coefficient schemes. *J. Phys. Oceanogr.*, 15, 650-669.

Blumberg, A.F. and Herring, J., (1987) Circulation modelling using orthogonal curvilinear coordinates, in *Three-Dimensional Models of marine and Estuarine Dynamics*, eds. Nihoul, J.C.J and Jamart, B.M., Elsevier.

Blumberg, A.F. and L.H. Kantha (1985) Open boundary condition for circulation models, *J. Hydraulic Engineering*, 111, pp237-255.

Eanes, R. and S. Bettadpur (1995) The CSR 3.0 global ocean tide model. *Center for Space Research, Technical Memorandum, CST-TM-95-06*.

Easton, A. K. (1970). The tides of the continent of Australia. Horace Lamb Centre for Oceanographical Research, Res. Paper 37, Flinders University, South Australia.

Easton, A. K. (1978). A Reappraisal of the Tides in Spencer Gulf, South Australia. *Aust. J. Mar. Freshw. Res.* 29, 467-477.

Griffes, S.M., Hallberg, R. W., (2000) Biharmonic friction with a Smagorinsky viscosity for use in large-scale eddy-permitting ocean models. *Mon. Weath. Rev.*, 128, 2935-2946.

Herzfeld, M. (2005) SHOC, sparse hydrodynamic ocean code, scientific manual. CSIRO Marine and Atmospheric Research.

Herzfeld, M. (2006) An alternative coordinate system for solving finite difference ocean models. *Ocean Modelling*, 14, 174 – 196.

Kitaigorodskii, S.A., O.A. Kuznetsov and G.N. Panin (1973) Coefficients of drag, sensible heat and evaporation in the atmosphere over the surface of the sea. *Izv. Acad. Sci. USSR*

Kondo, J. (1975) Air-sea bulk transfer coefficients in diabatic conditions. *Boundary-Layer Meteorology*, 9, 91-112.

Large, W.G., and S. Pond (1981) Open ocean momentum flux measurements in moderate to strong winds, *J. Phys. Oceanogr.*, 11, 324-336.

Lennon, G.W., D.G. Bowers, R.A. Nunes, B.D. Scott, M. Ali, J. Boyle, C. Wenju, M. Herzfeld, G. Johansson, S. Nield, P. Petrusevics, P. Stephenson, A.A. Suskin and S.E.A. Wijffles (1987) Gravity currents and the release of salt from an inverse estuary. *Nature*, 327, 695-697.

Leonard, B.P. (1979) A stable and accurate convective modelling procedure based on quadratic upstream interpolation. *Comp. Methods in Appl Mech. and Eng.*, 19, 59 – 98.

Leonard, B.P. (1991) The ULTIMATE conservative difference scheme applied to unsteady one-dimensional advection. *Comp. Methods in Appl. Mech. and Eng.*, 19, 17 – 74.

McClatchie, S., J.F. Middleton and T. Ward (2006) Water mass analysis and alongshore variation in upwelling intensity in the eastern Great Australian Bight. *J. Geophys. Res.*, 111, C08007, doi:10.1029/2004JC002699.

Masagutov, T.F. (1981) Calculation of the vertical turbulent fluxes in the near-water atmospheric layer over the ocean in tropical latitudes. *Meteor. Gidrol.*, 12, 61-68.

Mellor, G.L. and T. Yamada (1982) Development of a turbulence closure model for geophysical fluid problems. *Rev. Geophysics and Space Phys.*, 20(4), 851-875.

Miller, M.J. and A.J. Thorpe (1981) Radiation conditions for the lateral boundaries of limited-area numerical models. *Q. J. R. Meteorol. Soc.*, 107, 615 - 628.

Middleton, J. F., Platov, G. (2003). The Mean Summertime Circulation along Australia's Southern Shelves: a numerical study. *J. Phys. Oceanogr.*, 33(3), 2270-2287.

Middleton J. F., Platov, G. (2005). Hydrodynamic model of the Great Australian Bight. Ward T., Goldsworthy S. D. and B. C. Page, Eds, In Tropho-dynamics of the GAB: Assessing the Need for an Ecological Allocation in the SA Pilchard Fishery. Report to the Fisheries Res. Develop. Corp., Proj. Number 2003/072, SARDI Aquatic Sciences Publication Number RD03/0166-2, pp 51-99.

Middleton J. F., Arthur, C., van Ruth, P., Ward, T., McClean, J., Maltrud, M., Gill, P., Levings, A., Middleton, S. (2007). El Nino effects and upwelling off South Australia., *J. Phys. Oceanogr.*, 37, 2458-2477.

Middleton, J.F, and C. Teixeira (2008) Wind-forced motion in Spencer Gulf: a numerical study. In prepararion.

Nixon, J. B., Noye, B. J. (1999). Prawn Larvae Advection-Diffusion Modelling in Spencer Gulf. In Noye, B.J., ed., Modelling Coastal Sea Processes, p189-218.

Noye, B. J., Matthews, K., Grzechnik, M. P. (1999a). A three dimensional model of tides and surges in the Great Australian Bight. In Noye, B.J., Ed., Modelling Coastal Sea Processes, p107-134.

Noye, B. J., Grzechnik, M., Stevens, J. M. (1999b). Modelling Currents and Dispersion in Boston Bay, South Australia. In Noye, B.J., ed., Modelling Coastal Sea Processes, 1, 247-272.

Nunes Vaz, R.A., Lennon, G. W., Bowers, D. G. (1990). Physical Behaviour of a large inverse estuary. *Cont. Shelf Res.*, 10, 277-304.

Nunes, R.A., Lennon, G. W., (1987). Episodic Stratification and Gravity Currents in a Marine Environment of Modulated Turbulence. *J. Geophys. Res*., 92, 5465-5480.

Petrusevics. P.M. (1993). SST fronts in inverse estuaries, South Australia – indicators of reduced gulf-shelf exchange. *Aust. J. Mar. Freshwater Res.* 44 305-323.

Petkovic, P., Buchanan, C., (2002) January 2002 edition of the AGSO bathymetry. Geographic projection WGS84 Datum. Australian bathymetry and topography grid. Canberra: Geoscience Australia.

Ridgway, K. J., Dunn, J., Griffin, D., Cahill, M., (2006) SynTS – a 3D ocean observational analysis for the Australian region, Second Argo Science Workshop, Venice, Italy.

Ridgway K. R., J. R. Dunn and J. L. Wilkin (2002) Ocean interpolation by four-dimensional least squares -Application to the waters around Australia, *J. Atmos. Ocean. Tech*., 19, 1357-1375.

Simons, T.J., (1974) Verification of numerical models of lake Ontario. Part I, circulation in spring and early summer. *J. Phys. Oceanog.*, 4, 507 – 523.

Simpson, J.J. and T.D. Dickey (1981) The relationship between downward irradiance and upper ocean structure. *J. Phys. Oceanog.*, 11, 309 - 323.

Smagorinsky, J. (1963) General circulation experiments with the primitive equations, I. The basic experiment. *Mon. Wea. Rev.*, 91, 99 – 164.

Smith, S.D., (1980) wind stress and heat flux over the ocean in gale force winds. *J. Phys. Oceanogr.*, 10, 709-726

Tanner, J.E. & J.K. Volkman (2008) Aquafin CRC - Southern Bluefin Tuna Aquaculture Subprogram: Risk and Response – Understanding the Tuna Farming Environment. Technical report, Aquafin CRC Project 4.6, FRDC Project 2005/059. Aquafin CRC, Fisheries Research & Development Corporation and South Australian Research & Development Institute (Aquatic Sciences), Adelaide. SARDI Publication NoF2008/000646-1, SARDI Research Report Series No 344, 289 pp.

Tartinville, B., E. Deleersnijder and J. Rancher (1997) The water residence time in the Mururoa atoll lagoon: sensitivity analysis of a three-dimensional model. *Coral Reefs*, 16, 193 – 203.

Thompson, R.O.R.Y. (1983) Low-pass filters to suppress inertial and tidal frequencies. *J. Phys. Oceanogr.*, 13(6), 1077-1083.

Walker, S.J. and J.R. Waring (1998) A multiple grid, 3-dimensional, non-linear, variable-density hydrodynamic model with curvilinear horizontal coordinates and level (z) vertical coordinates, CSIRO Marine Research, Report OMR-118/120.

11. Appendix A: A Re-Analysis of the Gulf Mouth Sea Level Data

11.1. Summary

The sea level records from M1 and M2 were found to have datum shifts of 10 – 20 cm brought about by re-deployment of the instruments at slightly different depths after servicing. Such datum shifts must be eliminated if the data is to be used to drive the model open boundary for periods longer than the minimum period of co-incident data (42 days). In addition, from the equipment available, the pressure sensors used on moorings M1 and M2 only gave estimates of sea level height to within a centimetre or so and no averaging was made to eliminate aliasing due to waves. Depths were recorded every 15 minutes. Mooring M3 did use a high quality tide gauge sensor and the 15 minute samples were obtained as burst (4 minute) averages. Thus, the quality of the M1 and M2 sea level data remains to be determined.

To this end a re-analysis is made of the low-passed filtered sea level data from the gulf sites M1 to M5. First, the low-pass filtered data at site M5 is found to be very similar to that at site M1 so that data from the former (M5) can be used to produce a long 10 month time series of continuous data at site M1. This also gives confidence in the M1 data collected. Similar continuous data sets are obtained for site M2 and M3. The seasonal sea level signal at M3 is assumed for sites M1 and M2 and the underlying assumption is that no net geostrophic flow into the gulf occurs for periods 2 months or greater. Using these long time series, a simple conceptual model is then developed to explain the net in/out flows into the gulf mouth that appear to be driven in part by the alongshore wind stress. The M1, M2 and M3 sea level data also suggests the existence of anticyclonic (cyclonic) circulation patterns near the gulf mouth and during periods of upwelling (downwelling) winds. These results are in qualitative agreement with recent numerical studies elsewhere (Middleton and Teixeira 2008).

With care, the M1, M2 and M3 time series will be used to drive the SHOC model.

11.2. The sea level data

A summary of the sea level data is given in Table 11.1. As shown in the first row, there are four coincident periods (42-68 days) when all M1, M2 and M3 data were obtained. The sub-records for these periods have been extracted, filtered to remove tides and then de-meaned. The results will be presented below. However, low-pass filtering loses 10 days per record and the result is that the final (gappy) sub-records are too short to be useful for driving the low-frequency circulation (3-20 day period) at the mouth of the gulf.

Here, we outline a re-analysis of the data so as to fill the gaps in the raw data, and derive three long time series at M1, M2 and M3 that might be useful in driving the model and in inferring the (low-frequency geostrophic) circulation near the gulf mouth.

11.3. Creation of long time series

To create the longest times series possible for each of the M1, M2 and M3 sites, the missing records were filled using the following procedure on the raw data files. First, each sub-series (Table 11.1) had the arithmetic means removed. The resultant data series were labelled rawmnd.dat where m=1,2,3,4,5 or 6 denotes the mooring site and n=1,2,3 or 4 the deployment period (see Table 11.2).

Table 11.1. Start and end times of mooring data. The first row lists the maximum coincident period for moorings 1, 2 and 3. The relevant start and finish times for the appropriate mooring are highlighted in bold. The last row lists the subsequent gaps between each of the maximum coincident periods in the first row. For M3, only two deployments were made and the data spans the periods indicated. These periods are indicated in days since 1990 that is adopted for the modelling. Some calendar dates are included.

Mooring	**Deployment 1 68 days Sept-Oct**		**Deployment 2 63 days Dec-Jan**		**Deployment 3 42 days March-April**		**Deployment 4 55days May-June OR 79 days May-July**	
	start	end	start	end	start	end	start	end
M1	5720.5	5790.25 – Nov 8	5812.375	5918.25	5918.5 - March 16	5981.5	5981.75 May 18	6066.37
M2	5722.62 - aug30			5875.375 – Feb 1	5875.625	5974.45 May 11	5987.625 –May 24	6085.5
M3	5722.37			5888.5 48 Feb 14	5888.75 March 14			6070.25
M4	5721.5	5793			5887.5	5963	5981.625	6050.37
M5	5720.5	5792	5799.5	5878	5887.5	5960.625	5981.5	6045
M6							5981.75	6042.37
		22 day gap		43 day gap		17 day gap		

Table 11.2. Means (cm) of raw, filtered and filtered & trimmed data sub-series for deployments d1, d2, d3, d4. A dash means no data for that period. Documentation for the calculation of the means indicted by the ^ have not been located.

Data file	**Mean deploy 1**	**Mean deploy 2**	**Mean deploy 3**	**Mean deploy 4**
rawm1d*	441.1	407.6	420.92	477.2
fm1d*	440.3	406.7	421.6	477.5
fm1s*	440.4	409.5	418.8	477.5
rawm2d*	-----	0.000^	537.96	540.15
fm2d*	--------	0.85^	537.85	540.21
fm2s*				
rawm3d*	---------	4833.0	----------	4847.7
fm3d*	---------	4833.3	----------	4847.0
fm3s*				
rawm4d*	1380.1	---------	965.5	903.8
fm4d*	1379.7	----------	965.0	905.0
fm4s*	1379.8	----------	970.1	904.7
rawm5d*	1853.5	1989.2	2005.3	2013.4
fm5d*	1852.9	1990.6	2005.9	2015.0
fm5s*	1853.2	1992.6	2010.0	2015.0

Subtraction of the means is necessary due to the arbitrary datum shifts (water depths) that arose after servicing and redeployment. From Table 11.2, these can be large (~10-40 cm) and without correction will drive significant and erroneous geostrophic currents. Note, the datum shifts can also arise from seasonal and intra-seasonal (ENSO) influences.

Filling the Gaps:

Site M1: This site has the most and longest gaps. Based on the observation below that the M5 and M1 low pass filtered data are almost identical for the August - December 2005 period, the M5 data was used from deployment periods 1 & 2 to cover the period 5720.50 to 5812.33. There is a 7.5 day gap between these two records from 5792.04 to 5799.00. This was filled with data from site 2 so that the net geostrophic flow into the gulf is implied to be zero for this period.

After time 5812.33, the raw data from site 1 was used and the remaining ¼ day gaps filled using the hourly data from the following or proceeding day.

Site M2: The first two deployment files were added and the 1/3 day gap interpolated using the following ¼ day of data. A 13 day gap between this file and the next file was interpolated using 13 days of data from site 1. The net geostrophic flow thru the gulf mouth is therefore zero over this time (11-24th May 2006).

Site M3: This site has only a ¼ day gap that was filled using hourly values from the following day's time series.

The process above ensures that the time series at each site are continuous (days 5720.50 to 6042.37) and the datum shifts are eliminated: the cost of elimination is that each of the sub-records used to obtain the continuous series have zero mean and thus the implied net geostrophic flow (proportional to the sea level difference) into the gulf is necessarily zero (2 months or longer).

The resultant continuous series were called rawm1.dat, rawm2.dat etc. These were then filtered using the Thompson (1984) low pass filter (cut-off 29hrs). The filter results in a loss of 5 days of data at each end of the time series. These three series were then trimmed so that all start at 5725.500 and end at 6061.375 and given the labels fmklong.dat where k=1,2 or 3 denotes the site.

Figures 11.1, 11.2 and 11.3 contain the long filtered time series for sites 1, 2 and 3 along with the short (original) filtered records. The mean of each sub-series is set to zero as is the mean of the long records. As can be seen, the long and short records generally differ by some constant suggesting that seasonal or intra-seasonal effects are important.

Seasonal Effects:

To determine these, we have calculated a running 2-month average of the long time series (Figure 11.4). As is evident, the seasonal variability indicated is much larger at M3 than either M1 or M2. This is thought to be due to the number of sub-records used to determine each long time series. For M3, only 2 sub-records were used and each was around 5 months in length. For M1 and M2, 4 records were used and for each the sub-record the mean was subtracted (and thus part of the seasonal trend).

In Figure 11.5 we present the 3-month averaged sea level from sites between Victor Harbour and Thevenard as obtained by Middleton et al (2007). Clearly there is a great deal of variability at the seasonal and intra-seasonal time scales. Middleton et al (2008) have averaged the monthly averaged data from Outer Harbour and Thevenard to obtain the seasonal signal shown in Figure 11.6. It has a maximum amplitude of only 3 cm and much less than the 2005-2006 value from M3 which is about 10 cm. The reason for the difference may be in part due to the El Nino effects which will act to lower sea level at all sites by the same amount. Plotted along with the sea level is the –nino3.4 index which when negative (positive) indicates El Nino (La Nina) conditions. It is evidently correlated with the sea level signals, and for 1998-1999 the El Nino signal in sea level was about 7 cm.

Readjusting the Data:

The differences in the seasonal values of sea level at sites 1, 2 and 3 are thought to be due to the subtraction of the means for each component sub-series used. Since M3 has the best sea level sensor and least sub-records, we will adopt its 2-month running mean for both M1 and M2. This is simply done by subtraction of the means shown in Figure 11.4 from the long time series and then by the addition of the 2-month running mean for M3. The underlying assumption is then that there is no net geostrophic flow into gulf at periods of 2 months or more.

The resultant readjusted filtered/trimmed long records are shown in Figure 11.7. We next investigate the reliability or otherwise of these records.

11.4 Geostrophic Currents

To investigate this we have determined the net geostrophic velocity (v12) into the gulf mouth using the difference in sea level between sites 1 and 2. The results are presented in Figure 11.8 along with Ekman velocity computed from the Neptune Island wind stress and off-set by -20 cm s^{-1} for clarity. An average water depth of 20 m is assumed. Note that both velocities have been further filtered using a 3-day running block-average to mask the large 2-3 day variability.

Notably, the positive geostrophic velocities (into the gulf) are inversely correlated with the negative Ekman velocities (out of the gulf). This inverse correlation is consistent with a simple geostrophic model shown in Figure 11.9. For the upwelling favourable winds shown, the surface (out of gulf) Ekman transport must be largely offset by an into gulf geostrophic velocity. This geostrophic velocity must be accompanied by a relative high on the western side of the gulf (as indicated by the H). For downwelling favourable winds, the reverse holds and the model is crudely consistent with the observations in Figure 11.8.

Note, in this simple model, we ignore effects that arise from the onshore winds, density and friction in the bottom boundary.

In addition, we note that when the winds relax, that the sea level difference across the gulf mouth may vanish and the alongshore flow bends into the gulf mouth as shown in Figure 11.10.

Now let us examine the geostrophic velocities between M1 and M3 (v13) and M3 and M2 (v32) shown in Figure 11.11 and 11.12. In Figure 11.12, a 3-day running average has been

applied to mask out the large 2-day variability and the alongshore wind stress is also shown. The geostrophic velocities here (Figure 11.12) are remarkably much larger (~20 cm s^{-1}) than the net between M1 and M2 (~5 cm s^{-1}) and largely self-compensating. That is, when there is a large flow into the gulf between M1 and M3, there is also a large flow out of the gulf between M3 and M2.

In addition, when the winds are upwelling favourable (days 5790-5810 & 5850-5920), there is an inflow between M1 and M3 (western side) and an outflow between M3 and M2 (eastern side). This flow suggests an anticyclonic circulation for upwelling conditions at the gulf mouth, such that the net transport may be largely set by the Ekman Transport. The reverse holds during downwelling winds.

The conceptual model above is supported by the numerical studies of Middleton and Teixeira (2008) who have examined the gulf response to idealized forcing by oscillatory winds. We conclude that the long, filtered time series may be indicative of true sea level although the variations in seasonal effects suggest they be used with care. In addition, the adjusted long time series for M1, M2 and M3 have been filtered using the Thompson filter (cut-of 29 hrs), but still contain much of the 2-3 day variability that is apparent in all the sea level records and wind stress. This adjusted data may need to be further filtered in line with other filtered data (wind stress) used to force the SCHOC model. In addition, the seasonal means were artificially set to the first (and last) constant value for M3 over the first 30 (and last 30 days) shown in Figure 11.8 (lower panel). Thus, the model results over these times may be suspect.

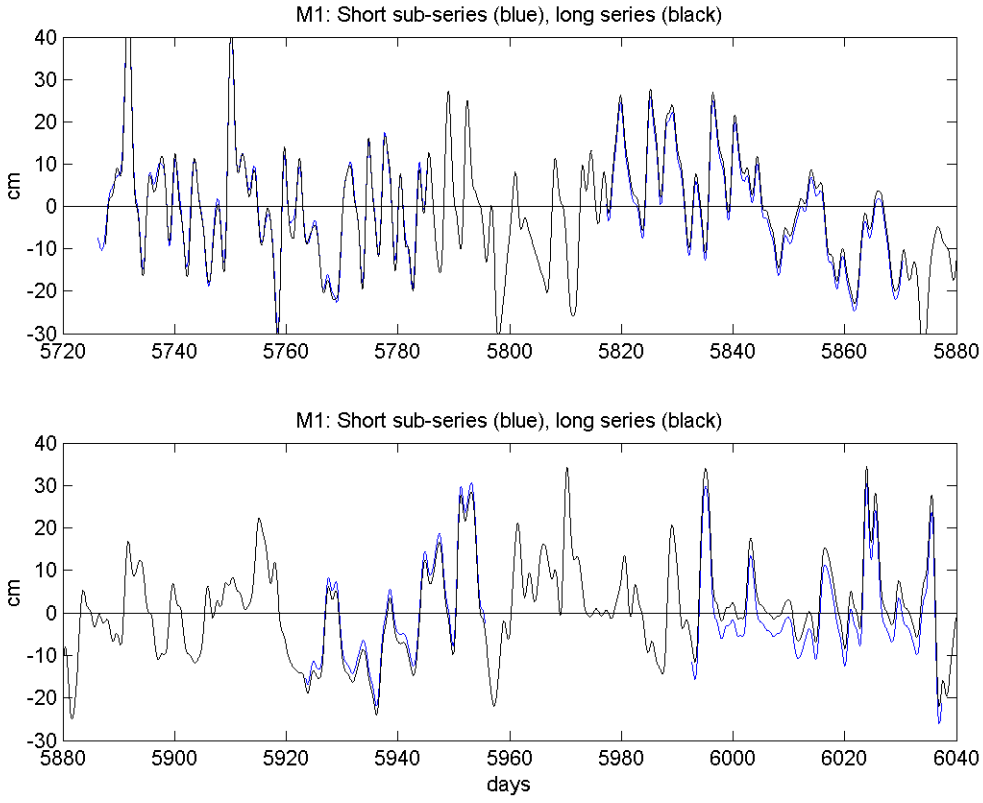

Figure 11.1. The long (black) and short (blue) sea level series for M1. Each long and short time series has zero mean.

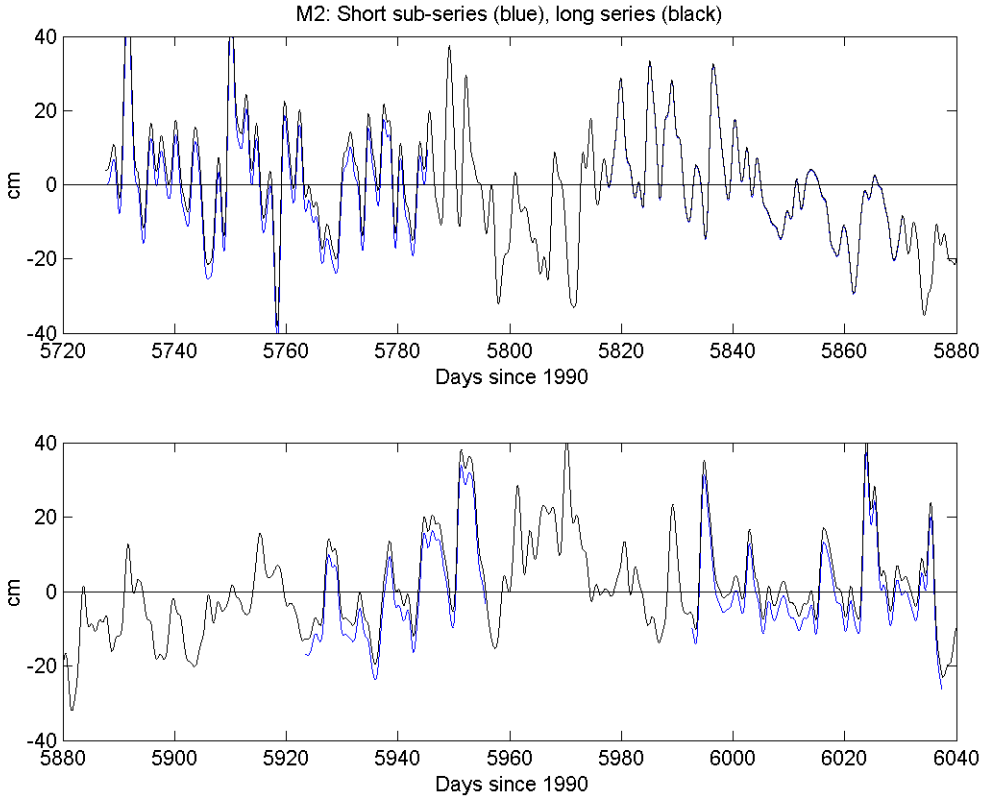

Figure 11.2. The long (black) and short (blue) sea level series for M2. Each long and short time series has zero mean. The long and short series are indistinguishable between days 5820 and 5880.

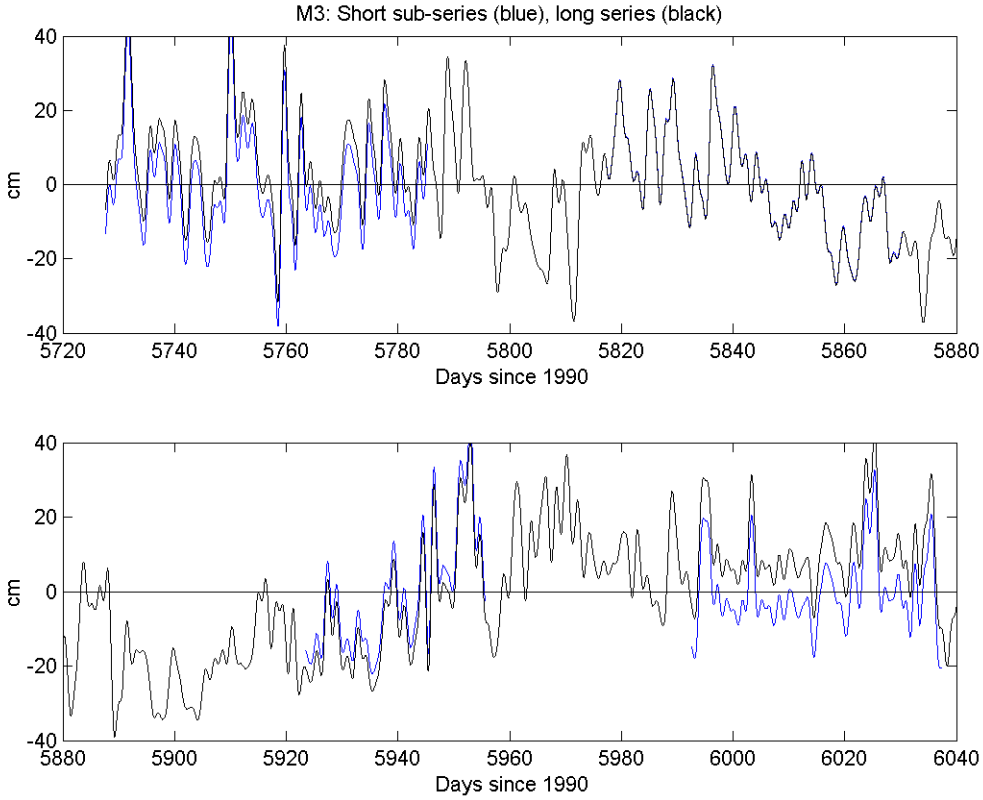

Figure 11.3. The long (black) and short (blue) sea level series for M3. Each long and short time series has zero mean. The long and short series are indistinguishable between days 5820 and 5880.

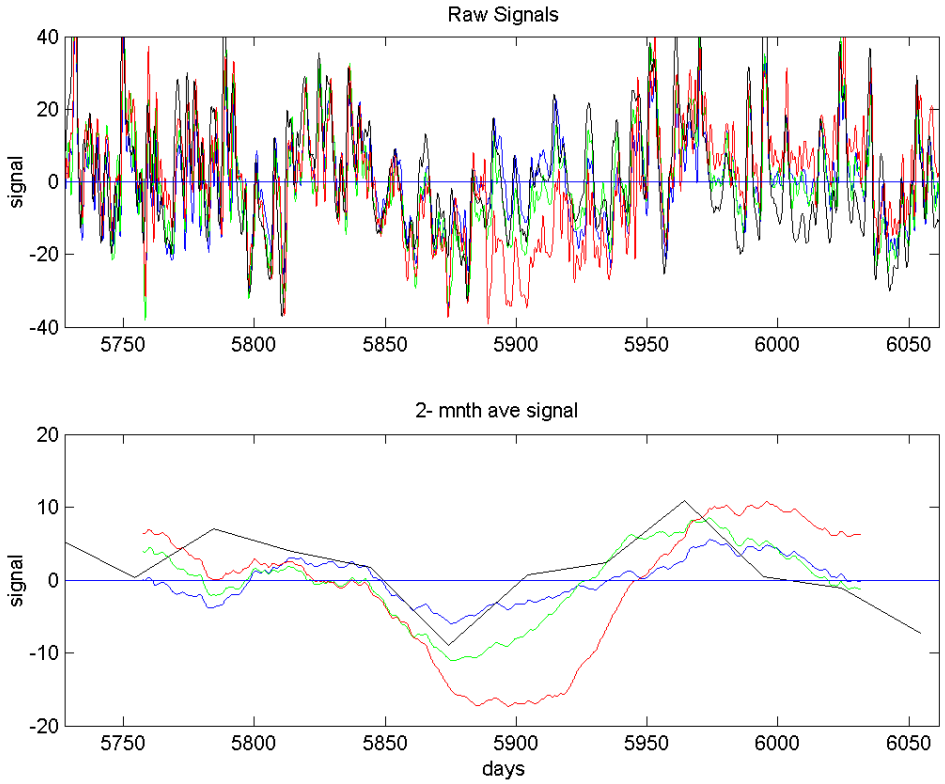

Figure 11.4. Upper: the (29hr-cut-off) Thompson filtered long sea level series. Lower: the 3-month average of the sea level data in the upper panel. The series are for M1 (blue), M2 (green), M3 (red) and Thevenard (black).

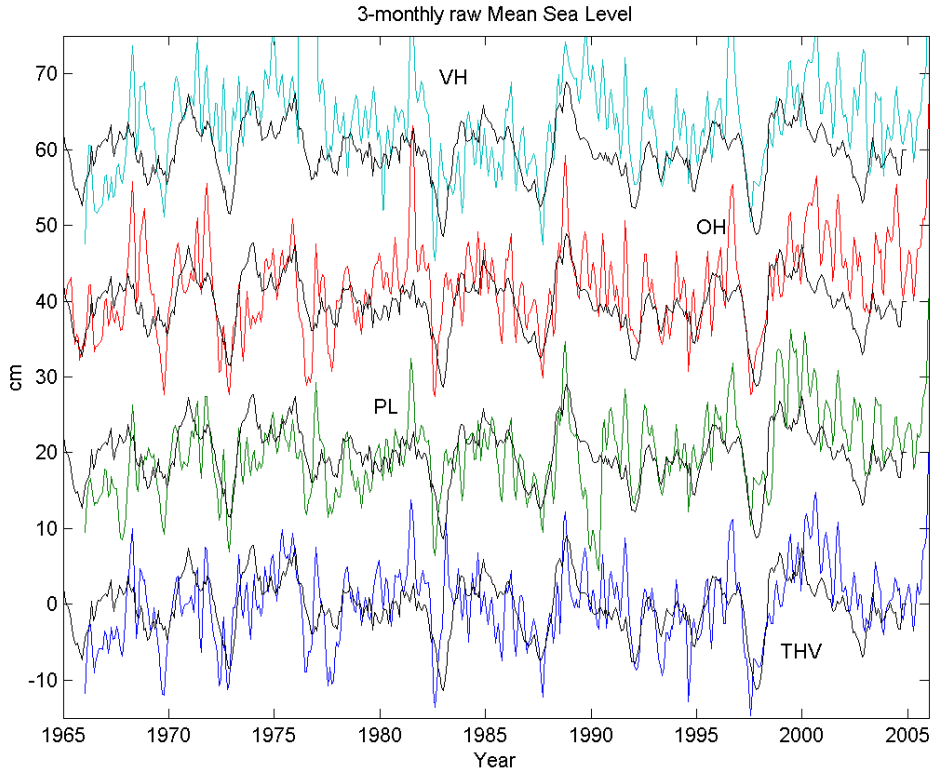

Figure 11.5. The 3-monthly averaged sea level from Thevenard (THV), Port Lincoln (PL), Outer Harbour (OH) and Victor Harbour (VH) offset by 20 m. The black curve is the –nino3.4 index which if negative indicates El Nino conditions.

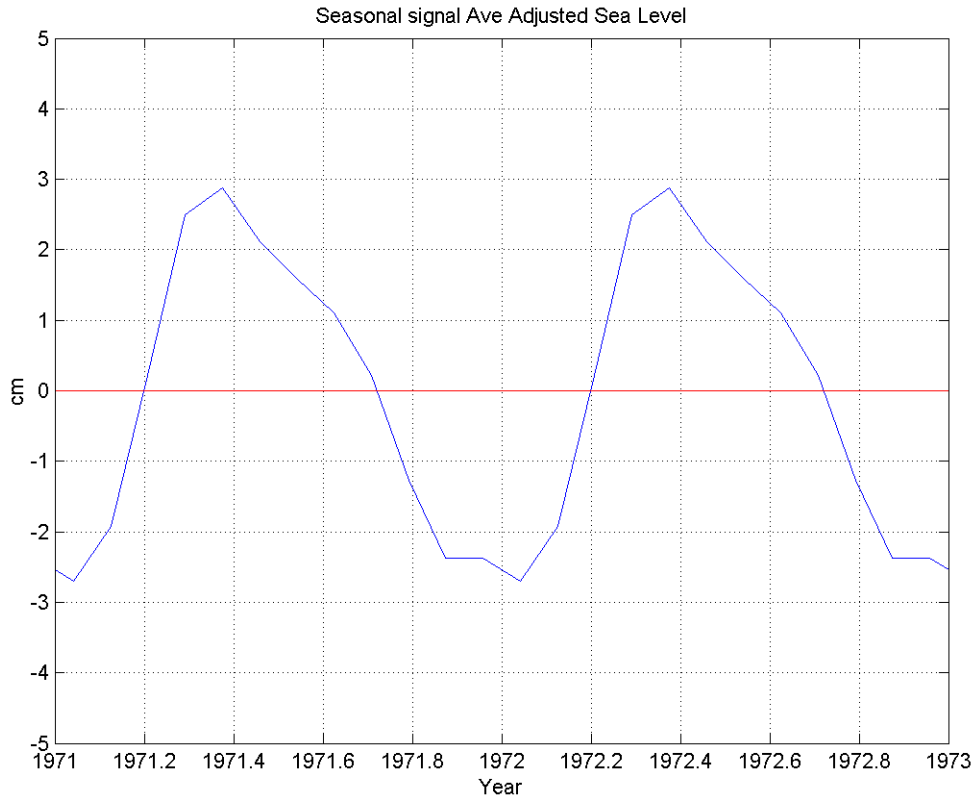

Figure 11.6 The monthly average of Thevenard and Outer Harbour sea level data for the 1971-1973 period. Note: the averages at the two sites were nearly identical, (from Middleton et al 2007).

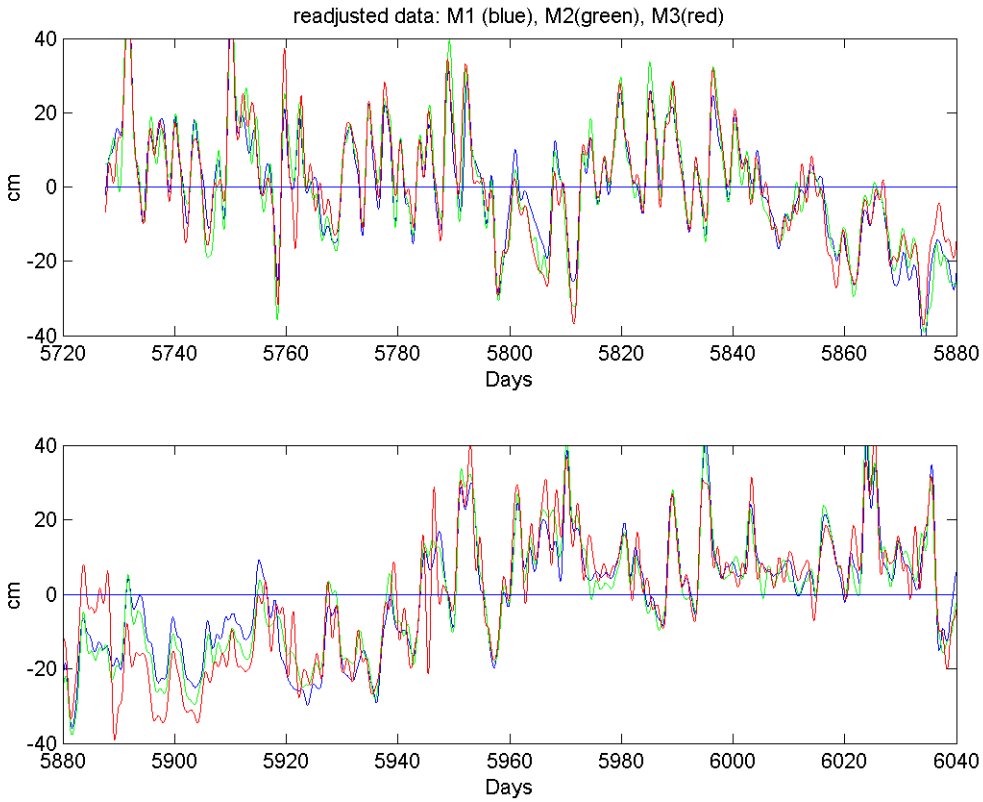

Figure 11.7. The long time series of sea-level data readjusted to all have the M3 seasonal (2-monthly) average shown in Figure 11.4.

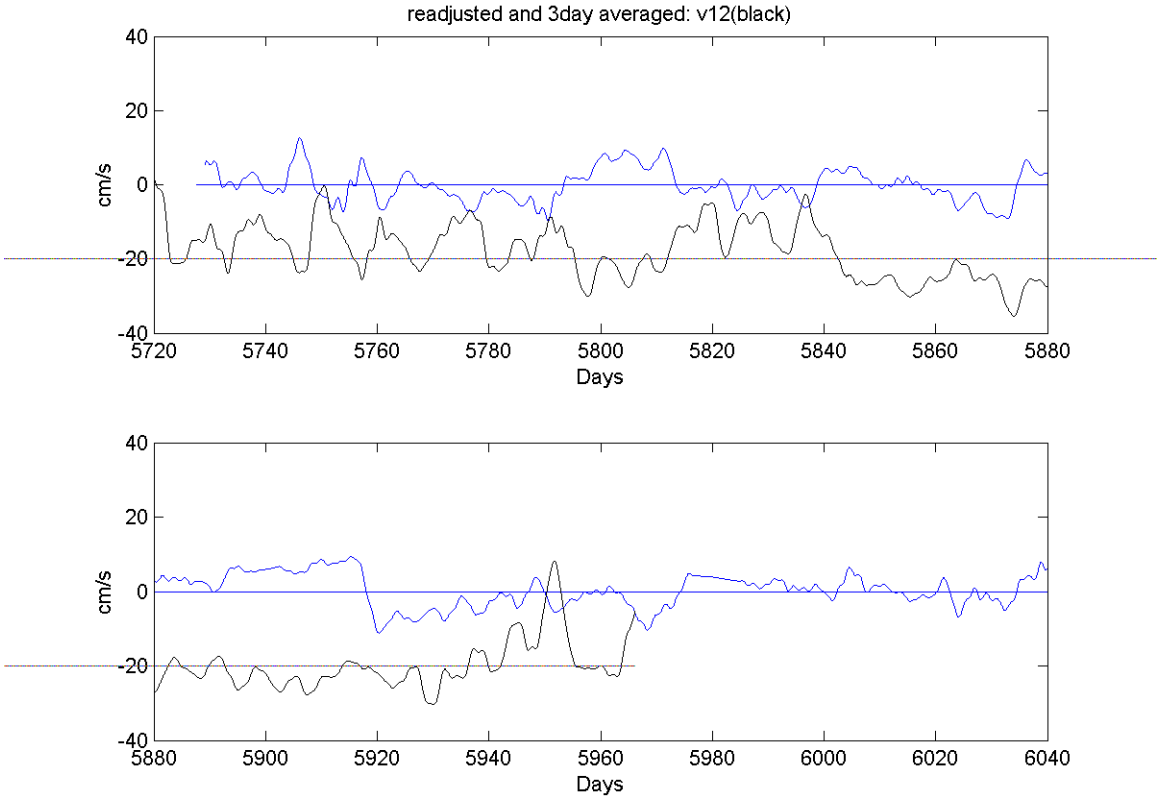

Figure 11.8 The geostrophic velocity v12 (blue) based on the M1 and M2 adjusted time series shown in Figure 11.7. Positive values are directed into the gulf. The black curve denotes the Ekman velocity driven by the wind stress (Neptune Island data). The Ekman velocities are offset by – 20 cm s^{-1} and values below -20 are out of gulf while values above -20 are directed into the gulf. All data has been filtered using a 3-day running block average to eliminate the 2-day variability.

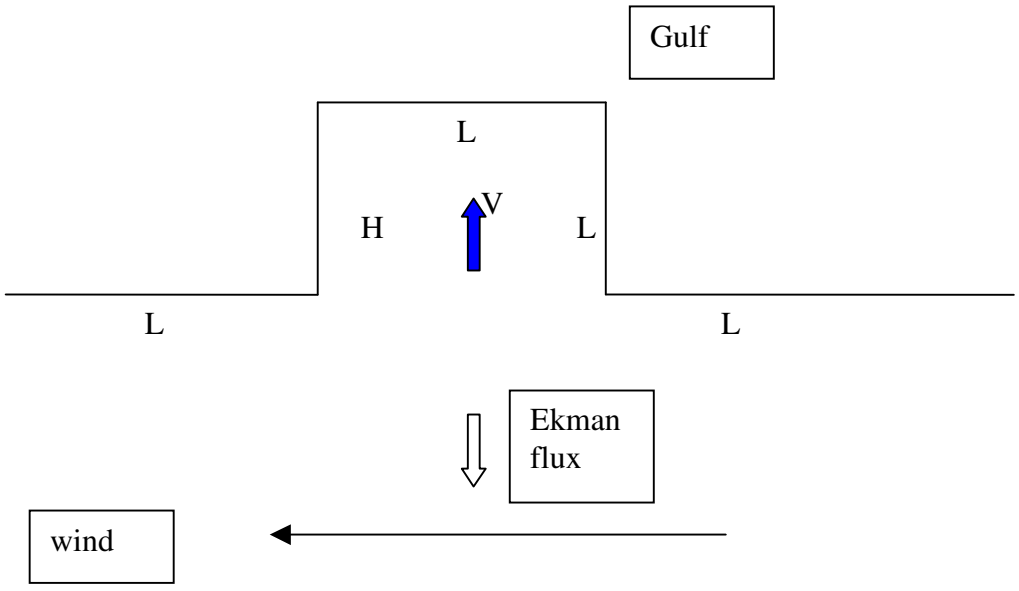

Figure 11.9. Schematic illustrating the northward geostrophic velocity v12 that should arise to offset the mass lost through the surface (out of gulf) Ekman transport for upwelling favourable winds. The geostrophic velocity must be accompanied by a relative high on the west gulf coast.

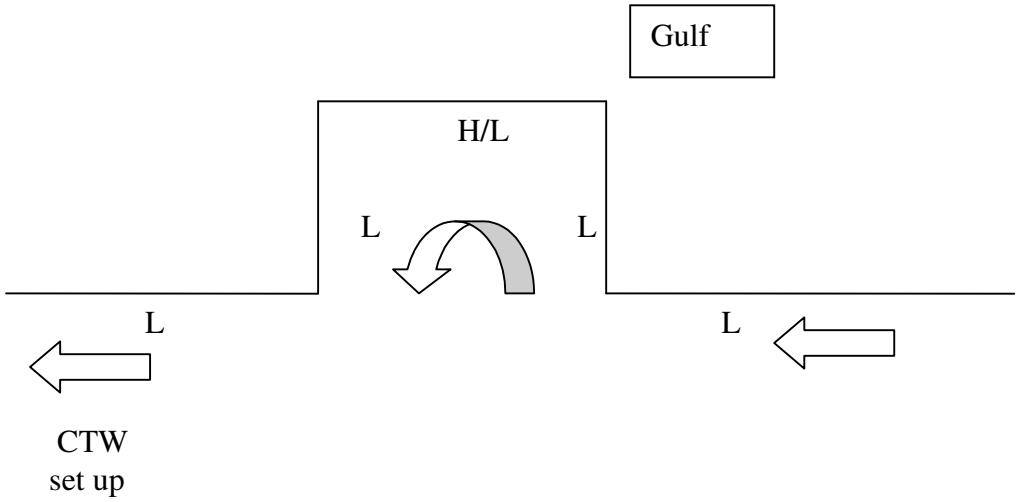

Figure 11.10. Schematic illustrating the shelf and gulf currents when no wind is present and the circulation is driven by coastal trapped waves (CTW) from the west. At the head of gulf, the currents are weak, while at the mouth, the currents lop into the gulf as shown.

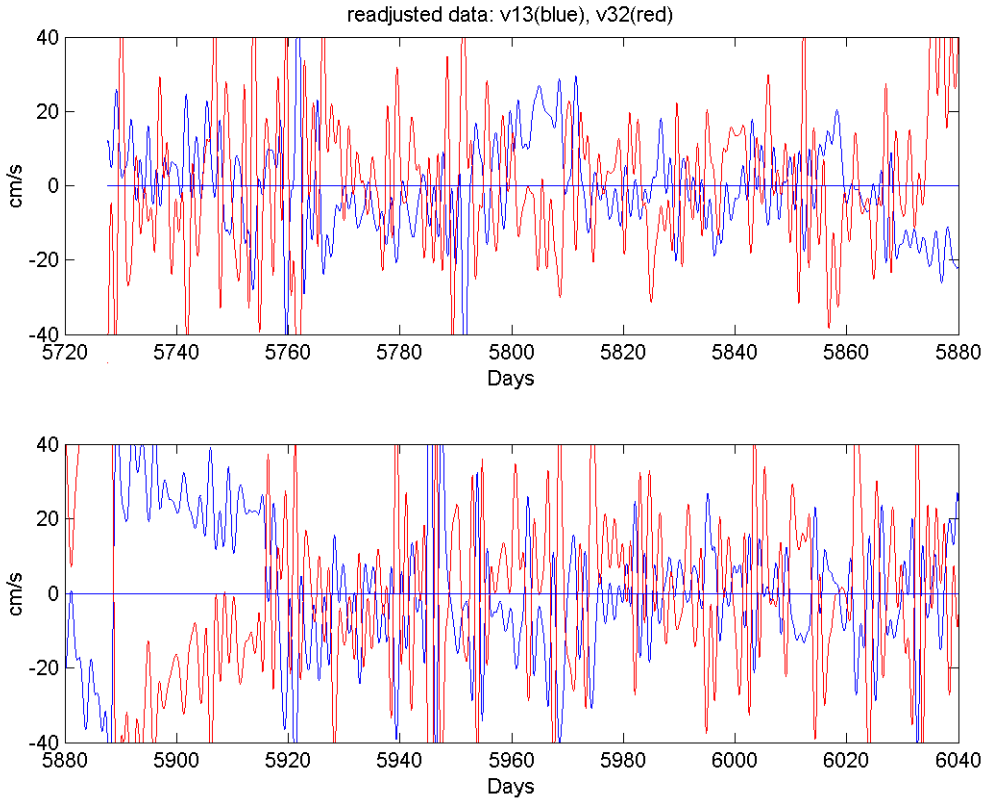

Figure 11.11. The geostrophic velocities v13, and v32 based on the seasonally adjusted long times series for M1, M2, M3. Positive values are to the north (into gulf).

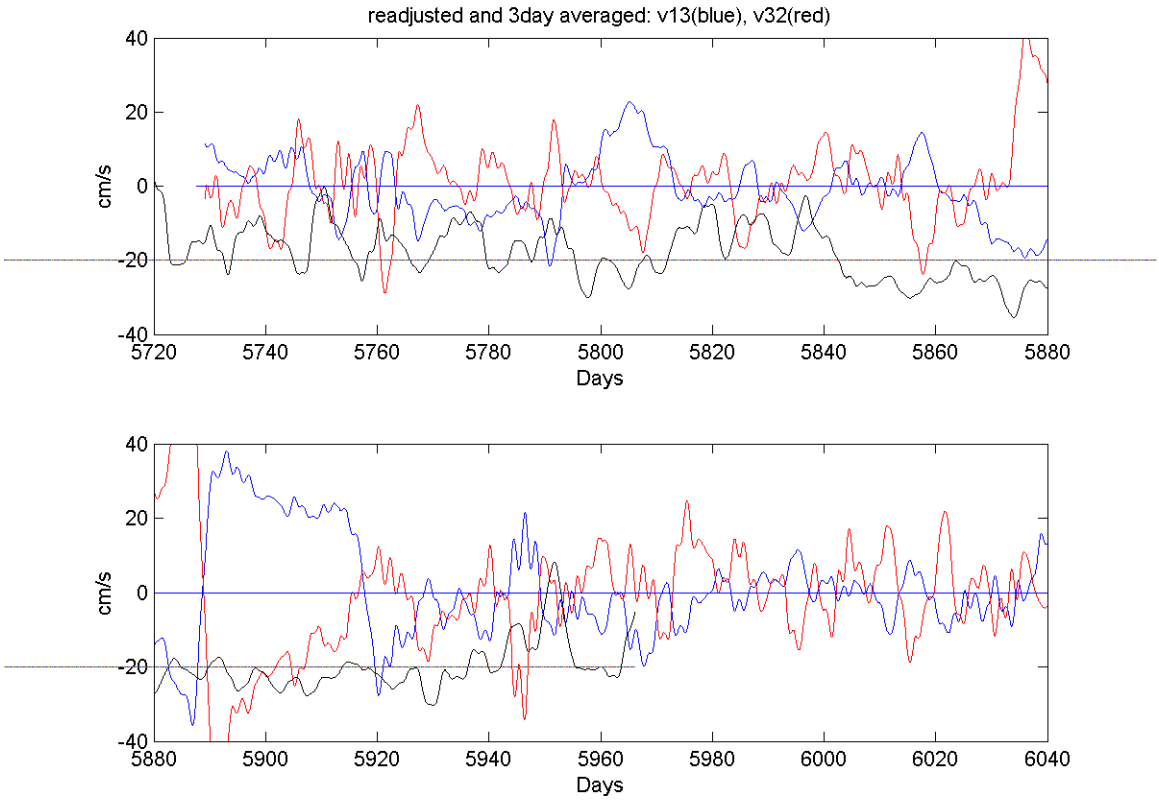

Figure 11.12. The geostrophic velocities v13, and v32 based on the seasonally adjusted long times series for M1, M2, M3. Positive values are to the north (into gulf). A 3-day filter has been applied using a running block average to eliminate the 2-day variability.

12. Appendix B: Local Heating – a simple model

The contribution of local heating was considered using the air-sea heat flux computation in the SHOC. The model domain included all of Spencer Gulf with a detailed nested region in the vicinity of the tuna farming zone. The heat flux data output from the model was used to predict an incremental change in temperature δT over each day and for a mixed layer of depth H according to:

$$\delta T = \frac{tQ_f}{\rho_w C_p H}$$

where t = time increment (s),
Q_f = heat flux from model (Watts m^{-2}),
ρ_w = water density (1024 kg m^{-3}),
C_p = specific heat of water (4000 J kg^{-1} °K^{-1})
and H = depth (20 m).

13. Appendix C: Velocity shear

In general tidal currents are subject to bottom boundary layer shear, and wind-driven currents contain shear primarily in the surface layer. Shear can take the form of differences in both magnitude and direction due to rotational effects. We start by considering magnitude differences. Statistics for low pass filtered data (29 hour cutoff) and the tidal band are presented (as before, the tidal band data is formed by subtracting the low-filtered data from the unfiltered data). Since only M4 was able to resolve both surface and bottom boundary layers, we consider it first.

Surface and Bottom Shear - M4 Statistics

The following quantities are plotted in Figure 13.1: a) $s(t)-\bar{s}(t)$: "shear", where s(t) is the velocity magnitude in either the surface or bottom layer (plotted in red and blue respectively), and $\bar{s}(t)$ is the depth-mean of s(t). b) $\left|s(t)-\bar{s}(t)\right|$: "shear magnitude".

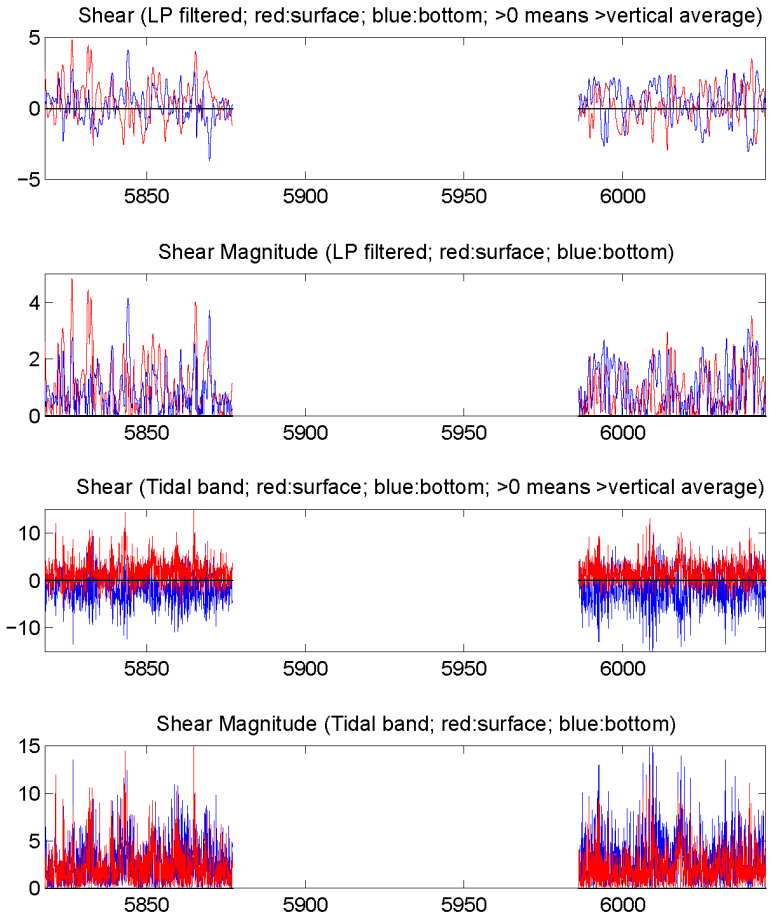

Figure 13.1. Difference between surface (and bottom) speed and that of the water column as a whole at Mooring 4. Low-frequency band (upper two panels) and tidal band (lower two panels). Red: surface minus depth-mean. Blue: bottom minus depth-mean. "Shear magnitude" is the absolute value of the difference.

The mean and rms of the difference time series of Figure 13.1 are given in Table 13.1. Units are cm s^{-1}. A positive/ negative value implies the boundary layer is faster/slower the mean.

Table 13.1. statistics of difference time series at Mooring 4

	Deployment 2 (summer)				**Deployment 4 (winter)**			
	Low Frequency		Tidal Band		Low Frequency		Tidal Band	
	mean	rms	mean	rms	mean	rms	mean	rms
surface	0.6	1.1	1.7	2.4	0.3	0.9	1.6	2.2
bottom	0.2	0.9	-1.6	2.7	0.4	1.1	-1.9	3.1

The surface and bottom velocity differences are both about three times higher in the tidal band than in the low-pass filtered band. In the tidal band the rms difference at the bottom is slightly higher than at the surface. In the low-pass filtered band, the bottom and surface shears are nearly equal.

The directions of the depth-mean current, and the surface and bottom deflections (both in degrees), for M4 are shown in Table 13.2. Positive (negative) deflections are measured counter-clockwise (clockwise) from the direction of the mean flow. The mean flow direction is the angle measured from east.

Table 13.2. Directions of flow at Mooring 4

	Deployment 2 (summer)		**Deployment 4 (winter)**	
	Low Frequency	Tidal Band	Low Frequency	Tidal Band
depth-mean	47.0[1]	84.8 [2]	60.7[1]	80.2 [2]
surface deflection	17.4	3.7	20.4	0.08
bottom deflection	-27.2	-8.5 [3]	-29.8	-6.3 [3]

1: The mean (over time) directions of the components (depth-average, surface, and bottom) are taken first, then the deflection angles (surface versus depth-mean, and bottom versus depth-mean) found.
2: For the tidal band only, the principal axis direction is used to define the mean flow direction.
3. Time mean of hourly deflections.

Shear Statistics for M4 and M5

Selected statistics for the current meters at M4 and M5 are summarized in the tables below, beginning with definitions of the values. The velocity units are cm s^{-1}.

Statistics for unfiltered, low pass filtered (29 hour cutoff), and the tidal band are presented (the tidal band is formed by subtracting the low-filtered data from the unfiltered data).

u,v: east-west and north-south components of velocity;

$\bar{u}, \bar{v}$: depth-integrated values of u,v;

$u_{rms}=\sqrt{<\bar{u}^2>}$ (and similarly for v component): rms value of depth-mean currents (brackets indicate time average);

$$\sigma^{u}{}_{z}(t) = \sqrt{\frac{1}{h}\int_{-h}^{0}(u-\bar{u})^2\,dz}$$

(and similarly for v component): standard deviation of the u component along the z (depth) axis; and

$<\sigma^{u}_{z}(t)>$: time average of $\sigma^{u}_{z}(t)$ (and similarly for v component).

Mooring 4

Deployment 1: 29 August – 14 November 2005

Deployment 2: 16 November 2005 – 10 February 2006

Deployment 3: 11 February – 15 May 2006

Deployment 4: 15 May – 15 August 2006

Table 13.3. $<\overline{u}>,<\overline{v}>$: time averages of depth-mean current components at M4

	Unfiltered				Low Frequency				Tidal Band			
D	1	2	3	4	1	2	3	4	1	2	3	4
u	0.0	0.7	1.1	0.9	-0.1	0.7	1.1	0.9	0.0	0.0	0.0	0.0
v	0.7	0.6	0.7	1.8	0.6	0.6	0.7	1.8	0.0	0.0	0.0	0.0

D: Deployment; u and v in cm/s

Table 13.4. As in Table 13.3, taken over all deployments

	Unfiltered	Low Frequency	Tidal Band
u	0.7	0.7	0.0
v	0.9	0.9	0.0

Table13.5. $<\sigma^{u}_{z}(t)>,<\sigma^{v}_{z}(t)>$: time averages of std. deviations along z-axis at M4

	Unfiltered				Low Frequency				Tidal Band			
D	1	2	3	4	1	2	3	4	1	2	3	4
u	5.0	21.7	7.1	10.6	1.7	2.6	3.4	3.9	4.2	4.9	5.9	3.8
v	11.3	37.6	11.1	23.7	1.6	1.3	1.4	1.8	14.6	13.8	16.3	10.9

D: Deployment; u and v in cm/s

Table 13.6. As in Table 13.5, taken over all deployments

	Unfiltered	Low Frequency	Tidal Band
u	11.1	2.9	4.7
v	20.9	1.5	13.9

Table 13.7. $\sqrt{<\overline{u}^2>}, \sqrt{<\overline{v}^2>}$: rms of depth-mean velocity components at M4

	Unfiltered				Low Frequency				Tidal Band			
D	1	2	3	4	1	2	3	4	1	2	3	4
u	3.3	3.1	3.7	3.4	1.4	1.8	2.0	1.7	2.9	2.5	3.1	3.0
v	10.8	10.0	10.9	12.7	1.7	1.5	1.4	2.6	10.7	9.9	10.8	12.4

D: Deployment; u and v in cm/s

Table 13.8. As in Table 13.7, taken over all deployments

	Unfiltered	Low Frequency	Tidal Band
u	3.4	1.7	2.8
v	11.1	1.8	11.0

Mooring 5

Deployment 1: 30 August – 14 November 2005

Deployment 2: 16 November 2005 – 10 February 2006

Deployment 3: 11 February – 15 May 2006

Deployment 4: 16 May – 15 August 2006

Table 13.9. $<\overline{u}>, <\overline{v}>$: time averages of depth-mean current components at M5

	Unfiltered				Low Frequency				Tidal Band			
D	1	2	3	4	1	2	3	4	1	2	3	4
u	-2.4	2.9	-	-1.6	-2.4	2.9	-	0.9	0.0	0.0	-	0.0
v	0.4	-4.0	-	0.8	0.4	-4.0	-	1.8	0.0	0.0	-	0.0

D: Deployment; u and v in cm/s

Table13. 10. As in Table 13.9, taken over all deployments

	Unfiltered	Low Frequency	Tidal Band
u	-0.4	-0.4	0.0
v	-0.9	-0.9	0.0

Table 13.11. $<\sigma_z^u(t)>, <\sigma_z^v(t)>$: time averages of std. deviations along z-axis at M5

	Unfiltered				Low Frequency				Tidal Band			
D	1	2	3	4	1	2	3	4	1	2	3	4
u	2.2	3.8	-	5.5	1.3	1.8	-	1.9	3.3	3.7	-	3.4
v	3.9	3.9	-	5.2	2.0	1.2	-	3.9	5.9	2.3	-	3.0

D: Deployment; u and v in cm/s

Table 13.12. As in Table 13.11, taken over all deployments

	Unfiltered	Low Frequency	Tidal Band
u	3.9	1.7	3.4
v	4.3	2.3	3.7

Table 13.13. $\sqrt{<\bar{u}^2>}$, $\sqrt{<\bar{v}^2>}$: rms of depth-mean velocity components at M5

	Unfiltered				Low Pass Filtered				Tidal Band			
D	1	2	3	4	1	2	3	4	1	2	3	4
u	3.7	5.4	-	4.6	2.7	3.3	-	2.1	2.4	4.2	-	4.0
v	5.9	5.4	-	3.5	1.6	4.4	-	1.6	5.5	3.2	-	3.0

D: Deployment; u and v in cm/s

Table 13.14. As in Table 13.13, taken over all deployments at M5

	Raw	Low Frequency (subtidal)	Tidal Band
u	4.5	2.7	3.5
v	4.9	2.5	3.9